Summer 8-12-2011

Microfluidic Pumping With Surface Tension Force and Magnetohydrodynamic Drive

Mian Qin
qq1985ear@gmail.com

Microfluidic Pumping With Surface Tension Force and Magnetohydrodynamic Drive

Abstract
Micropumping is difficult to design and control as compared to their macro-scale counterparts due to the size limitation.

The first part of this dissertation focuses on micropumping with surface tension forces. A simple, single-action, capillary pump/valve consisting of a bi-phase slug confined in a non-uniform conduit is described. At low temperatures, the slug is solid and seals the conduit. Once heated above its melting temperature, the liquid slug moves spontaneously along a predetermined path due to surface tension forces imbalance. This technique can be easily combined with other propulsion mechanisms such as pressure and magnetohydrodynamics (MHD).

The second part of this dissertation focuses on MHD micropumping, which provides a convenient, programmable means for propelling liquids and controlling fluid flow without a need for mechanical pumps and valves. Firstly, we examined the response of a model one dimensional electrochemical thin film to time-independent and time-dependent applied polarizations, using the Nernst-Planck (NP) model with electroneutrality and the Poisson-Nernst-Planck (PNP) model without electro -neutrality, respectively. The NP model with well designed boundary conditions was v developed, proved capable of describing the bulk behavior as accurate as the full PNP model. Secondly, we studied the MHD propelled liquid motion in a uniform conduit patterned with cylinders. We proved equivalence in MHD and pressure driven flow patterns under certain conditions. We examined the effect of interior obstacles on the electric current flow in the conduit and showed the existence of particular pillar geometry that maximizes the current. Thirdly, we looked at MHD flow of a binary electrolyte between concentric cylinders. The base flow was similar to the pressure driven flow in the same setup. The first order perturbation fields, however, behave differently as the traditional Dean's flow. We carried out one-dimensional linear stability analysis for the unbounded small gap situation and solved it as an eigenvalue problem. Two-dimensional nonlinear simulation was performed for finite gap size or bounded situations. We observed strong directionality of the applied electric field for the onset of stability. Results in this study could help enhance the stability of the system or introduce secondary motion depending on the nature of the applications.

Degree Type
Dissertation

Degree Name
Doctor of Philosophy (PhD)

Graduate Group
Mechanical Engineering & Applied Mechanics

First Advisor
Haim H. Bau

Keywords
magnetohydrodynamic flow, MHD, microfluidic, electrochemical system, surface tension, electrokinetic flow

Subject Categories
Other Mechanical Engineering | Transport Phenomena

MICROFLUIDIC PUMPING WITH SURFACE TENSION FORCE AND MAGNETOHYDRODYNAMIC DRIVE

Mian Qin

A DISSERTATION

in

Mechanical Engineering and Applied Mechanics

Presented to the Faculties of the University of Pennsylvania

in

Partial Fulfillment of the Requirements for the

Degree of Doctor of Philosophy

2011

Supervisor of Dissertation

_____

Haim H. Bau

Professor of Mechanical Engineering and Applied Mechanics

Graduate Group Chairperson

_____

Jennifer R. Lukes

Professor of Mechanical Engineering and Applied Mechanics

Dissertation Committee

Paulo E. Arratia, Assistant Professor of Mechanical Engineering and Applied Mechanics

Haim H. Bau, Professor of Mechanical Engineering and Applied Mechanics

Howard H. Hu, Professor of Mechanical Engineering and Applied Mechanics

Acknowledgement

I am heartily thankful to my advisor Haim H. Bau, whose encouragement, supervision and support from the preliminary to the concluding stages enabled me to develop an understanding of the research subjects, and more importantly, the attitude towards science, career and beyond. There truly have been ups and downs during my five years of graduate study. No matter what the situations were, Dr. Bau was always there to guide and help. I feel so lucky to be here as his student and believe that the great experience will deeply influence my future in a very positive way.

I am also grateful to my committee members: Dr. Howard H. Hu and Dr. Paulo E. Arratia, for discussing with me, giving me valuable advice and reviewing my dissertation.

My thanks also go to the current and former members in Dr. Bau and Dr. Hu's group: Jason Thompson, Joe Grogan, Tong Gao, Xiaohong Yan, Sean Anderson, Mike Norton, Dr. Michael Mauk, Dr. Robert Hart, Dr. Dafeng Chen, Dr. Changchun Liu, Dr. Zongyuan Chen, Dr. Jing Wang, Dr. Hui Zhao, Dr. Shizhi Qian, Dr. Michael Schrlau, Dr. Mark Arsenault and Dr. T. N. Swamynathan. In particular, I thank Dr. Xianbo Qiu and Jason Kwa, who helped me with the microfluidic device fabrication.

I am indebted to the other faculty, staff and colleagues in the department of Mechanical Engineering and Applied Mechanics at the University of Pennsylvania. Ms. Maryeileen B. Griffith, Ms. Sue Waddington-Pilder and Ms. Olivia Brubaker offered generous help whenever I need it. I also thank Haizhen Pan, Nora Ayanian,

Jack Franklin, Neil Zuckerman and other MEGA officers for their support and friendship. My special thanks go to Mrs. Hu, who provided us with many pleasant moments.

Last but not least, I would like to thank my parents for their unconditional love, endless support and sacrifice. I also want to thank my husband Liang Fu for his love and companionship. And my dearest son Kuan, he encourages me in a unique nonverbal way all the time.

ABSTRACT

MICROFLUIDIC PUMPING WITH SURFACE TENSION FORCE AND MAGNETOHYDRODYNAMIC DRIVE

Mian Qin

Advisor: Dr. Haim H. Bau

Micropumping is difficult to design and control as compared to their macro-scale counterparts due to the size limitation.

The first part of this dissertation focuses on micropumping with surface tension forces. A simple, single-action, capillary pump/valve consisting of a bi-phase slug confined in a non-uniform conduit is described. At low temperatures, the slug is solid and seals the conduit. Once heated above its melting temperature, the liquid slug moves spontaneously along a predetermined path due to surface tension forces imbalance. This technique can be easily combined with other propulsion mechanisms such as pressure and magnetohydrodynamics (MHD).

The second part of this dissertation focuses on MHD micropumping, which provides a convenient, programmable means for propelling liquids and controlling fluid flow without a need for mechanical pumps and valves. Firstly, we examined the response of a model one dimensional electrochemical thin film to time-independent and time-dependent applied polarizations, using the Nernst-Planck (NP) model with electroneutrality and the Poisson-Nernst-Planck (PNP) model without electro -neutrality, respectively. The NP model with well designed boundary conditions was

developed, proved capable of describing the bulk behavior as accurate as the full PNP model. Secondly, we studied the MHD propelled liquid motion in a uniform conduit patterned with cylinders. We proved equivalence in MHD and pressure driven flow patterns under certain conditions. We examined the effect of interior obstacles on the electric current flow in the conduit and showed the existence of particular pillar geometry that maximizes the current. Thirdly, we looked at MHD flow of a binary electrolyte between concentric cylinders. The base flow was similar to the pressure driven flow in the same setup. The first order perturbation fields, however, behave differently as the traditional Dean's flow. We carried out one-dimensional linear stability analysis for the unbounded small gap situation and solved it as an eigenvalue problem. Two-dimensional nonlinear simulation was performed for finite gap size or bounded situations. We observed strong directionality of the applied electric field for the onset of stability. Results in this study could help enhance the stability of the system or introduce secondary motion depending on the nature of the applications.

TABLE OF CONTENTS

LIST OF TABLES

LIST OF FIGURES

CHAPTER 1: Introduction

1.1 Lab-on-a-chip

There're a few terms that have become popular in the engineering world in recent years: micro total analysis system (μTAS), lab-on-a-chip (LOC), micro-fluidics, micro-electro-mechanical- system (MEMS) and their nano-counterparts (NEMS). These terms refer to devices that significantly downscale the conventional laboratory tools and integrate the current experimental devices' functions. In the sequence they're put, each term has broader meaning than the previous one: e.g., LOC is a device that integrates on a single substrate one or several laboratory functions and deals with the handling of extremely small volume of fluids; while micro-fluidics include mechanical flow control elements aside from stated above. A typical microfluidic device usually consists of the following: fluid channels, micromixers, microvalves, micropumps and calibrating devices. Various purposes covering mechanical, chemical and biological fields could be realized on these small devices, e.g., flow separation, liquid chromatograph, HIV detection and DNA amplification, see Ziober et al. 2008 for an example.

The advantages of microfluidic technology over the traditional bench-top methods include: 1) small fluid volume, which means reduced consumption of reagents and production of waste, also requires less sample volume for diagnostics, say one tiny drop of blood sample instead of a tube; 2) small reactor size, which means shorter diffusion distances and shorter response times to heating/cooling, leading to faster diagnosis; 3) high surface to volume ratios, which means ample

reaction surfaces and active binding sites, also fast heat dissipation; 4) integrated functionality and enhanced compactness of the systems; 5) massive parallelization due to compactness, which allows high-throughput analysis; 6) low cost, since it usually involves cheap plastics and massive fabrication, making disposable chips possible; 7) safer platform for chemical, radioactive or biological studies because of integration of functionality and less human interference during the process; 8) easy storage, better portability, less energy consumption and etc.. For the overview of problems associated with microfluidics, such as Joule heating, channel geometry and flow resistance, see Bayraktar & Pidugu, 2006 and Sharp et al. 2005.

Any microfluidic device, regardless of its functions, substrate material, fabrication technique and structural design, requires precise handling of small liquid volumes, usually in the pico liter range. The small fluid volumes in these systems needs to be stored, pumped, mixed, dispensed or otherwise manipulated to achieve desired mechanical, biological or chemical effects. For example, PCR (polymerase chain reaction) reagents may need to be first introduced from separate fluid reservoirs into a mixing chamber and then be transported among different temperature regions on the microchip so that the DNA templates could cyclically undergo denaturation, annealing and elongation processes and finally achieve massive duplication (**Fig. 1**) . For the fluid transport purposes mentioned above, passive and active control of fluid motion is desired, which are generally referred to as micropumping and microvalving techniques. For a review on microvalving, see Oh & Ahn, 2006. We focus on micropumping in the following text.

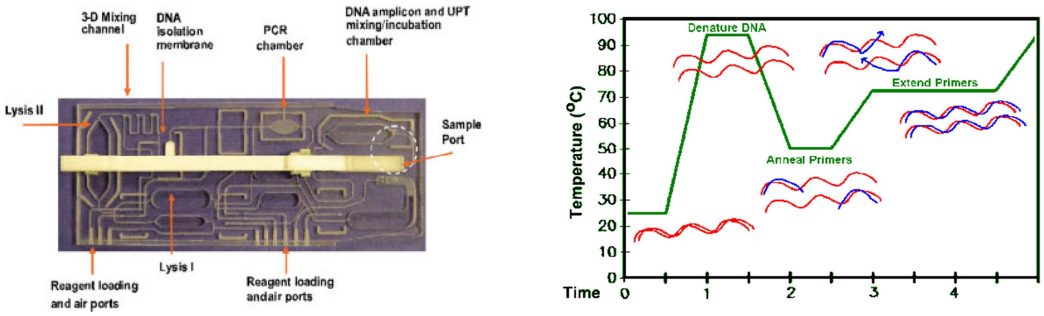

Fig. 1 a) A polycarbonate based microfluidic device for oral cancer screening and detection (Ziober et al. 2008); b) the principle of PCR reactions (by Dr. Steven M. Carr).

1.2 Micropumping Techniques

There're two categories of micropumping techniques according to Laser and Santiago, 2004: 1) displacement micropumping, including reciprocating, rotary and aperiodic pumping; 2) dynamic micropumping, utilizing centrifugal, electroosmotic, electrohydrodynamic, magnetohydrodynamic forces and etc. The various dynamic micropumping methods are referred to as "Continuous flow micropumping" in Woias, 2005.

Micropumping could be very challenging in a few aspects. First, small pump size is desirable due to the limited space on the microchip. Rigorously miniaturize part by part a normal sized pump will be extremely difficult and expensive, if not impossible. Second, although high pumping rate are usually not required in microfluidics, precise metering of fluid volume are of great importance. Even if the absolute difference is minute, the relative error will be significant. The result is especially noticeable for highly sensitive biological and medical diagnosis and

treatments. Third, due to the decreased channel size accompanied by the increased flow resistance, pressure gradient required by the micropump is not insignificant. Surface forces (e.g., surface tension, if multiphase flow and interfaces are present) are becoming more important due to the increased surface area to volume ratio and could act adversely to the pumping. Reliability, power consumption, cost and biocompatibility are critical issues to micropumping, too.

1.3 Surface Tension

Surface tension force driven fluid has many distinct advantages. As a passive pumping method, it requires no consumption of energy. Also, as a surface force, it scales with the size of the conduit to the second order and is comparatively more important in micro-scales compared to the other body forces (inertia, gravity and etc.). Examples of how surface tension forces could be utilized to propel fluid motion are summarized in Bico & Quere, 2002. The balance of surface tension could be broken by capillary imbibition, conical shaped conduit, surface hydrophilicity gradient, reactive surface, photosensitive surface and temperature ununiformity. For more background of surface tension based micropumping, refer to chapter 2.1.

1.4 Magnetohydrodynamic Flow

Among the dynamic pumping methods, magneto-hydrodynamic (MHD) pumping draws much attention. The biological samples are usually electrically conductive and could carry electric current flow. Under an applied magnetic field, the

electric and magnetic field interaction results in Lorentz force, which in turn, drives fluid motion (Qian & Bau, 2009). The operation of a MHD pump requires no moving element. The generated flow rate is easily adjustable by tuning the amount of applied current/voltage. For more background of MHD based micropumping, refer to chapter 3.1, 4.1 and 5.1.

1.5 Organization of the Dissertation

We discussed surface tension force and MHD based fluid pumping in more details in the following chapters. Chapter 2 studies experimentally and theoretically the surface tension based micro –pumping using phase change materials. Chapter 3 studies theoretically and numerically the electrochemical response of weakly conducting electrolyte under AC and DC applied polarizations. Chapter 4 studies the MHD micropumping in weakly conducting electrolyte, which is confined in a uniform conduit and surrounding circular cylinders. Chapter 5 studies the MHD flow behavior in curved channels, including base flow pattern and stability analysis. Chapter 6 Concludes.

CHAPTER 2: Surface Tension Based Phase Change Pump / Valve

2.1 Introduction

In microfluidic applications, it is often necessary to induce and control fluid motion in minute conduits. Since frequently the devices are designed to be disposable, it is desirable to achieve these objectives inexpensively and reliably. Given the relatively large ratio of surface area to volume in microfluidic devices, it is natural to attempt to utilize surface forces for flow control.

One of the early examples of the use of surface forces to move liquids is imbibition by capillaries and porous materials. Washburn's 1921 derived a theory of the dynamics of imbibition in circular capillaries in contact, on one side, with a large body of liquid and confirmed his theoretical predictions with experimental observations. Imbalance of surface tension forces that induces fluid motion may result from various factors such as (*i*) the presence of single meniscus as in Washburn's work; (*ii*) non-uniform geometry such as a cone-shaped conduit (Zhang et al. 2007); (*iii*) variations in surface tension resulting from variations in chemical composition (Weislogel 1997) and/or temperature (Mazouchi 1999); and (*iv*) variations in contact angle due to varying surface properties induced by chemical reactions (De Gennes 1998, Sumino et al. 2005), light (Ichimura et al. 2000), and electric fields (Yun et al. 2002). The surface-induced forces can propel immiscible liquid slugs that, in turn, can displace the working fluid, provide diffusion barriers between solutions of various compositions, and open and close connections.

To be useful, the surface tension-driven flow must occur at will under

operator's control. To avoid spontaneous, undesired motion, we propose the use of phase change material. During storage and inactivity, the slug is maintained in solid state, frozen in position. When fluid motion, pumping, and valving are desired, the slug is heated to above its melting temperature. Once in liquid state, the slug motion occurs spontaneously by the action of surface forces. The motion can be further enhanced with other pressure sources. When the source of heat is removed, the slug returns to its frozen, immobile state.

There are many examples in the literature of phase change valves (Bico & Quere 2002, Oh & Ahn 2006). In some instances, the working fluid itself has been frozen (ice valve) to close a flow passage (Hobbs & Pisano 2003). In other cases, researchers used low-temperature melting paraffin. Occasionally, designers took advantage of the volume change associated with the paraffin's phase change to actuate a flexible membrane (Yoo et al. 2007, Chen et al. 2005, Boden et al. 2006, Klintberg et al. 2003, Lee & Lucyszyn 2005, Yang & Lin 2006, Carlen & Mastrangelo 2002, Selvaga -napathy et al. 2003, Klintberg et al. 2003). In other instances, the molten material was displaced and moved out of the way with external pressure force (Song et al. 2008) or with magnetic force when the paraffin plug was laden with magnetic particles (Liu et al. 2004). When in solid state, the paraffin valves were reported to withstand pressures of at least 50psi without leakage (Liu et al. 2004).

In the current work, we combine phase-change material with surface tension forces to facilitate pumping and valving. In the following part of this chapter, I first provide a theory for the surface tension-driven motion of the fluid. Second, I

demonstrate that this pumping performance can be optimized. Third, I describe a few examples of implementations and compares experimental observations with theoretical predictions. Then I present the discussions and conclusions.

2.2 Theory

In this section, we study the plug motion once it is in a liquid state. Consider the closed loop depicted in Fig. 2.1 consisting of two cylindrical conduits with diameters d_1 and d_2 ($d_2 > d_1$). The two menisci between the immiscible liquid pair are initially located in conduits of different diameters. Normally, material 2 is in solid state. Here, we follow the chain of events once liquid 2 has been heated above its melting temperature and is in its liquid state.

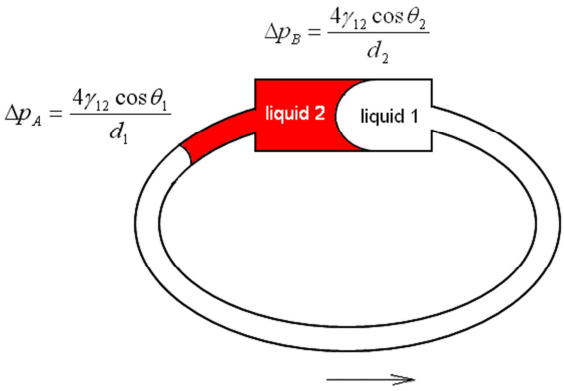

Figure 2.1 A closed loop consisting of two cylindrical conduits of diameters d_1 and d_2 containing two immiscible liquids 1 and 2. One meniscus is located in the small tube and the other in the large tube.

According to the Young equation, the pressure jumps across the interfaces between liquid 1 and liquid 2 are, respectively, $\Delta p_A = 4\gamma_{12}\cos\theta_1 / d_1$ in the small conduit and $\Delta p_B = 4\gamma_{12}\cos\theta_2 / d_2$ in the large conduit. In the above, γ_{12} is the interfacial surface tension; and θ_1 and θ_2 are, respectively, the contact angles

between liquid 1 and liquid 2 in the small and large conduits. Since $d_1 < d_2$, $\Delta p_A > \Delta p_B$ and the liquids will move in the counterclockwise direction. The driving force is

$$F = \pi\gamma_{12}(d_1\cos\theta_1 - d_2\cos\theta_2). \qquad 2.1$$

The above expression can also be derived based on energy considerations.

When the slug is in motion, the contact angle will change as a result of the combined effects of the viscous force, which pins the meniscus at the conduit's wall, and the surface tension, which preserves the spherical shape of the meniscus. This dynamic effect decreases the curvature of the advancing interface and increases that of the receding interface (Fig. 2.2). We use a simple model to describe this contact angle hysteresis (Bico & Quere 2002).

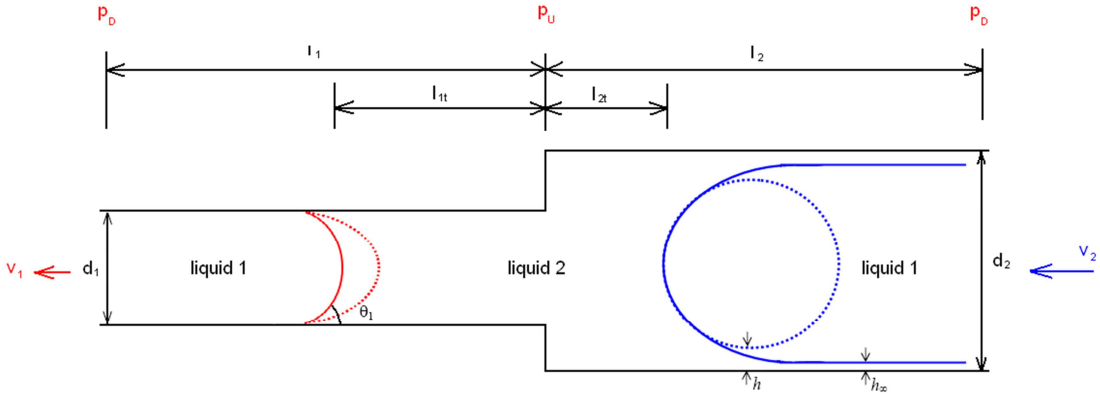

Figure 2.2 The shapes of the advancing and receding menisci when the slug moves towards the left.

The contact angle of the advancing interface (Hoffman 1975):

$$\theta_1 = \left[6\Gamma\cdot(Ca+\delta)\right]^{1/3} \qquad 2.2$$

is a function of the capillary number

$$Ca = \mu u/\gamma_{12}, \qquad 2.3$$

which represents the ratio of the viscous and the interfacial force. In the above, u is the average velocity of the fluid in the conduit, $\Gamma = \ln(d_1/2a)$, and a is a molecular length scale on the order of a few angstroms. For example, when $d_1 = 4mm$ and $a = 6\,\mathring{A}$ (Bico & Quere 2002, Hoffman 1975), $\Gamma \sim 15$. To recover the equilibrium contact angle at zero velocity, one sets $\delta = \frac{\theta_e^3}{6\Gamma}$, where θ_e is the equilibrium contact angle.

When liquid 2 is wetting, downstream of the receding interface, a film is deposited along the conduit's wall with thickness (Bretherton 1961)

$$h_\infty = 1.34R \cdot Ca^{2/3}. \qquad 2.4$$

As a result, the radius of curvature of the receding meniscus is smaller than the actual radius of the conduit (Fig. 2.2b) by (Bico & Quere 2002)

$$h = 2.9h_\infty. \qquad 2.5$$

Moreover, since the liquid wets itself, $\theta_2 = 0$. The above model indicates that the motion dynamics is independent of the large conduit's material. This is consistent with our experimental observations (see section 2.4).

In our analysis, we assume that the apparatus (Fig. 2.1) is horizontal and neglect gravitational forces. This is justified when the ratio of the gravitational force and the surface tension force as given by the Bond number $Bo = \frac{|\Delta\rho| g d_1^2}{4\gamma_{12}}$ is small. In the above, $\Delta\rho = \rho_1 - \rho_2$ is the difference between the densities of fluids 1 and 2 and g is the gravitational acceleration. For example, when the two substances are oil and air ($\Delta\rho = 800kg/m^3$), the tube diameter is $1mm$, and the interfacial tension is

$0.01N/m$, the Bond number is ~ 0.2.

The momentum equation in the smaller capillary

$$\frac{d(m_1u_1)}{dt} = (p_D - p_U)\frac{\pi d_1^2}{4} + \pi d_1\gamma_{12}cos\theta_1 - 8\pi[\mu_1(l_1 - l_{1t}) + \mu_2 l_{1t}]u_1. \qquad 2.6$$

where the various lengths are defined in Fig. 2.2. p_U and p_D are, respectively, the pressures upstream and downstream (assuming flow in the counterclockwise direction) of the small conduit. m_i, l_i and $u_i\,(i=1,2)$ are, respectively, the total mass, the total length, and the velocity of the fluids in conduit i. μ_1 and μ_2 are, respectively, the viscosities of liquid 1 and liquid 2. l_{it} is the length occupied by fluid 1 in conduit i at time t. In the above, we assume that the flow along most of the length of the conduit obeys Poiseuille law (parabolic velocity profile) and both liquids are incompressible. Similarly, in the large diameter conduit

$$\frac{d(m_2u_2)}{dt} = (p_U - p_D)\frac{\pi d_2^2}{4} - \pi(d_2 - 2h)\gamma_{12} - 8\pi\left[\mu_1(l_2 - l_{2t}) + \mu_2 l_{2t}\right]u_2. \qquad 2.7$$

The total liquid mass in conduit i is:

$$m_i = \left[\rho_1(l_i - l_{it}) + \rho_2 l_{it}\right]\frac{\pi d_i^2}{4}. \qquad 2.8$$

The velocity of the fluids in the small diameter conduit is:

$$u_1 = \frac{dl_{1t}}{dt}. \qquad 2.9$$

The velocity in the large diameter conduit is:

$$u_2 = -\frac{dl_{2t}}{dt}. \qquad 2.10$$

Conservation of mass requires that

$$d_1^2(l_{1t} - l_{10}) = d_2^2(l_{20} - l_{2t}). \qquad 2.11$$

Combining equations (2.6-2.11) and eliminating the pressure terms, we obtain

the second order, nonlinear differential equation for l_{1t} as a function of time

$$A(n)\frac{d^2 l_{1t}}{dt^2}+B(n)\frac{d}{dt}\left(l_{1t}\frac{dl_{1t}}{dt}\right)+[C(n)l_{1t}+D(n)]\frac{dl_{1t}}{dt}=4\gamma_{12}\frac{d_2^{\,2}}{nd_1^{\,2}}\left(\frac{\cos\theta_1}{d_1}-\frac{d_2-2h}{d_2^{\,2}}\right). \qquad 2.12$$

In the above,

$$A(n)=(\rho_2-\rho_1)\left(\frac{nd_1^{\,2}}{d_2^{\,2}}l_{10}+l_{20}\right)+\rho_1\left(\frac{d_2^{\,2}}{nd_1^{\,2}}l_1+l_2\right),$$

$$B(n)=(\rho_2-\rho_1)\left(\frac{d_2^{\,2}}{nd_1^{\,2}}-\frac{nd_1^{\,2}}{d_2^{\,2}}\right),$$

$$C(n)=\frac{32}{d_2^{\,2}}(\mu_2-\mu_1)\left(\frac{d_2^{\,4}}{nd_1^{\,4}}-\frac{nd_1^{\,2}}{d_2^{\,2}}\right)$$

and
$$D(n)=\frac{32}{d_2^{\,2}}(\mu_2-\mu_1)\left(\frac{nd_1^{\,2}}{d_2^{\,2}}l_{10}+l_{20}\right)+\mu_1\left(\frac{d_2^{\,4}}{nd_1^{\,4}}l_1+l_2\right)$$

are time-independent. We introduced the variable n to accommodate situations when a large conduit empties into n small diameter conduits. Additional details are provided later in this chapter. Here, in the single conduit case, $n=1$. The initial conditions are: $l_{1t}(0)=l_{10}$ and $\frac{dl_{1t}(0)}{dt}=0$.

Since, in general, equation (2.12) cannot be solved exactly. It is desirable to derive approximate, asymptotic solutions for a few special cases. In the limit of short time ($t\to 0$) and the fluids initially at rest, the velocity is small, the surface tension forces are balanced with the inertial forces, $h\sim 0$, $\theta_1=\theta_{1e}$, and equation (2.12) reduces to:

$$[A(1)+B(1)l_{10}]\frac{d^2 l_{1t}}{dt^2}=4\gamma_{12}\frac{d_2^{\,2}}{d_1^{\,2}}\left(\frac{\cos\theta_1}{d_1}-\frac{d_2-2h}{d_2^{\,2}}\right). \qquad 2.13$$

In the short time limit,

$$l_{1t}(t) = \frac{2\gamma_{12}\frac{d_2^{\,2}}{d_1^{\,2}}\left(\frac{\cos\theta_{1e}}{d_1} - \frac{1}{d_2}\right)}{A(1) + B(1)l_{10}}t^2 + l_{10}. \qquad 2.14$$

Only when the diameter ratio $\frac{d_1}{d_2} < \cos\theta_{1e}$, the net surface tension force is in the direction as in Fig. 2.2 and drives the liquid motion in the according direction. When $\frac{d_1}{d_2} > \cos\theta_{1e} > 0$, the net surface tension force is smaller than zero and could not drive the liquid motion. When the interface in the small conduit curves toward the opposite direction ($\cos\theta_{1e} < 0$), the liquid motion is going to be reversed, as if liquid 1 and liquid 2's positions are switched.

At long times, inertial terms can be neglected and one has a balance between surface tension and viscous forces, equation (2.12) reduces to

$$[C(1)l_{1t} + D(1)]\frac{dl_{1t}}{dt} = 4\gamma_{12}\frac{d_2^{\,2}}{d_1^{\,2}}\left(\frac{\cos\theta_1}{d_1} - \frac{d_2 - 2h}{d_2^{\,2}}\right). \qquad 2.15$$

In the above, $\theta_1 = \left[6\Gamma\cdot\left(\frac{\mu_1}{\gamma}\frac{dl_{1t}}{dt} + \delta\right)\right]^{1/3}$ and $h = 1.943\left(\frac{d_1^{\,2}}{d_2^{\,2}}\frac{\mu_1}{\gamma}\right)^{2/3}\left(\frac{dl_{1t}}{dt}\right)^{2/3}$. When the two fluids have the same viscosities $\mu_1 = \mu_2$, $C(1) = 0$. The time-dependent term in equation (2.15) drops out and time-independent flow is established.

Another special case occurs when one of the fluids is a gas (say, liquid 1). In this case, $\rho_1 << \rho_2$ and $\mu_1 << \mu_2$. In other words, one can neglect both the inertia and the viscous resistance of fluid 1. Equation (2.12) with $n = 1$ reduces to

$$\rho_2\left[\left(\frac{d_2^{\,2}}{nd_1^{\,2}}-\frac{nd_1^{\,2}}{d_2^{\,2}}\right)l_{1t}+\left(\frac{nd_1^{\,2}}{d_2^{\,2}}l_{10}+l_{20}\right)\right]\frac{d^2l_{1t}}{dt^2}+\rho_2\left(\frac{d_2^{\,2}}{nd_1^{\,2}}-\frac{nd_1^{\,2}}{d_2^{\,2}}\right)\left(\frac{dl_{1t}}{dt}\right)^2$$
$$+\frac{4(d_2-2h)\gamma}{nd_1^{\,2}}-\frac{4d_2^{\,2}}{nd_1^{\,3}}\gamma\cos\theta_1+\frac{32\mu_2}{d_2^{\,2}}\left[\left(\frac{d_2^{\,4}}{nd_1^{\,4}}-\frac{nd_1^{\,2}}{d_2^{\,2}}\right)l_{1t}+\left(\frac{nd_1^{\,2}}{d_2^{\,2}}l_{10}+l_{20}\right)\right]\frac{dl_{1t}}{dt}=0. \qquad 2.16$$

Furthermore, when the ratio of the diameters is large ($d_1/d_2 << 1$), and θ_1 is velocity-independent, equation (2.16) simplifies to the classical Bosanquet equation (Bosanquet 1923). This equation can be integrated once to yield

$$l_{1t}\frac{dl_{1t}}{dt}+\frac{16}{d_1^{\,2}}\nu_2 l_{1t}^{\,2}-\frac{4}{d_1}\frac{\gamma_{12}}{\rho_2}\cos\theta_1 t=0, \qquad 2.17$$

and again to yield

$$l_{1t}(t)=\sqrt{e^{-at}\left(\frac{b}{a^2+l_{10}^{\,2}}\right)+\frac{bt}{a}-\frac{b}{a^2}}, \qquad 2.18$$

where $a=\frac{16\nu_2}{d_1^{\,2}}$ and $b=\frac{4\gamma_{12}\cos\theta_1}{d_1\rho_2}$. When an analytical solution is not possible (i.e., when θ_1 is a function of the velocity), the equations can be readily integrated numerically to render l_{1t} as a function of t.

Equation (2.11) indicates that the velocity of the interface in the large conduit is significantly slower than that in the small conduit. When it is desirable to increase the velocity of the meniscus in the large conduit, a few smaller conduits can be combined in parallel. A few possible arrangements are depicted in Fig. 2.3.

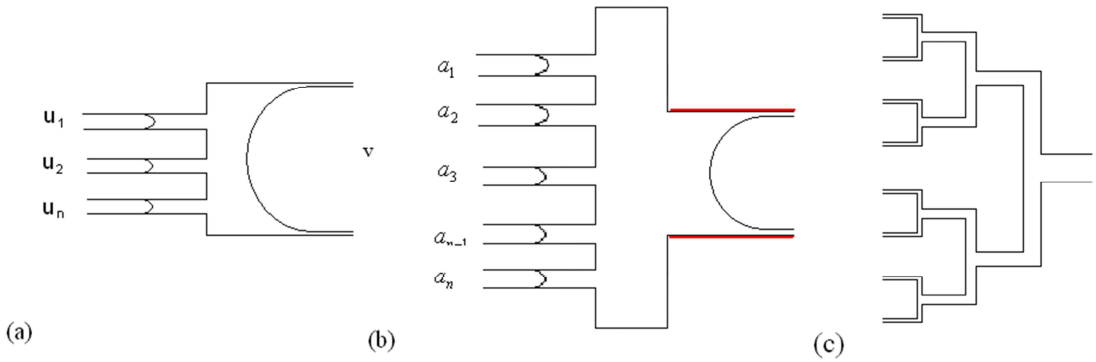

Figure 2.3 Various embodiments of multiple parallel small conduits connected to a single large conduit.

Below, we consider n small diameter conduits branching from a single large diameter conduit. In the arrangement depicted in Fig. 2.3a, the number of small conduits is restricted by the cross-sectional area of the large conduit. In the arrangement depicted in Fig. 2.3b, the number of small conduits is unrestricted.

The theory developed earlier in this section can be extended to accommodate the cases depicted in Fig. 2.3. To this end, we write $n+1$ momentum equations: n equations for the small conduits and one equation for the large conduit. The small conduits can vary in diameters facilitating various displacement rates in various conduits. To model the flow, we need to solve for n velocities u_i in the small conduits and the pressure differences across the length of each tube. For conciseness, we consider here only the case of n small conduits with identical diameters and initial menisci positions.

The lengths of the columns fluid 2 in the small tubes ($l_{1t}(t)$) can be calculated using equation (2.12) with $n>1$.

When liquid 1 is a gas and $\frac{d_2^{\,2}}{nd_1^{\,2}} >> 1$, equation (2.16) is identical to equation (2.17) and independent of n. In other words, when the sum of small tubes' cross-sectional areas is much smaller than the area of the large tube's cross-section, the number of small tubes does not affect the fluid motion in the individual small conduits. In contrast, the flow rate in the large conduit is proportional to the number

of the small conduits (n). Thus, by connecting a few small conduits to the large conduit, one can increase the average velocity of the liquid in the large conduit.

When $\frac{d_2^{\,2}}{nd_1^{\,2}} >> 1$ and the small conduits are identical in size but have different initial liquid menisci positions, the liquid motion in any small conduit can be predicted with equation (2.17) independently of the other small conduits. For example, consider a case with two small conduits branching from a large conduit. Figs. 2.4a and 2.4b depict, respectively, the liquid displacement in each of the small conduits when the ratio between the small conduits' diameter and large conduit's diameter is 0.4 and 0.5 and the initial lengths of the liquid columns are different ($l_{10} = 1cm$ and $l_{30} = 1mm$). The figures depict the predictions of the approximate model assuming that the small conduits (1 and 3) are independent of each other (denoted with 'a' in Fig. 4) and that accounts for the interdependence of the three momentum equations (denoted with 'e' in Fig. 2.4). When the diameter ratio is 0.4, the "approximate" and "exact" results coincide (Fig. 2.4a). When the diameter ratio is 0.5, there is a significant difference between the "approximate" and "exact" results (Fig. 2.4b). $d_2 = 1.98mm$, $\mu_1 = 0,\ \mu_2 = 0.0641Pa \cdot s,\ \gamma_{12} = 0.034N/m,\ \rho_1 = 0,\ \rho_2 = 830kg/m^3,\ l_{10} = 0.01m,$ $l_{20} = 0.01m,\ l_{30} = 0.001m$ and $\theta_1 = 57^o$. In (a), $d_1 = d_3 = 0.79mm$ and in (b) $d_1 = d_3 = 1mm$.

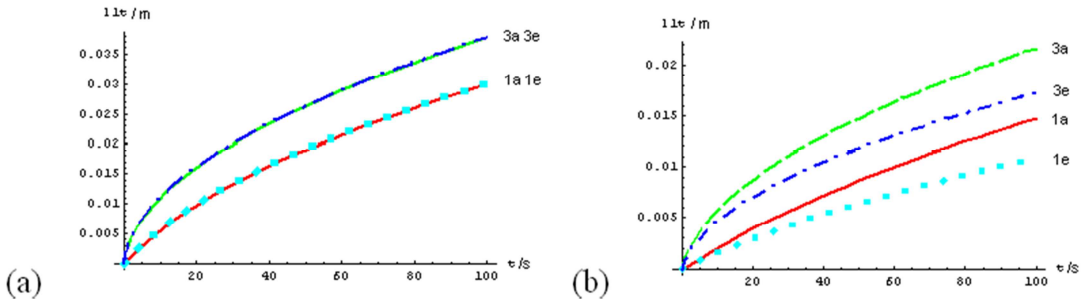

Figure 2.4 The displacement of the liquid column in the small conduits 1 and 3 when $\frac{d_2^{\,2}}{nd_1^{\,2}} >> 1$ (a) and $\frac{d_2^{\,2}}{nd_1^{\,2}} \sim 1$ (b). The subscripts e and a denote, respectively, the "exact" (coupled model) and "approximate" (uncoupled model) predictions.

The concepts described above can be extended to include multiple generations of branches as in Fig. 2.3c.

2.3 Optimization

Consider the case of a single large conduit of diameter d_2 and a single small conduit of diameter d_1, i.e., similar to the case depicted in Fig. 2.1. We denote the diameters' ratio $m = d_1/d_2$. As d_1 decreases, both the driving surface tension and the viscous drag increase albeit at different rates (see terms of equation (2.12)). One would expect therefore that there exists an optimal diameter ratio m that minimizes the amount of time that it takes the meniscus to cover a predetermined distance. Alternatively, one can seek the diameter ratio m that maximizes the length of the liquid displacement in the large conduit

$$J = m^2 l_{1t}(t_f)\,. \qquad 2.19$$

in the time interval $0 < t < t_f$. To find the optimal m that maximizes J, we start from equation (2.12) and assume that the contact angle is velocity-independent (i.e.,

$\theta_1 = \theta_e$ and $h = 0$). Below, we rewrite equation (2.12) in terms of m.

$$\left[(\rho_2-\rho_1)\left(\frac{1}{m^2}-m^2\right)l_{1t}+\rho_1\left(\frac{1}{m^2}l_1+l_2\right)+(\rho_2-\rho_1)\left(m^2 l_{10}+l_{20}\right)\right]\frac{d^2 l_{1t}}{dt^2}$$
$$+(\rho_2-\rho_1)\left(\frac{1}{m^2}-m^2\right)\left(\frac{dl_{1t}}{dt}\right)^2+\frac{4\gamma}{d_2}m^2\left(1-\frac{\cos\theta_e}{m}\right) \qquad . \qquad 2.20$$
$$+\frac{32}{d_2{}^2}\left[(\mu_1-\mu_2)\left(m^2-\frac{1}{m^4}\right)l_{1t}+\mu_1\left(\frac{1}{m^4}l_1+l_2\right)+(\mu_2-\mu_1)\left(m^2 l_{10}+l_{20}\right)\right]\frac{dl_{1t}}{dt}=0$$

As before, the above equation can be significantly simplified when liquid 1 is a gas. Further simplification can be obtained by realizing that the inertial forces play a significant role only for a short time interval after the onset of motion. We illustrate the effect of inertial forces through an example. Assuming liquid 1 to be a gas and neglecting its inertia and viscous drag, Fig. 2.5 depicts the normalized inertia terms (solid line) and the viscous drag (dotted line) of fluid 2 as functions of time. The forces were normalized with the surface tension force. Witness that the inertial force decays rapidly. When $t > 1.5ms$, the inertial force is smaller than 1% of the surface tension force and can be safely neglected.

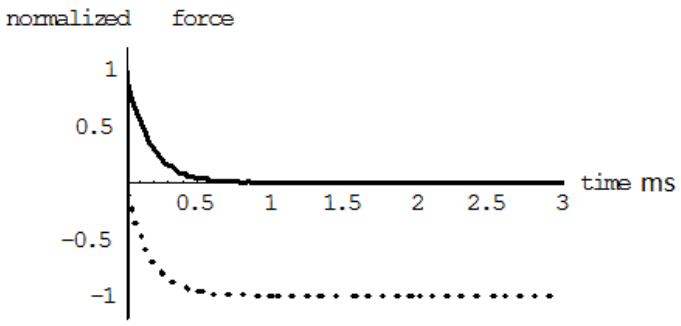

Figure 2.5 The normalized inertia (solid line) and viscous drag (dotted line) of liquid 2 are depicted as functions of time. The forces are normalized with the interfacial

force. $d_1 = 0.8mm,$ $d_2 = 2mm,$ $\rho_2 = 830kg/m^3,$ $\mu_2 = 0.064Pa \cdot s,$ $\gamma_{12} = 0.0229N/m$, $l_{10} = l_{20} = 0.01m$ and $\theta_e = 60^o$.

Assuming that fluid 1 is a gas and neglecting inertial terms, equation (2.20) reduces to

$$\frac{4\gamma}{d_2} m^2 \left(1 - \frac{\cos\theta_e}{m}\right) + \frac{32\mu_2}{{d_2}^2}\left[-\left(m^2 - \frac{1}{m^4}\right) l_{1t} + \left(m^2 l_{10} + l_{20}\right)\right]\frac{dl_{1t}}{dt} = 0. \qquad 2.21$$

The above equation can be integrated in closed form. Using the initial condition $l_{1t}(0) = l_{10}$ we get:

$$\left(m^2 - \frac{1}{m^4}\right)\left({l_{1t}}^2 - {l_{10}}^2\right) - 2\left(m^2 l_{10} + l_{20}\right)\left(l_{1t} - l_{10}\right) - \frac{d_2\gamma_{12}}{4\mu_2} m^2 \left(1 - \frac{\cos\theta_e}{m}\right) t_f = 0. \qquad 2.22$$

We now can express the objective function J explicitly as a function of m and t_f:

$$J = \frac{l_{10} + m^4 l_{20} - \sqrt{{l_{10}}^2 + 2m^4 l_{10} l_{20} + m^5\left[m^3 {l_{20}}^3 + \frac{d_2\gamma\left(\cos\theta_e - m\right)}{4\mu_2}\left(1 - m^6\right) t_f\right]}}{m^4 - \frac{1}{m^2}}. \qquad 2.23$$

Fig. 2.6 depicts J as a function of m when $t_f = 100s$. The solid line and the symbols correspond, respectively, to J values calculated with expression (2.19) and values calculated using the differential equations (without neglecting the inertial terms). The figure illustrates that equation (2.23) provides an excellent approximation for the objective function J and that an optimal diameter ratio m exists ($m_{opt} = 0.437$ for the conditions of Fig. 6) for which the displacement length can be optimized.

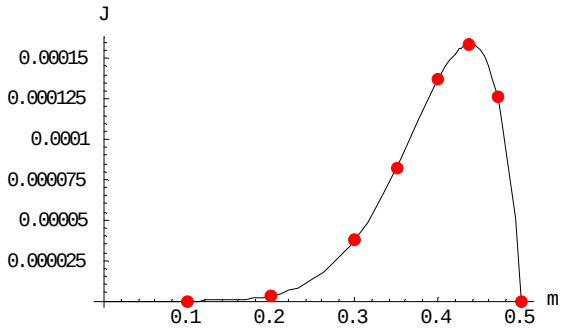

Figure 2.6 The objective function J is depicted as a function of the diameter ratio m. $\rho_2 = 830 kg/m^3$, $\mu_2 = 0.064 Pa \cdot s$, $\gamma_{12} = 0.0229 N/m$, $l_{10} = l_{20} = 0.01m$, $d_2 = 2mm$ and $\theta_1 = 60^o$. The solid line is obtained from equation (2.23). Red dots are obtained from brute force solution of equation (2.12).

2.4 Experiments

To demonstrate the validity of the theory and to illustrate that some of the ideas articulated in the theoretical section can be put into practice, we carried out a sequence of experiments. In the first set of experiments, we monitored a liquid slug displacing air as function of time in an open conduit of the type depicted in Fig. 2.3a. In the second set of experiments, we described the liquid-liquid displacement in a closed loop as in Fig. 2.1. In the third set of experiments, we describe a spontaneously moving phase change valve. In all the cases, a large tube empties into multiple small tubes ($n = 3$).

2.4.1 Liquid-Air Displacement

The experimental setup is shown in Fig. 2.7. The setup consists of three flexible Teflon tubes of diameter d_1 inserted into a large polycarbonate tube of

diameter d_2. Fluid 1 was a gas (*i.e.*, air). Fluid 2 was light paraffin oil.

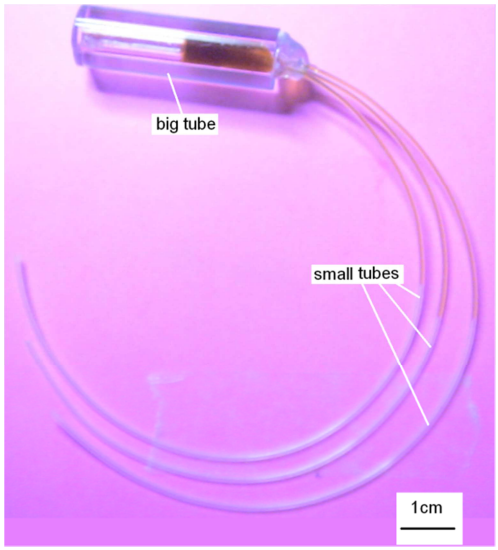

Figure 2.7 Experimental setup of a big polycarbonate tube connected with three small Teflon tubes. Dyed oil replaces air.

The thermophysical properties of the working fluids were either measured or were obtained from the vendors. To facilitate imaging of the transparent paraffin oil, we mixed the oil with oil-based ink (Speedball Inc.). The contact angle between the paraffin oil and a Teflon surface is estimated to be $36.6 \pm 4°$ (Brassard et al. 2008). The product $\gamma_{12} \cos\theta = 9.3 mN/m$ was measured by monitoring the capillary rise of a column of paraffin oil in a vertical Teflon capillary tube. We estimate $\gamma_{12} \sim 11.6 mN/m$. The viscosity of the clear paraffin oil was estimated to be $\mu_2 = 64.1 mPa \cdot s$ by measuring the terminal velocity of a settling particle suspended in the liquid. The density of the paraffin oil at $25°C$ is $\rho_2 = 830 kg/m^3$, obtained from the manufacturer's data.

Fig. 2.8 depicts the displacement of fluid 2 (l_{1t}) as a function of time. The solid lines and the symbols correspond to theoretical predictions and experimental

observations. The various symbols correspond to the different conditions listed in Table 2.1. The theoretical predictions are in good agreement with experimental observations with less than 9% discrepancy.

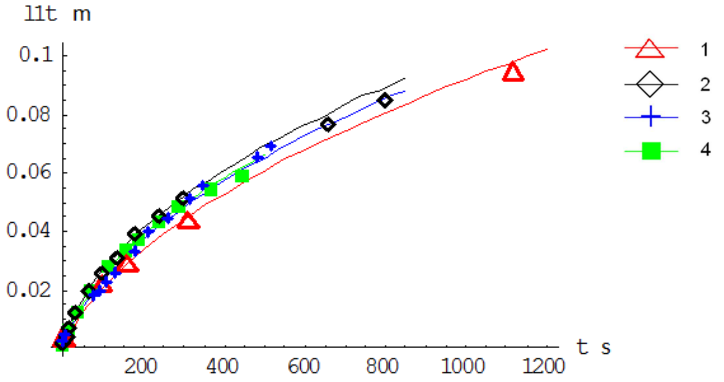

Figure 2.8 The displacement length l_{1t} is depicted as a function of time. The symbols and solid lines correspond, respectively, to the experimental data and the theoretical predictions. The small and large tubes are, respectively, made of Teflon and polycarbonate. The initial conditions are tabulated in Table 2.1.

The experiments were repeated with large conduits made of PVC and glass. Consistent with the theory presented in section 2, the material of the large conduit had little or no effect on the displacement as a function of time.

	1 (red, upright triangle)	2 (black rhombus)	3 (blue cross)	4 (green, solid square)
l_{10} (m)	0.015	0.005	0.0095	0.008
l_{20} (m)	0.015	0.01	0.013	0.017

Table 2.1 List of initial lengths of fluid 2 in the small and large conduits for Fig. 2.8.

2.4.2 Liquid-Liquid Displacement

In the above, we discussed the displacement of light paraffin oil with air. We

encountered, however, a few difficulties when attempting to carry out experiments with two liquids such as oil and water.

A small PVC tube was connected to a big glass tube at one end (Fig. 2.9). Depending on the sequence of injection, the PVC tube may be pre-wetted with paraffin oil (Fig. 2.10b) or not pre-wetted with paraffin oil (Fig. 2.10a). In the non-pre-wetted case (Fig. 2.10a), we observed no liquid motion once the other end of the two tubes were connected to form a closed loop. In the pre-wetted case (Fig. 2.10b), the oil-water interface in the small tube moved towards the water side on the existing oil film. The different phenomena resulting from these two set-ups are because that additional energy is required to develop a precursor film in front of the interface (Bico & Quere 2002). However, this motion did not last for long because of the interfacial instability between the core water thread and the surrounding oil film (see Fig. 2.11b). This instability caused a wavy interface. Disturbance amplified eventually to break the core water thread into isolated drops suspended in oil, which minimizes the surface energy. The water slugs had bullet shape and were asymmetric in the advancing and receding menisci. This caused additional resistance to the fluid motion and finally terminated the liquid displacement. Fig. 2.11d is an experimental picture which clearly displays the interfacial instability between the core (oil) and the water film along the hydrophilic glass tube’s wall.

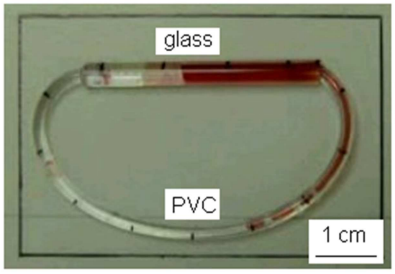

Figure 2.9 A big glass tube connected to a small PVC tube filled with clear paraffin oil and red dyed water. The counter clockwise motion starts when the PVC tube is pre-wetted with paraffin oil and ends when the core water thread breaks into slugs suspended in oil.

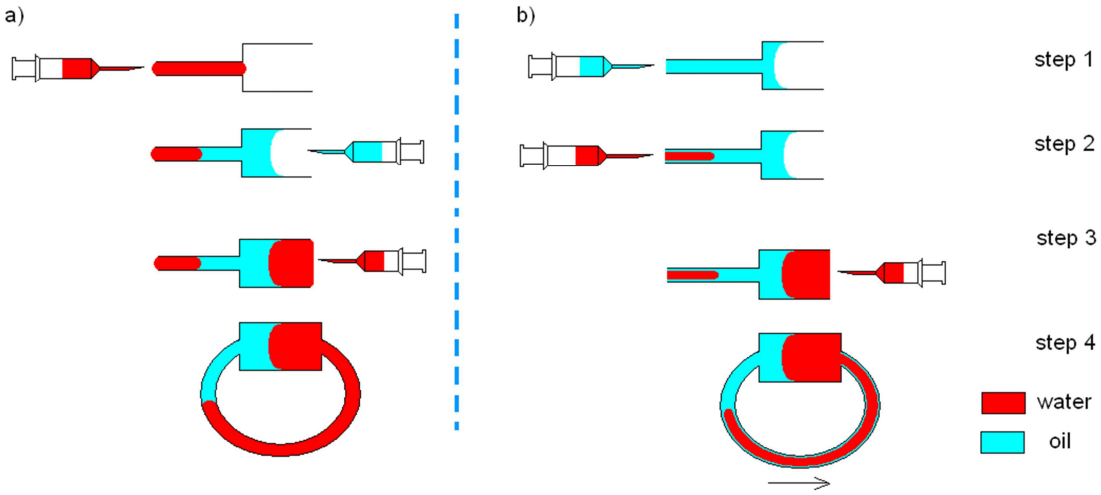

Figure 2.10 Filling sequence a) the small tube is not pre-wetted with paraffin oil. No motion is observed upon completing step 4. Filling sequence b) renders the entire small tube coated with a film of paraffin oil. Liquid motion sets up counter-clockwise at the completion of step 4. The motion slows down and finally stops when the water core starts forming isolated slugs surrounded by oil.

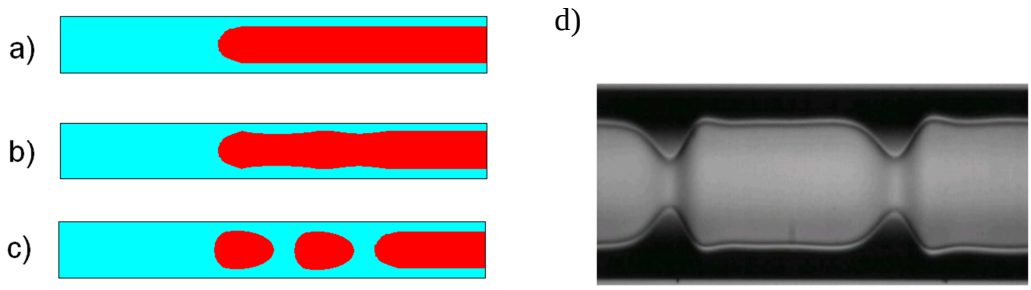

Figure 2.11 a) A schematic of the paraffin oil displacing water towards the right in a uniform tube. b) Instability develops as the liquids move, causing the annular flow interface transition to a wavy shape (known as the annular flow mode). c) Instability magnifies and the core thread of water breaks down into small droplets surrounded by oil, minimizing the surface energy (known as the Taylor flow mode). d) Experimental picture of oil (center thread) displacing water (outer film) in a $200\mu m$ diameter glass tube at flow rate $14.85\mu L/s$ towards the right (photo obtained in our collaborator Dr. Doyoung Byun's lab).

When we replace water with air in the above setup, the situation is much simpler. The oil displaces air easily without a need for pre-wetting oil film along the tube's surface. The oil slug proceeds smoothly until it occupies the entire length of the small tube.

2.4.3 A Thermally-Actuated Valve

To explore the possibility of using a spontaneously moving slug as a valve, we constructed the device shown in Fig. 2.12. Fig. 2.12a and b are, respectively, a schematic depiction and a photograph of the experimental device. The device was fabricated with polycarbonate. The device consists of a main, large conduit equipped

with a branching, side conduit **I** and three smaller conduits connected to the main conduit. One of the smaller conduits has also a branching side conduit. We used a low temperature melting fluid such as Steedman's wax (Staiger et al. 2000) (Sigma-Aldrich Inc.) as liquid 2. At room temperature, the wax was solid and blocked the conduit. Once the temperature was increased above the melting temperature ($T_m = 37°C$), the wax melted and motion set-up spontaneously.

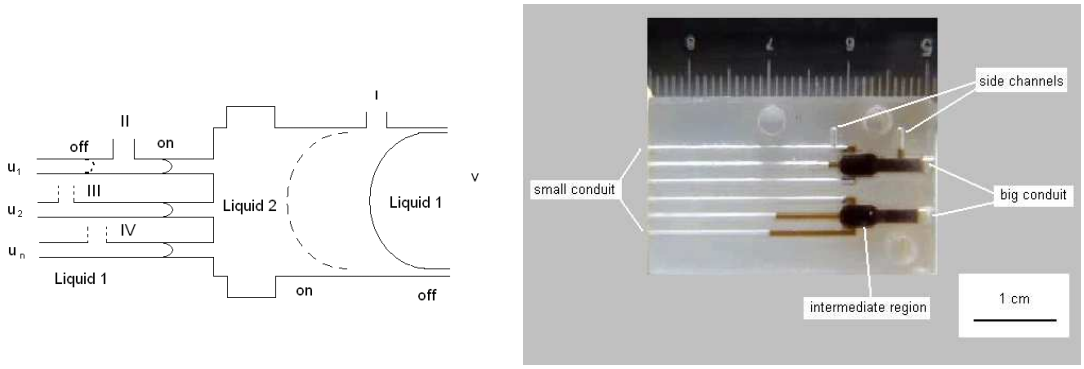

Figure 2.12 A conceptual embodiment of thermally-actuated phase change valve (a) and a device fabricated with polycarbonate b).

Initially, when the wax (substance 2) was solid, it blocked the passage from side branch **I** to the main tube **V** while passages **II**, **III**, and **IV** were maintained open. Upon the melting, the wax (fluid 2) moved spontaneously to open passage **I**. Depending on their position, passages **II**, **III**, **IV** could remain open or be closed either simultaneously or gradually. The timing of the closing of passages **II**, **III**, and **IV** can be controlled either by their position or by repetitive melting and freezing of the wax. The operation of the device is featured in a video available in the Supporting Information.

2.5 Discussion

According to our experimental observations, spontaneous liquid-air displacement is able to be achieved by designing the channel geometries and choosing the small tube material thus the interface curving direction.

The liquid-liquid displacement has more complications than the liquid-gas displacement. For example, the interface instability is dependent on the local roughness of the tube, the pre-wetting film thickness and other subtle factors, making it difficult to control.

Tube geometries other than cylindrical could also be used for the capillary pump. The Laplace pressure across the liquid-liquid or liquid-gas interfaces need to be calculated according to the tube cross-sections. Inner sharp corners in the cross-sectional geometry should be avoided, otherwise the more wetting liquid might run along the edges.

To further assist the phase change process, we may use mixture of wax and ferrofluids which has large quantities of metal particles inside, thus enhances the heat conduction. We may also use laser heating (Park et al. 2007) which claims to be able to achieve the phase change in seconds.

Here we established a theory which successfully predicts the experimental observations of liquid motion. The discrepancy between the theoretical calculation and the experimental data is less than 10%. There are several factors that may contribute to the discrepancies. First, the accumulated inaccuracies in the viscosity, surface tension and contact angle values of the liquid may be significant. Second, as the interfacial properties are highly sensitive to environmental conditions, the

temperature fluctuations in the surroundings may also lead to the difference between the theory and the experiment. Third, instead of having two straight sections of uniform cylindrical tubes as in the theory, we have curved small tubes for the experiments, which may cause additional curvature in the interface. Last but not least, our simplified theoretical model ignores the details of flow around the sudden step change in the tube diameters.

2.6 Conclusion

In this study we demonstrated the use of capillary force to spontaneously open or close a phase change valve. A one dimensional dynamic model predicted well the experimental results. We proposed an optimization scheme based on the dynamic model and get good agreement between the optimization result and the brute force solutions of the dynamic model. This valve was shown to be able to achieve both close to open and open to close switching within seconds.

CHAPTER 3: Electrolyte Response to AC / DC Polarizations

3.1 Introduction

Upon imposing an electric polarization, ions in the electrolyte are set in motion and participate in reactions: the motions take place in the liquid phase, including migration due to the electric potential gradient, diffusion due to the concentration gradient and convection when liquid motion presents; the electrochemical reactions take place at the electrode–electrolyte interfaces. The bulk electrolyte is electrically neutral and its performance is purely resistive, with the resistance depending on the local concentrations. The interface regions are rich in charges and are usually called the electric double layer (EDL), including a compact Stern layer and a diffuse layer. The EDLs are in dynamic equilibrium with the bulk under constant polarizations, performing as resistors. When time–dependent polarizations are present, the EDLs would undergo significant charging/discharging processes, showing capacitive behaviors. The ion transfer kinetics could be described by the Poisson equation and the Nernst–Planck (NP) equations (PNP model) (Bonnefont et al. 2001). In the bulk electrolyte where neutrality holds, the electric potential doesn't need to be solved. However, in the EDLs where neutrality condition fails, the Poisson equation needs to be solved, which is coupled to the ion concentrations. Due to the great difference between the length scales of the bulk and the EDL, the mesh generation and numerical calculation become difficult, which call for a proper description of the EDL, such as an equivalent boundary condition for the bulk. The electrochemical reactions on the electrode surfaces are often described by the Butler–Volmer type equation for

Faradaic current injection. This highly non–linear boundary condition further complicates the problem.

We study the response of a model one–dimensional electrochemical thin film to both time–independent and time–dependent applied polarizations. For the time–independent case, Bazant et al. 2005 carried out a matched asymptotic study for thin EDL situation and compared the asymptotic solution with the numerical results. We examine the ion transport in four different kinds of electrolyte and applied current/voltage conditions. Both numerical simulations and analytical solutions are obtained. In the time–dependent case, Bazant et al. 2004 studied the response of a symmetric binary electrolyte to a step change voltage, using linearized PNP equations with the Laplace transforms for small voltages and obtained numerical solutions for large voltages. Their analysis was based on ideally polarizable (blocking) electrodes where no current injection is possible. We solved the full PNP model for both ideally polarizable electrodes and current injection electrodes, in the context of a tri-ion RedOx electrolyte. A simplified model studying only the electro-neutral bulk is developed, under the proper boundary conditions that capture the capacitive–resistive behavior of the double layer. The simplified model is then validated by comparing its result with that from the corresponding full model.

3.2 Theory

Consider a pair of parallel plate electrodes located at $x = 0$ and L, respectively. The space in between the electrodes is filled with an electrolyte solution. Once an electric polarization (current or potential difference) is applied at the electrodes, the

transport of the i-th species c_i is governed by the Nernst-Planck equation:

$$\frac{\partial c_i}{\partial t} = -\nabla \cdot \vec{m}_i \quad (i = 1, ..., l), \tag{3.1}$$

where the mass flux of species i,

$$\vec{m}_i = \vec{u} c_i - D_i \nabla c_i - z_i \nu_i F \nabla \phi, \tag{3.2}$$

consists of convective, diffusive and electro-migrative terms. In the above, D_i and $\nu_i = D_i / (RT)$ are, respectively, the diffusivity and the mobility of the i-th species. z_i is the valance of the i-th ion. l is the total number of ion species. F is the Faraday constant. ϕ is the electric potential. For static electrolytes that we consider in this chapter, the convective term vanishes.

The electric potential satisfies the Poisson equation:

$$-\nabla \cdot (\varepsilon_s \nabla \phi) = F \sum_{i=1}^{l} z_i c_i, \tag{3.3}$$

where ε_s is the dielectric permittivity of the solvent. The current flux in the bulk electrolyte equals the sum of the ions' net charge flow:

$$\vec{j}_b = F \sum_{i=1}^{l} z_i \vec{m}_i, \tag{3.4}$$

For reversible reactions at the electrodes' surfaces: $Ox + ne^- \Leftrightarrow Red$, the species' fluxes are given by the Butler-Volmer (BV) equation (Newman & Thomas-Alyea 2004):

$$\vec{n} \cdot \vec{m}_{Red} = \frac{j_0}{F} \left[\frac{c_{Ox,d/b}}{c_{Ox,ave}} e^{(-\alpha nF/RT)(v - \phi_{d/b})} - \frac{c_{Red,d/b}}{c_{Red,ave}} e^{[(1-\alpha)nF/RT](v - \phi_{d/b})} \right] = -\vec{n} \cdot \vec{m}_{Ox}, \tag{3.5}$$

where α is the charge transfer coefficient for the cathodic reaction, n is the number of electrons exchanged in the reaction, j_0 is the exchange current's density,

c_{Ox} and c_{Red} are, respectively, the concentrations of the oxidized and reduced species. Subscript ave and d/b refers to the average in the bulk and the interface of the diffuse layer and the bulk, respectively. When multiple reactions take place at the electrodes' surfaces, a separate BV equation is needed for each reacting pair. The net current flux at the surface of the electrode is:

$$\vec{j}_E = F\left(z_{Red}\vec{m}_{Red} + z_{Ox}\vec{m}_{Ox}\right) \qquad 3.6$$

Typically, the bulk of the solution is electrically neutral (EN):

$$\sum_{i=1}^{l} z_i c_i = 0\,. \qquad 3.7$$

When considering the electrolyte response to fixed potential, the EDL is in equilibrium and the current flux across the EDLs is invariant: $\vec{j}_E = \vec{j}_b$. Equation (3.1-3.3) will be solved, subjecting to the boundary conditions in equation (3.5). However, using the EN condition in equation (3.7), the potential and concentrations in the NP equations could be decoupled and no separate equation for potential needs to be solved. The potential doesn't satisfy Laplace equation though, which seems a straight forward conclusion from equations (3.3) and (3.7). The RHS of equation (3) will be a second order small quantity if asymptotic analysis is carried out as in Bazant et al. 2005.

The full PNP model (equations 3.1-3.3) needs to be solved for the AC problem for both the Debye layer and the bulk, since charge equilibrium and EN condition both fail in the Debye layer. A suitable boundary condition is shown as in Fig. 3.1, with the stern layer acting as a capacitor of capacitance c_s in parallel with a

nonlinear resistor. The electric current is able to pass through the resistor path, allowing Faradaic current injection, and meanwhile charge/discharge the capacitor, adjusting the potential difference across the stern layer.

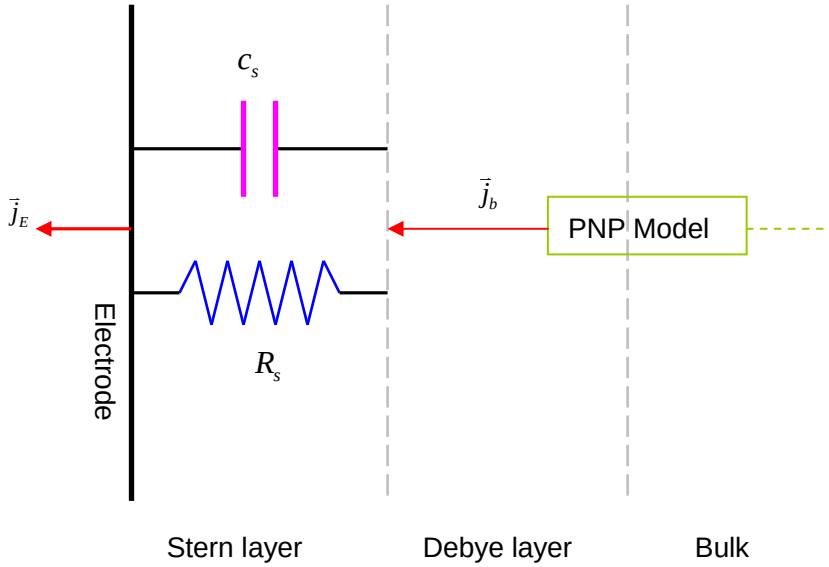

Figure 3.1 A physical picture of the electrolyte structure with electric double layers next to one of the electrodes. Circuit element was drawn to illustrate the boundary conditions for the full PNP model.

From the stern model, which assumes the capacitance of the compact layer c_s to be constant, two Robin type boundary conditions could be obtained for the Poisson equation (Bazant et al. 2005):

$$\begin{aligned} \phi(0) - \lambda_s \frac{d\phi}{dx}(0) &= v(0) \\ \phi(L) + \lambda_s \frac{d\phi}{dx}(L) &= v(L) \end{aligned}, \qquad 3.8$$

Here $\lambda_s = \frac{\varepsilon_s}{c_s}$ is the effective thickness of the compact layer. v are the externally applied potentials at the electrodes. These boundary conditions could be understood as extrapolating the potential across the thickness of the stern layer.

Since the EDL thickness is usually in the nm range and is much smaller than the distance between the electrodes, numerical difficulty is expected in solving the full problem. A proper model that studies only the electroneutral bulk but still captures the behavior of the electrochemical cell is stated as below, with equivalent boundary conditions as sketched in Fig. 3.2.

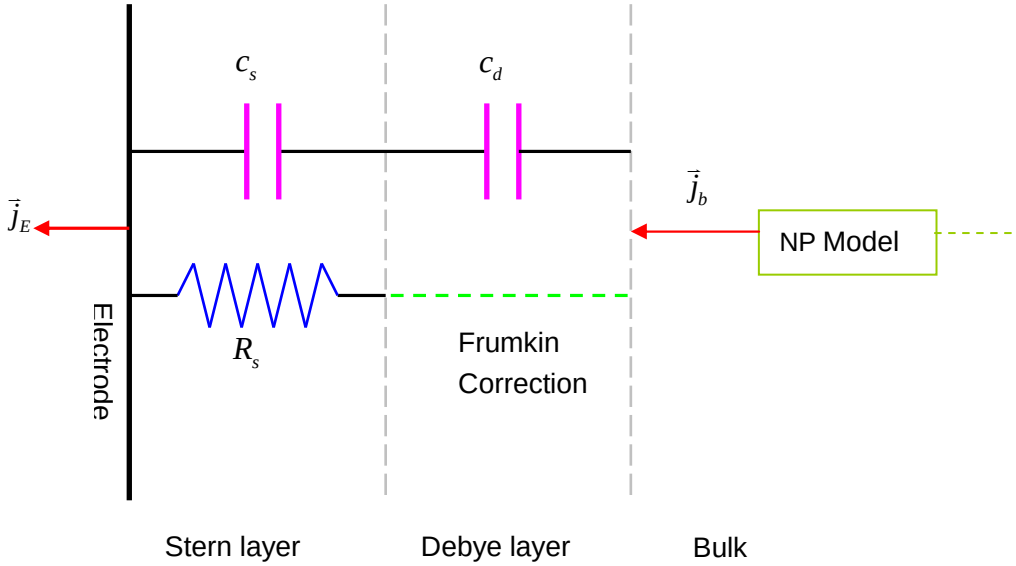

Figure 3.2 A physical picture of the electrolyte structure with electric double layers next to one of the electrodes. Circuit element was drawn to illustrate the boundary conditions for the reduced NP model.

Note that the BV equation is used only across the compact layer, which means that in equation (3.6), concentrations and potential at the d/b interfaces should be replaced by the corresponding quantities at the s/d interfaces. This is called the Frumkin correction to the BV condition (Frumkin 1955). For Gouy–Chapman profiles for the equilibrium diffuse layer at leading order,

$$c_{\pm} \sim e^{\mp(\phi-\phi_{d/b})}, \qquad 3.9$$

The concentration at the s/d and the d/b interfaces are related by:

$$\frac{c_{Ox,s/d}}{c_{Ox,d/b}} = e^{-\varsigma}, \frac{c_{Red,s/d}}{c_{Red,d/b}} = e^{\varsigma} \tag{3.10}$$

where $\varsigma = \phi_{s/d} - \phi_{d/b}$ is the zeta potential.

The capacitance of the stern layer and the diffuse layer are as following:

$$c_s = \frac{\varepsilon_s}{\lambda_s}, c_d = \frac{\varepsilon_s}{\lambda_d}. \tag{3.11}$$

The diffuse layer capacitance could also be obtained by numerically extrapolate the potential profile from the PNP results and relate the time derivative of the capacitive voltage and the injection current. The total capacitance of the two layers can be calculated as:

$$c_0 = \frac{1}{\frac{1}{c_s} + \frac{1}{c_d}} = \frac{\varepsilon_s}{\lambda_s + \lambda_d} \tag{3.12}$$

The potential drop across the stern layer and the Debye layer would be proportional to their capacitances, which means that

$$\frac{v - \phi_{s/d}}{\phi_{s/d} - \phi_{d/b}} = \frac{c_d}{c_s} = \delta, \tag{3.13}$$

where $\delta = \lambda_s / \lambda_d$. The potential drop across the stern layer:

$$v - \phi_{s/d} = \frac{\delta}{1+\delta}(v - \phi_{d/b}) \tag{3.14}$$

For time dependent applied potential, a general form for the EDL charging and discharging is:

$$c_0 \frac{d(v - \phi_{d/b})}{dt} = j_E - j_b, \tag{3.15}$$

When the applied potential is periodic and of the form e^{iwt}, we have:

$$\frac{\phi_{e/s}-\phi_{d/b}}{j_E-j_b}=\frac{1}{iwc_0}, \qquad 3.16$$

where $i=\sqrt{-1}$ and w is the frequency.

The dimensionless equations that normalize distance, concentrations, potentials, current densities and time with L, $\overline{c}_1$, RT/F and $D_1F\overline{c}_1/L$, L^2/D_1 are:

$$\frac{\partial C_i}{\partial T}=-\frac{D_i}{D_1}\frac{\partial M_i}{\partial X}\ \ (i=1,....,l),\ \ \vec{M}_i=-\frac{\partial C_i}{\partial X}-z_iC_i\frac{\partial \Phi}{\partial X} \qquad 3.17$$

$$-\varepsilon^2\frac{\partial^2\Phi}{\partial X^2}=\frac{1}{2}\sum_{i=1}^{l}z_iC_i \qquad 3.18$$

$$\vec{n}\cdot\vec{M}_{Red}=J_0\left[\frac{C_{Ox,d/b}}{C_{Ox,b}}e^{-\Psi/\delta-\alpha n\Psi}-\frac{C_{Red,d/b}}{C_{Red,b}}e^{\Psi/\delta+(1-\alpha)n\Psi}\right]=-\vec{n}\cdot\vec{M}_{Ox} \qquad 3.19$$

$$\begin{aligned}\Phi(0)-\delta\varepsilon\frac{d\Phi}{dX}(0)&=V(0)\\ \Phi(1)+\delta\varepsilon\frac{d\Phi}{dx}(1)&=V(1)\end{aligned} \qquad 3.20$$

$$\int_{X=0}^{1}C_i=C_{i0} \qquad 3.21$$

$$\vec{J}_b=\sum_{i=1}^{l}z_i\vec{M}_i \qquad 3.22$$

$$\vec{J}_E=z_{Red}\vec{M}_{Red}+z_{Ox}\vec{M}_{Ox} \qquad 3.23$$

$$C_0\frac{d(V-\Phi_{d/b})}{dT}=J_E-J_b \qquad 3.24$$

and for sinusoidal applied potential: $\dfrac{V-\Phi_{d/b}}{J_E-J_b}=\dfrac{1}{iwC_0}$ 3.25

where $\Psi=(V-\Phi_{d/b})\dfrac{\delta}{1+\delta}$, $\varepsilon=\lambda_d/L$, $\lambda_d=\sqrt{\dfrac{\varepsilon_sRT}{2c_1F^2}}$, $C_s=\dfrac{2\varepsilon}{\delta}$, $C_d=2\varepsilon$ and $C_0=\dfrac{2\varepsilon}{1+\delta}$.

3.3 Time-Independent Applied Polarizations

In this section, we study the steady state response of an electrolyte to a fixed applied potential/ current. The electric double layer would be in equilibrium in all these cases and only the electro-neutral bulk needs to be considered. Electric current is conserved in the entire domain of interest. We thus have $J = J_E$ everywhere in the direction perpendicular to the surface of the electrodes.

3.3.1 A symmetric binary electrolyte ($A^{z_1+}B^{z_1-}$) under current density j_0

As in the case of electroplating, only the cations participate in the electrode reactions (assume single electron transfer): $A^{z_1+} + z_1 e^- \Leftrightarrow A(s)$. The anode is made of $A(s)$ so that the total numbers of A^{z_1+} and B^{z_1-} ions both remain constants according to time. The governing equations for the unknowns C_1, C_2 and Φ:

$$\begin{aligned} &\frac{dC_1}{dX} + z_1 C_1 \frac{d\Phi}{dX} = -\frac{J_E}{z_1} \\ &\frac{dC_2}{dX} - z_2 C_2 \frac{d\Phi}{dX} = 0 \\ &z_1 C_1 - z_2 C_2 = 0 \end{aligned} \qquad 3.26$$

Assume $z_1 = z_2 = 1$ are the charges of the cations and anions, respectively. We have $C_1 = C_2$ everywhere from the electro-neutrality equation (3.26-3). Adding and subtracting equations (3.26-1) and (3.26-2) decouples the concentrations and potential, leading to the solutions

$$\begin{aligned} C_1 = C_2 &= 1 + \frac{J_E}{2}\left(\frac{1}{2} - X\right) \\ \Phi &= \ln\left[\frac{1 + \frac{J_E}{2}\left(\frac{1}{2} - X\right)}{1 + \frac{J_E}{4}}\right] \end{aligned} \qquad 3.27$$

that satisfy the mass conservation of $\int_{X=0}^{1} C_i dX = 1$ and boundary condition $\Phi(0) = 0$.

We solved numerically the dimensionless Nernst-Planck problem using COMSOL and the compared the numerical results with the analytical results, shown as in Fig. 3.3.

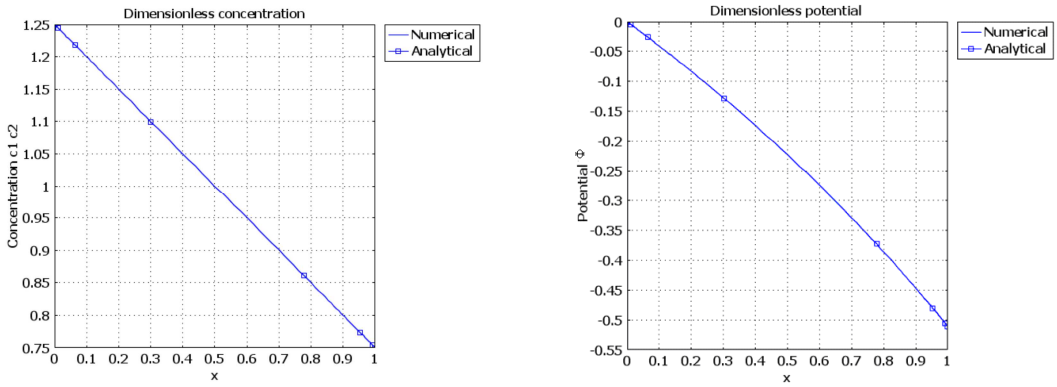

Figure 3.3 Comparison of COMSOL numerical solutions (solid line) and analytical solutions (solid line with symbols) as in equation (33). a) dimensionless concentrations; b) dimensionless potential.

3.3.2 A binary electrolyte ($A^{z_1+}B^{z_2-}$) under applied potential V

Consider two ion species with charge number z_1 and z_2 co-exist in the electrolyte. The electrode reaction is: $A^{z_1+} + z_1 e^- \Leftrightarrow A(s)$. The dimensionless ion concentrations satisfying the mass transfer equations as following:

$$\begin{aligned} &\frac{dC_1}{dX} + z_1 C_1 \frac{d\Phi}{dX} = -\frac{J_E}{z_1} \\ &\frac{dC_2}{dX} - z_2 C_2 \frac{d\Phi}{dX} = 0 \\ &z_1 C_1 - z_2 C_2 = 0 \end{aligned} \quad . \qquad 3.28$$

Instead of having a constant current flux going through the electrolyte, we impose

potentials of 0 and V on the electrodes.

The boundary conditions can be written as:

$$\begin{aligned} J_E &= J_0\left\{C_1(0)e^{(1-\alpha)z_1\Phi(0)} - e^{-\alpha z_1\Phi(0)}\right\} \; at \;\; X=0 \\ J_E &= J_0\left\{e^{-\alpha z_1[\Phi(1)-V]} - C_1(1)e^{(1-\alpha)z_1[\Phi(1)-V]}\right\} \; at \;\; X=1 \end{aligned} \tag{3.29}$$

The mass conservations are now:

$$\int_{X=0}^{1} C_1 dX = 1, \int_{X=0}^{1} C_2 dX = \frac{z_1}{z_2}, \tag{3.30}$$

Equations (3.28) yield the solution for the concentrations:

$$C_1(X) = 1 + \frac{J_E z_2}{z_1\left(z_1+z_2\right)}\left(\frac{1}{2} - X\right) = \frac{z_1}{z_2}C_2(X) \tag{3.31}$$

and for the potential drop in electrolyte:

$$\Delta\Phi = \Phi(1) - \Phi(0) = \frac{1}{z_2}\ln\frac{J^1 + J_E}{J^1 - J_E} \tag{3.32}$$

where $J^1 = \dfrac{2z_1\left(z_1+z_2\right)}{z_2}$ is the dimensionless limiting diffusion-migration current in the cell, corresponding to the ion depletion condition $C_1(0) = 0$.

Using the solution in equations (3.31) and (3.32) to eliminate $\Phi(0)$ from equations (3.29) leads to an implicit expression for the polarization curve $J_E(V)$. A convenient form is obtained as the following equations (3.33) and (3.34):

$$E = e^{z_1\Phi(0)} = \frac{1 + e^{\alpha z_1\left[V - \frac{1}{z_2}\ln\left(\frac{J^1+J_E}{J^1-J_E}\right)\right]}}{1 - \frac{J_E}{J^1} + \left(1 + \frac{J_E}{J^1}\right)e^{(1-\alpha)z_1\left[\frac{1}{z_2}\ln\left(\frac{J^1+J_E}{J^1-J_E}\right) - V\right]}} \tag{3.33}$$

$$J_E = J_0 E^{-\alpha}\left[\left(1 - \frac{J_E}{J^1}\right)E - 1\right] \tag{3.34}$$

The solutions to equations (3.33) and (3.34) are plotted as in Fig. 3.4. Finite element

simulations of the problem with COMSOL for different parameters of J^1 and α are also plotted as in Fig. 3.4.

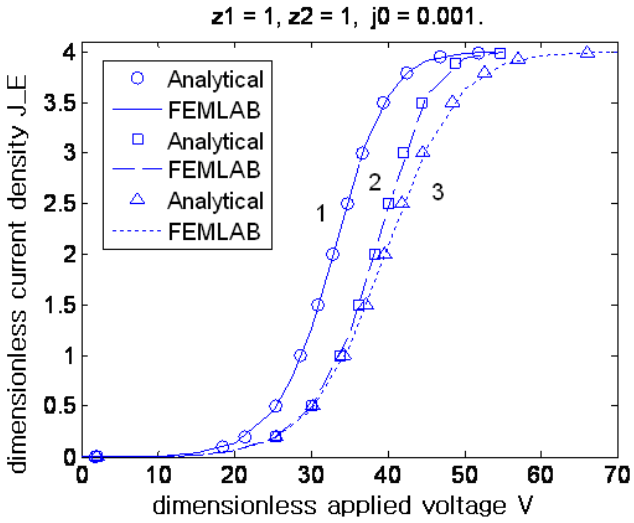

Figure 3.4 Polarization curve $J_E(V)$ determined analytically by equation (39) and (40) (symbols) and by COMSOL simulations (lines). $z_1 = z_2 = 1, J_0 = 0.001$. 1) $\alpha = 0.5$; 2) $\alpha = 0.3$; 3) $\alpha = 0.7$.

3.3.3 A binary electrolyte ($A^{z_1+}C^{z_3-}$) with supporting electrolyte ($B^{z_2+}C^{z_3-}$) under applied potential V

Assume three types of ions A^{z_1+}, B^{z_2+} and C^{z_3-} co-exist in the electrolyte, with their concentrations C_1, C_2 and C_3 satisfying the non-dimensional time independent NP and EN equations:

$$\begin{aligned} &\frac{dC_1}{dX} + z_1 C_1 \frac{d\Phi}{dX} = -\frac{J_E}{z_1} \\ &\frac{dC_2}{dX} + z_2 C_2 \frac{d\Phi}{dX} = 0 \\ &\frac{dC_3}{dX} - z_3 C_3 \frac{d\Phi}{dX} = 0 \\ &z_1 C_1 + z_2 C_2 = z_3 C_3 \end{aligned} \quad . \qquad 3.35$$

The solution to C_2 *and* C_3 can be obtained as in Grigin 1993:

$$C_2(X) = C_2(0)e^{-[\Phi(X)-\Phi(0)]}$$
$$C_3(X) = NC_2(0)e^{[\Phi(X)-\Phi(0)]} \qquad 3.36$$

Multiplying equation (3.35-1), (3.35-2) and (3.35-3) by z_1, z_2 *and* $-z_3$ respectively and summing them together, then reduce with equation (3.35-4) to get: (for case of $z_1 = 2, z_2 = z_3 = 1$)

$$\frac{dX}{d\Phi} = \frac{1}{J_E}\left(3C_3 - C_2\right) \qquad 3.37$$

The mass conservation for ions (the concentrations are scaled to $\overline{c}_3$, the ratio $\frac{\overline{c}_1}{\overline{c}_3} = k$, bar denotes average):

$$\int_{X=0}^{1} C_1 dX = k,\ \int_{X=0}^{1} C_2 dX = 1-2k,\ \int_{X=0}^{1} C_3 dX = 1. \qquad 3.38$$

Denote

$$\Delta\Phi = \Phi(1) - \Phi(0) \qquad 3.39$$

and

$$y = e^{2\Delta\Phi} \qquad 3.40$$

Substitute equation (3.36) to (3.38) for mass conservation for C_2 and C_3 to get the following expressions:

$$\frac{C_2(0)^2}{2J_E}\left(3N\ln y + y^{-1} - 1\right) = 1-2k \qquad 3.41$$

$$\frac{NC_2(0)^2}{2J_E}\left[3N\left(y-1\right) - \ln y\right] = 1 \qquad 3.42$$

Reduce (3.41) and (3.42) to get the expression for N as a function of y:

$$N(y) = (2-k)\ln y + \frac{\sqrt{(2-k)^2 \ln^2 y + 3(y-1)(y^{-1}-1)(1-2k)}}{3(y-1)(1-2k)} \qquad 3.43$$

The integration of equation (3.37) from $\Phi(0)$ to $\Phi(1)$ equals 1, leads to the expressions of $C_2(0)$ and J_E as functions of N and y:

$$C_2(0) = \frac{2(3N - y^{-1/2})(y^{1/2}-1)}{N\left[3N(y-1) - \ln y\right]} \qquad 3.44$$

$$J_E = \frac{2\left[3N(y^{1/2}-1) + y^{-1/2} - 1\right]^2}{N\left[3N(y-1) - \ln y\right]} \qquad 3.45$$

Equations (3.44) and (3.45) together with the electro-neutrality condition (3.35-4) and (3.36) yield the following expression for $C_1(0)$ and $C_1(1)$ in terms of N and y:

$$\begin{aligned} C_1(0) &= \frac{1}{2}\left(N-1\right)C_2(0) \\ C_1(1) &= \frac{1}{2}\left(Ny^{1/2} - y^{-1/2}\right)C_2(0) \end{aligned} \qquad 3.46$$

If the currents at the electrodes are related to the concentrations and over-potentials by the Butler-Volmer boundary conditions:

$$\begin{aligned} J_E &= J_0\left\{\frac{C_1(0)}{k}e^{2(1-\alpha)\Phi(0)} - e^{-2\alpha\Phi(0)}\right\} \; at \;\; X = 0 \\ J_E &= J_0\left\{e^{-2\alpha[\Phi(1)-V]} - \frac{C_1(1)}{k}e^{2(1-\alpha)[\Phi(1)-V]}\right\} \; at \;\; X = 1 \end{aligned} \qquad 3.47$$

Equating the right hand side of equations (3.47-1) and (3.47-2) and note that $\Phi(1) = \Phi(0) + \ln\sqrt{y}$, $\Phi(0)$ could be expressed in terms of y and V:

$$e^{2\Phi(0)} = \frac{1 + e^{2\alpha(V - \ln\sqrt{y})}}{\frac{C_1(1)}{k}e^{2(1-\alpha)(\ln\sqrt{y} - V)} + \frac{C_1(0)}{k}} \qquad 3.48$$

Equations (3.45), (3.47-1) and (3.48) can be calculated numerically for the $J_E(V)$ curve.

We used $k = 1/3, \alpha = 0.5, J_0 = 1, V = 1$. We solved the problem with COMSOL and compared the analytical and numerical results as shown in Fig . 3.5.

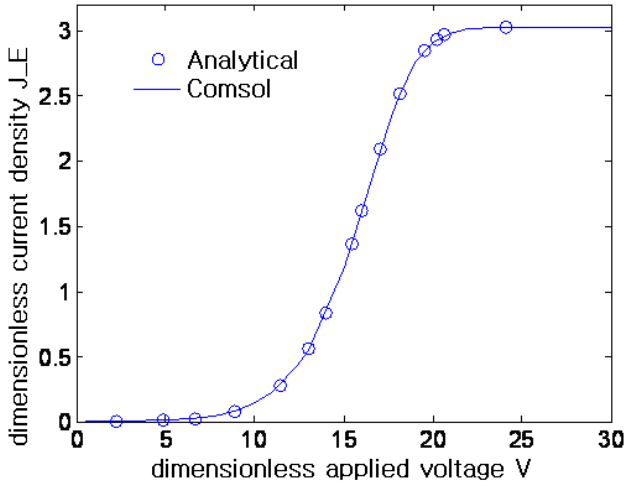

Figure 3.5 Comparison of the current – voltage relation calculated by analytical solution (symbols) and the COMSOL simulation results (solid line).

3.3.4 A RedOx electrolyte ($A^{z_1+}C^{z_3-} / B^{z_2+}C^{z_3-}$) under an applied potential V

Two types of cations undergo RedOx reaction: $A^{z_1+} + (z_1 - z_2)e^- \Leftrightarrow B^{z_2+}$. The mass transfer equations and the electro-neutrality equations are as following:

$$\begin{aligned} &\frac{dC_1}{dX} + z_1 C_1 \frac{d\Phi}{dX} = -\frac{J_E}{z_1 - z_2} \\ &\frac{dC_2}{dX} + z_2 C_2 \frac{d\Phi}{dX} = \frac{D_1}{D_2} \cdot \frac{J_E}{z_1 - z_2} \\ &\frac{dC_3}{dX} - z_3 C_3 \frac{d\Phi}{dX} = 0 \\ &z_1 C_1 + z_2 C_2 = z_3 C_3 \end{aligned} \qquad 3.49$$

Assume $z_1 = 3, z_2 = 2, z_3 = 1$. The concentrations are scaled to $\bar{c}_3$, $\frac{\bar{c}_1}{\bar{c}_3} = k$. Summing equations (3.55-1), (3.55-2) and (3.55-3) yields:

$$C_1 + C_2 = J_E\left(1 - \frac{D_1}{D_2}\right)\cdot\left(\frac{1}{2} - X\right) + \frac{3-k}{2} - C_3 \qquad 3.50$$

Multiplying equation (3.49-1) with $\frac{D_1}{D_2}$, adding it with equation (3.49-2) and use $\frac{d\Phi}{dX} = \frac{1}{C_3}\frac{dC_3}{dX}$ from equation (3.49-3) yields:

$$\left[12\frac{D_1}{D_2}C_1 + \left(6 + 2\frac{D_1}{D_2}\right)C_2\right]dC_1 + \left[\left(3 + 6\frac{D_1}{D_2}\right)C_1 + 6C_2\right]dC_2 = 0 \qquad 3.51$$

The solution to equation (3.51) could be obtained numerically. In the following, we will consider the simplest case of the fixed ratio of diffusion coefficients $\frac{D_1}{D_2} = \frac{3}{4}$ so that equation (3.51) can be integrated to be (Kharkats et al. 1995):

$$(C_1 + C_2)(3C_1 + 2C_2) = m \qquad 3.52$$

Here m is an integration constant.

The above equation (3.52) is equivalent to:

$$C_3^{\,2} - \left[\frac{J_E}{4}\cdot\left(\frac{1}{2} - X\right) + \frac{3-k}{2}\right]C_3 + m = 0 \qquad 3.53$$

Leading to:

$$C_3 = \frac{b + \sqrt{b^2 - 4m}}{2} \qquad 3.54$$

where $b = \frac{J_E}{4}\cdot\left(\frac{1}{2} - X\right) + \frac{3-k}{2}$.

For a given k value, we could obtain numerically m as a function of J_E through the conservation of mass for C_3. The expressions of the concentrations are as following:

$$C_1 = 3C_3 - 2b \qquad 3.55$$

$$C_2 = 3b - 4C_3$$

$$C_3 = \frac{b + \sqrt{b^2 - (1-k)^2}}{2}$$

For the Butler-Volmer boundary condition,

$$\begin{aligned} J_E &= J_0 \left\{ \frac{C_1(0)}{k} e^{(1-\alpha)\Phi(0)} - \frac{C_2(0)}{(1-3k)/2} e^{-\alpha\Phi(0)} \right\} \; at \;\; X = 0 \\ J_E &= J_0 \left\{ \frac{C_2(1)}{(1-3k)/2} e^{-\alpha[\Phi(1)-V]} - \frac{C_1(1)}{k} e^{(1-\alpha)[\Phi(1)-V]} \right\} \; at \;\; X = 1 \end{aligned} \qquad 3.56$$

From equation (3.55-1), (3.55-2) and (3.56), we are able to obtain:

$$e^{\Phi(0)} = \frac{2k}{1-3k} \cdot \frac{C_2(0) + C_2(1)\exp^{\alpha(V-\Delta\Phi)}}{C_1(0) + C_1(1)\exp^{(\alpha-1)(V-\Delta\Phi)}} \qquad 3.57$$

The numerical solution for the $J_E \sim V$ curve could be obtained from equation (3.56-1), (3.57) and $\Delta\Phi$ from integrating $\frac{d\Phi}{dX} = \frac{1}{C_3}\frac{dC_3}{dX}$. We find out that m is just weakly dependent on J_E (Fig. 3.6). We assume $J_E = 0$ and obtain $m = \frac{1-k}{2}$. Using this m value does lead to almost identical solutions of the $J_E \sim V$ relation.

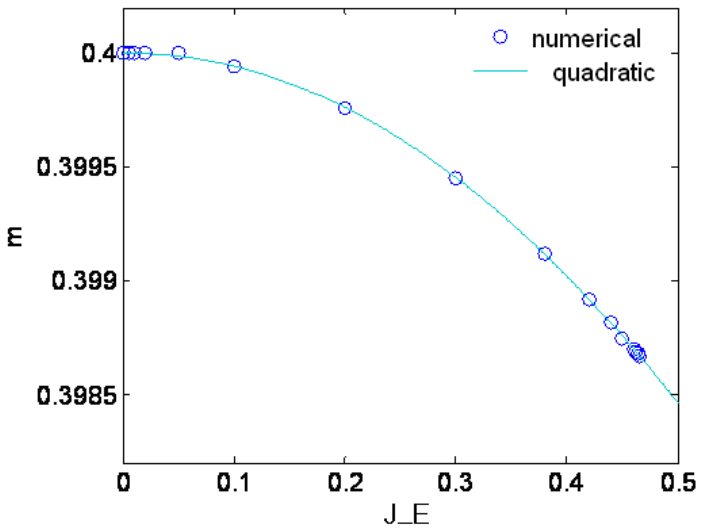

Figure 3.6 $m \sim J_E$ curve from analytical solution (symbols) and a quadratic fitting

curve (solid) from the mass conservation.

The numerical solutions of m at different J_E values are plotted as in Fig. 3.6. The comparison of $J_E \sim V$ curves of the COMSOL simulation result and the analytical solution as developed above is shown in Fig. 3.7.

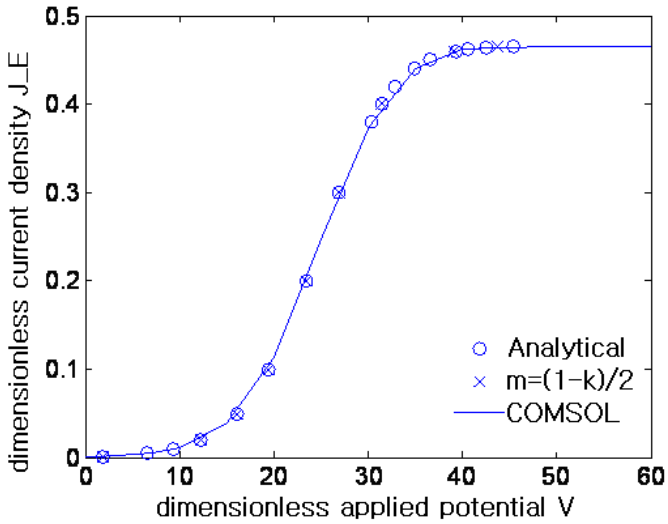

Figure 3.7 $J_E \sim V$ curve from analytical solution with exact m values as in Fig. 7 (circles), analytical solution with $m = (1-k)/2$ (cross symbols) and COMSOL simulation (solid line). $\alpha = 0.5, k = 0.2, J_0 = 0.001$.

3.4. Time-Dependent Applied Polarizations

First we consider the case of ideally polarizable electrodes, where the ionic fluxes vanish at the electrodes. A model problem studied by Bazant et al. 2004 is a dilute, completely disscociated $z:z$ electrolyte, limited by two parallel, planar, blocking electrodes at $x = \pm L$ and with applied potentials $\pm v$. When the applied potential is much smaller than the thermal voltage ($v << k_b T/ze$), the equations could be linearized into the Debye-Falkenhagen equation and Laplace transform gives a

solution of the problem, as could be found in Bazant et al. 2004 part IV. Performing the numerical inverse Laplace transform by Mathematica, we're able to obtain the potential and concentration distribution exactly the same as in Bazant et al. 2004 for different parameters. The comparison between the numerical Laplace inversion solution and the COMSOL solution are plotted as in Fig. 3.8. The electrodes are located at dimensionless coordinate $X = \pm 1$ and are subjected to dimensionless potentials ± 0.1.

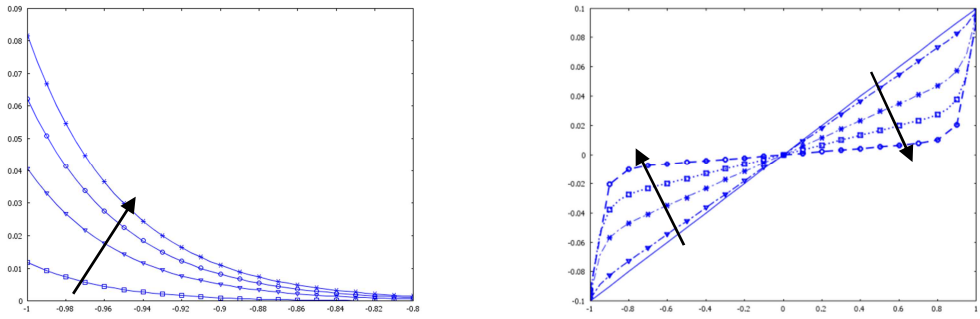

Figure 3.8 Dimensionless charge density $\rho = (C_1 - C_2)/2$ (within the EDL close to the left electrode $-1 < X < -0.8$) and dimensionless potential Φ for dimensionless voltage $V = 0.1$. Lines correspond to $t = 0$, 0.1, 0.5, 1 and 2 according to directions shown. $t = 0$ in the left figure overlaps with the x-axis and is not shown.

The reduced model described by equations (3.17)-(3.25) is numerically solved with COMSOL. The comparison of the full and reduce ion transport model with Butler-Volmer type of current injection is shown as in Fig. 3.9. The applied potential is of magnitude $V = 0.1$ and frequency $w = \pi$. $\delta = 0.1$. $\varepsilon = 0.05$. $J_0 = 0.001$. $\alpha = 0.5$.

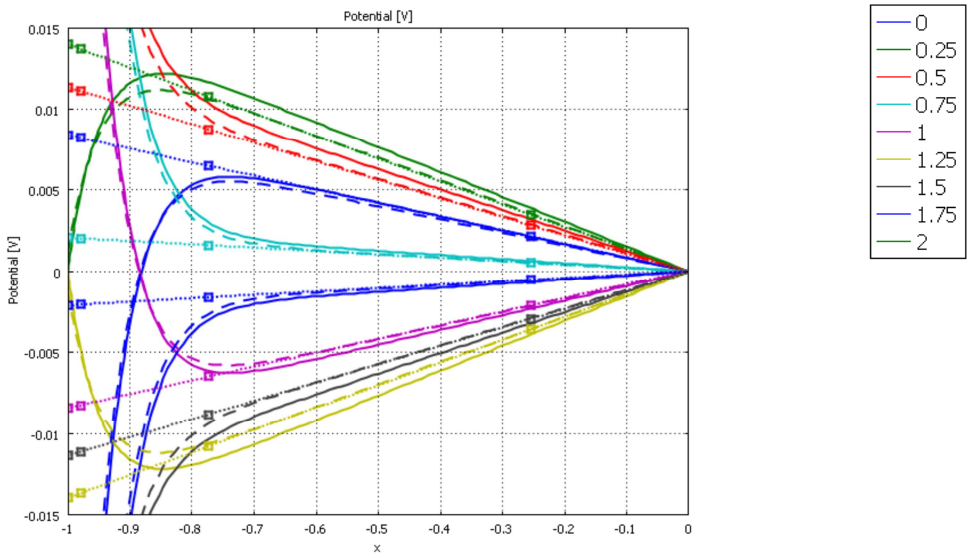

Figure 3.9 Comparison of the full PNP model with extrapolation boundary condition for the stern layer (dashed lines), full PNP model with leaky capacitor model for the stern layer (solid lines) and reduced NP model with leaky capacitor model for the EDL (dotted lines with symbols). Results are based on binary electrolyte (1:1) subjected to applied potential with magnitude $V = 0.1$ and frequency $w = \pi$. Different colors correspond to $T = 0 : 0.25 : 2$. $\delta = 0.1$. $\varepsilon = 0.05$. $J_0 = 0.001$. $\alpha = 0.5$. Half domain of the symmetric response is shown.

We also included in both the Fig. 3.10 and Fig. 3.11 the full model with a capacitor type of boundary condition for the stern layer, which is close to but different from the result from the linear extrapolation type of boundary condition as in equation (3.20). Note that for applied potential $V = 0.1\cos(\pi T)$, the time response of the reduced model agrees with the full models only after $T > 0.2$.

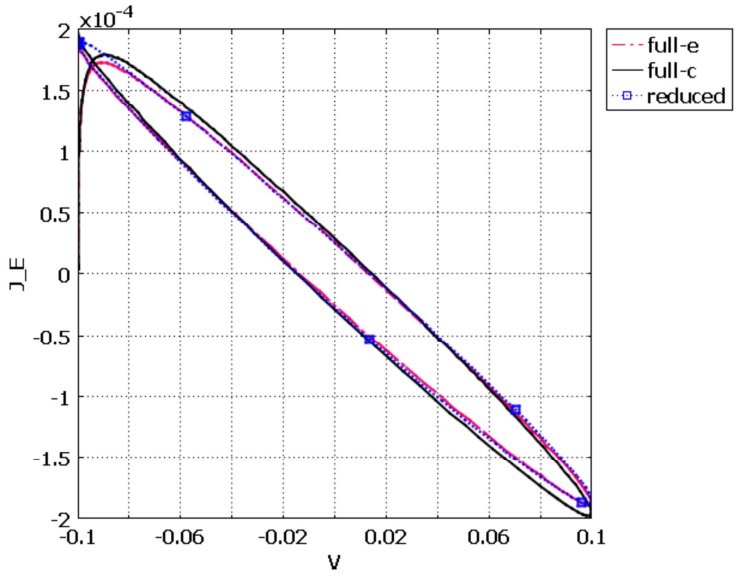

Figure 3.10 Dimensionless current injection J_E as functions of dimensionless applied potential V from the full PNP model with extrapolation boundary condition for the stern layer (red dash dotted line), the full PNP model with leaky capacitor model for the stern layer (black solid line) and the reduced NP model with leaky capacitor model for the EDL (blue dotted line with symbols). $V = 0.1$. $w = \pi$. $\delta = 0.1$. $\varepsilon = 0.05$. $J_0 = 0.001$.

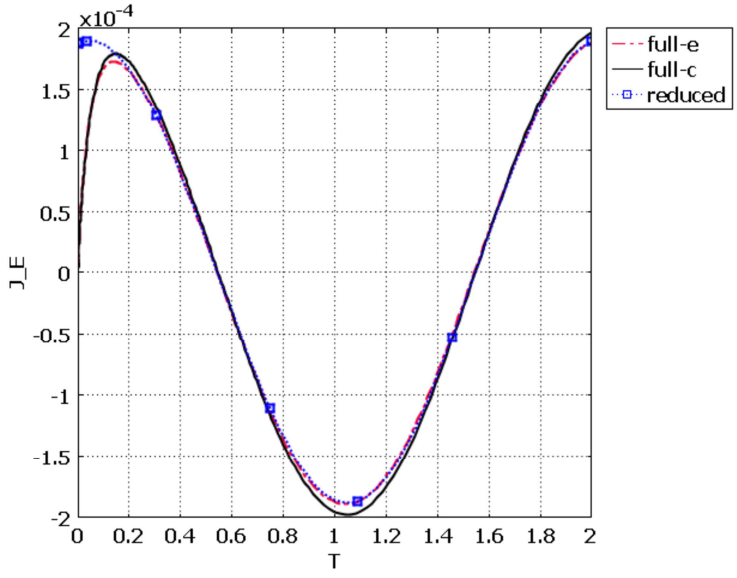

Figure 3.11 Current injection J_E as functions of time from the full PNP model with extrapolation boundary condition for the stern layer (red dash dotted line), the full model with leaky capacitor model for the stern layer (black solid line) and the reduced model with leaky capacitor model for the EDL (blue dotted line with symbols). $V = 0.1$. $w = \pi$. $\delta = 0.1$. $\varepsilon = 0.05$. $J_0 = 0.001$.

3.5 Conclusion

The physical model of a one dimensional electrolytic cell was summarized. The DC responses to applied current/ potential were studied for four cases of electrolytes by solving the electroneutral Nernst-Planck equations. The current-voltage relations were obtained analytically and compared to the numerical results. The AC response were obtained by solving the full Poisson-Nernst-Planck model. A reduced model accounting only the electroneutral bulk was developed, with proper boundary conditions for the non-neutral double layers. The results from the full and reduced model were compared to verify the validity of the reduced model, which overcomes the numerical difficulty associated with the distinct size difference between the double layer and the electrolytic cell.

CHAPTER 4: Magneto-Hydrodynamic Flow around Cylinders

4.1 Introduction

A lab-on-a-chip (LOC) device is a minute chemical processing plant that integrates on a single substrate common laboratory processes ranging from filtration and mixing to separation and detection. To achieve these tasks, it is often necessary to propel and stir liquids and control fluid flow. Since, in many applications, one uses solutions that are electrically conductive, one can transmit electric currents through these solutions. When the device is subjected to an external magnetic field provided by either permanent magnets or electromagnets, the electric current interacts with the magnetic field to produce Lorentz body forces, which, in turn, drive fluid motion. This phenomenon is commonly referred to as magneto-hydrodynamics and has been utilized, among other things, to pump fluids in microfluidic conduits (Qian and Bau 2005; Jang and Lee 2000; Lemoff and Lee 2000; Leventis and Gao 2001; West *et al.* 2002 and 2003; Zhong *et al.* 2002; Eijkel *et al.* 2003; Bao and Harrison 2003a and 2003b; Arumugam *et al.* 2005 and 2006; Aguilar *et al.* 2006; Nguyen and Kassegne 2008), control fluid flow in microfluidic networks without a need for mechanical pumps and valves (Bau *et al.* 2003); stir and mix fluids (Bau *et al.* 2001; Yi *et al.* 2002; Xiang and Bau 2003; Qian and Bau 2005; Gleeson and West 2002; West *et al.* 2003; Gleeson *et al.* 2004); and enhance mass transfer next to electrodes' surfaces (Boum and Alemany 1999; Lioubashevski *et al.* 2004; Alemany and Chopart 2007). For a recent review of a few applications of MHD in microfluidics, see Qian and Bau (2009).

Most of the literature pertaining to MHD focuses on liquid metals and ionized gases (Davidson 2001). In contrast, in microfluidic applications, one typically deals with electrolyte solutions. The modeling of MHD flows of electrolyte solutions differs from that of liquid metals since the local electric conductivity is a function of the electrolytes' concentration, which, in turn, depends on the flow field. Nernst-Plank equations for the ions' flux (Newman 1991), the Navier-Stokes momentum equation (Batchelor 1967), and Maxwell's equations for the magnetic field need to be solved concurrently. Additionally, one often needs to consider non-linear electrode kinetics and the possible production of undesirable products of electrochemical reactions at the electrodes' surfaces. Another potential undesired phenomenon is electrophoretic migration of charged molecules and particles in the electric fields induced by the electrodes.

Fortunately, for electrolytes with low magnetic permittivity and a low magnetic Reynolds number, the determination of the magnetic field can be decoupled from that of the ion concentration, fluid flow, and electric fields, and electric current induction can be neglected.

The typical MHD pump consists of an electrolyte-filled conduit with a rectangular cross-section whose opposite walls are coated with electrodes. It has long been known that when the electrolytes are subjected to a uniform magnetic field directed parallel to the electrodes' surfaces, the MHD flow is equivalent to pressure-driven flow (Ho 2007). We show that this equivalence also exists in some other circumstances that are common in microfluidic systems. We utilize the

equivalence between MHD-driven flow and pressure-driven flow to obtain the flow patterns of MHD flow in conduits patterned with pillar arrays. Such conduits can serve as chromatographic and separation columns and as catalytic reactors. The pillars provide increased surface area and solid support for stationary phases and catalytic surfaces (to facilitate and enhance heterogeneous reactions). MHD–driven flow is of particular interest to chromatography as it allows one to drive fluid flow in a closed loop, in effect, providing an "infinitely long column" (Martin 1958; Eijkel *et al.* 2004). In a traditional, linear, separation column, the column length must be selected in advance, which is not always feasible when dealing with unknown analytes or with analytes that have slightly different partition coefficients. No such advance knowledge is needed in the case of the closed loop chromatograph. The closed-loop chromatograph also allows for real-time detection.

In the case of the column patterned with the pillar array, we show that when the current is controlled (known), one can deduce the MHD flow rate by using literature data available for pressure-driven flow in a similar geometry. When the potential difference between the electrodes is the control parameter, the equivalence between the pressure-driven flow and the MHD-driven flow cannot be applied directly to obtain the flow field, and we solve the coupled Nernst-Planck and Navier-Stokes equations to obtain the concentration, current, and flow fields. In the latter case, we can verify the computations by comparing our computed drag coefficients with literature data available for the pressure-driven flow.

This chapter is organized as follows. Section 4.2 introduces the mathematical

model and outlines the various assumptions that apply for the conditions typically prevailing in microfluidic systems. Section 4.3 proves the existence of a "Lorentz potential" under special conditions and thus the equivalence between MHD-driven and pressure-driven flow under those conditions. Section 4.4 reviews briefly MHD flow in a uniform conduit. The analysis accounts for concentration gradients induced by the electric field. Additionally, we redefine the efficiency of the MHD pump energy conversion and estimate the temperature increase in the MHD pump. Section 4.5 studies MHD flow in a conduit patterned with a pillar array. Section 4.6 studies Taylor dispersion associated with MHD flow in a rectangular conduit. Section 4.7 concludes.

4.2 Mathematical Model

Consider an electrolyte solution consisting of l types of ionic species with concentrations c_i $(i=1,....,l)$ subjected to external electric and magnetic fields. The mass transport of the i-th ion is described by the Nernst-Planck (**NP**) equation:

$$\frac{\partial c_i}{\partial t} = -\nabla \cdot \mathbf{N}_i \qquad (i=1,...,l), \tag{4.1}$$

where the mass flux of species i

$$\mathbf{N}_i = \mathbf{u}c_i - D_i \nabla c_i - z_i \nu_i F c_i (\nabla \phi - \mathbf{u}\times\mathbf{b}) \tag{4.2}$$

is comprised of convective, diffusive, electro-migrative, and inductive terms. In the above, $\mathbf{u}$ is the fluid velocity; D_i and $\nu_i = D_i/(RT)$ are, respectively, the diffusivity and the mobility of the i-th ion species; z_i is the valence of the i^{th} ion species; R is the gas constant; T is the absolute temperature; F is the Faraday

constant; ϕ is the electric potential; and $\mathbf{b}$ is the magnetic field vector. We adopt here the convention that bold and regular letters represent, respectively, vectors and scalars.

The electric potential satisfies the Poisson equation:

$$-\nabla\cdot\left(\varepsilon_s\nabla\phi\right)=F\sum_{i=1}^{l}z_i c_i\,, \tag{4.3}$$

where ε_s is the dielectric permittivity of the solvent.

Typically, in a homogeneous solution, net charge exists only in narrow regions next to solid surfaces (electric double layers, **EDL**) and the bulk of the solution is nearly electrically neutral:

$$\sum_{i=1}^{l}z_i c_i\approx 0\,. \tag{4.4}$$

The electric current flux is

$$\mathbf{j}=F\sum_{i=1}^{l}z_i\mathbf{N}_i=-F\sum_{i=1}^{l}z_i D_i\nabla c_i-\sigma_{ionic}(\nabla\phi-\mathbf{u}\times\mathbf{b})\,, \tag{4.5}$$

where $\sigma_{ionic}=F^2\sum_{i=1}^{l}z_i^{\,2}\nu_i c_i$ is the ionic conductivity of the electrolyte solution.

The fluid motion satisfies the Navier-Stokes (**NS**) equation:

$$\rho\left(\frac{\partial\mathbf{u}}{\partial t}+\mathbf{u}\cdot\nabla\mathbf{u}\right)=-\nabla p+\mu\nabla^2\mathbf{u}+\mathbf{f}_{EM}\,, \tag{4.6}$$

where the electromagnetic body force

$$\mathbf{f}_{EM}=\mathbf{f}_L+\mathbf{f}_{\nabla B}+\mathbf{f}_E\,. \tag{4.7}$$

The Lorentz force

$$\mathbf{f}_L=\mathbf{j}\times\mathbf{b}\,; \tag{4.8}$$

the magnetophoretic force (when the ions are ferromagnetic and/or paramagnetic)

$$\mathbf{f}_{\nabla B} = \frac{\chi_m}{2\varsigma_0} c_i^{(m)} \nabla \mathbf{b}^2; \qquad 4.9$$

and the electrostatic force

$$\mathbf{f}_E = F \nabla \phi \cdot \sum_{i=1}^{l} z_i c_i . \qquad 4.10$$

In the above, ρ and μ are, respectively, the fluid density and viscosity; $\varsigma_0 = 1.257 \times 10^{-6} N \cdot A^{-2}$ is the magnetic permeability of the vacuum; p is the dynamic pressure; χ_m is the molar susceptibility; and the subscript m denotes paramagnetic ions. Due to the small dimensions of microfluidic conduits, we neglected buoyancy effects in equation (4.6). We emphasize, however, that body forces due to density variations may, on occasion, play a significant role even when device dimensions are relatively small. See, for example, Qian *et al*. (2006).

The electrolyte satisfies the continuity equation:

$$\nabla \cdot \mathbf{u} = 0 . \qquad 4.11$$

Equations (4.1-4.11) constitute the standard model.

In the model presented above, we neglected the induced magnetic field. This is justified since, in all our applications, the magnetic Reynolds number $\mathrm{Re}_m = \frac{\bar{u}H}{\upsilon} << 1$.

In the above, $\bar{u}$ is the average flow velocity; H is a length scale associated with the flow; and $\upsilon = (\varsigma_0 \sigma_{ionic})^{-1}$ is the "magnetic diffusivity". For example, when $\bar{u} = 1mm/s$, $H = 1mm$ and $\sigma_0 = 1.29 ohm^{-1} m^{-1}$ (0.1M KCl at $25^o C$), $\mathrm{Re}_m \sim 10^{-12}$ and the magnetic induction can be safely neglected. This approximation is valid even

in the case of liquid metals. For example, in the case of mercury (conductivity of $10^6 ohm^{-1}m^{-1}$), $\mathrm{Re}_m \sim 10^{-6}$. Thus, in what follows, we assume that the external, imposed magnetic field is unperturbed by the flow.

When the applied magnetic field is uniform ($\mathbf{b} = |\mathbf{b}|\mathbf{e}_z$) and the bulk of the electrolyte solution satisfies the electro-neutrality condition, both $\mathbf{f}_{\nabla B}$ and $\mathbf{f}_E$ vanish, leaving the Lorentz force as the only body force. The dimensionless Navier-Stokes equation becomes:

$$\mathrm{Re}\left(\frac{\partial \hat{\mathbf{u}}}{\partial \hat{t}} + \hat{\mathbf{u}}\cdot\hat{\nabla}\hat{\mathbf{u}}\right) = -\hat{\nabla}\hat{p} + \hat{\nabla}^2\hat{\mathbf{u}} - \mathrm{K}\sum_{i=1}^{l} z_i \hat{D}_i\left(\hat{\nabla}\hat{c}_i + z_i\hat{c}_i\hat{\nabla}\hat{\phi}\right)\times\hat{\mathbf{b}} + \mathrm{Ha}^2(\hat{\mathbf{u}}\times\hat{\mathbf{b}})\times\hat{\mathbf{b}} \qquad 4.12$$

.

In the above, $Ha = H|\mathbf{b}|\sqrt{\frac{\sigma_{ionic}}{\mu}}$ is the Hartmann number. The velocity, length, time, concentration, potential, magnetic field, pressure and diffusion coefficients are, respectively, scaled with $u_0 = \frac{F^2 H|\mathbf{b}| D_0 \bar{c}_q \Delta V_{ext}}{\mu RT}$, the conduit's height H, $\frac{u_0}{H}$, the average concentration $\bar{c}_q$, $\frac{RT}{F}$, $|\mathbf{b}|$, $\frac{\mu u_0}{H}$, and $D_0 = \sum_{i=1}^{l}\frac{1}{|z_i|}\Big/\sum_{i=1}^{l}\frac{1}{D_i}$. $\mathrm{Re} = \frac{\rho u_0 L}{\mu}$ is the Reynolds number. $\mathrm{K} = \frac{F|\mathbf{b}| D_0 \bar{c}_q H}{\mu u_0}$ is the ratio between the Lorentz force and the viscous force.

The dimensionless current $\hat{\mathbf{j}} = \frac{\mathbf{j}}{j_0} = -K\sum_{i=1}^{l} z_i \hat{D}_i\left(\nabla\hat{c}_i + z_i\hat{c}_i\nabla\hat{\phi}\right) + \mathrm{Ha}^2\left(\hat{\mathbf{u}}\times\hat{\mathbf{b}}\right)$, where $j_0 = \frac{\mu u_0}{H^2|\mathbf{b}|}$. ΔV_{ext} is the externally applied potential difference. Overhats denote dimensionless quantities and overbars denote domain averages. When the Hartmann number is small, the induction current term in equation (4.12) can be neglected. This is generally the case in microfluidic systems operating with

electrolyte solutions. For example, when $H = 1mm$, $|\mathbf{b}| = 0.4T$, $\mu = 10^{-3} Pa \cdot s$ and $\sigma_{ionic} \sim 1 ohm^{-1} m^{-1}$ (0.1M KCl at $25^o C$), the Hartmann number $Ha \sim 10^{-2}$. In contrast, in the case of liquid metals such as mercury (conductivity $10^6 ohm^{-1} m^{-1}$), $Ha \sim 10$ and the induction current term in equation (4.12) must be taken into account.

Equation (4.4) suggests that there is no accumulation of charge in the bulk of the solution. Therefore, the current flux is solenoidal (divergence free).

$$\nabla \cdot \mathbf{j} = 0 . \qquad 4.13$$

Applying equation (4.13) to equation (4.5) and neglecting the induction term, we obtain the equation for the electric potential in the bulk of the solution:

$$\nabla \cdot \left(\sigma_{ionic} \nabla \phi \right) + F \sum_{i=1}^{l} z_i \nabla \cdot \left(D_i \nabla c_i \right) = 0 . \qquad 4.14$$

Witness that equation (4.14) reduces to Ohm's law only when one can neglect the term $F \sum_{i=1}^{l} z_i \nabla \cdot \left(D_i \nabla c_i \right)$. This would be the case when all the ionic species have similar diffusivities or when the concentration distributions are nearly uniform. The flow field affects equation (4.14) indirectly through its effect on the concentration field (equation 4.2).

When reversible reactions of the type $Ox + ne^- \Leftrightarrow Red$ take place at the electrodes' surfaces, the species' fluxes at the electrodes' surfaces are given by the Butler-Volmer (**BV**) equation:

$$\mathbf{n} \cdot \mathbf{N}_{Red} = \frac{j_e}{F} \left[\frac{c_{Ox}}{\bar{c}_{Ox}} e^{(-\alpha nF/RT)\eta} - \frac{c_{Red}}{\bar{c}_{Red}} e^{[(1-\alpha)nF/RT]\eta} \right] = -\mathbf{n} \cdot \mathbf{N}_{Ox} , \qquad 4.15$$

where j_e is the exchange current flux, α is the charge transfer coefficient for the cathodic reaction, n is the number of electrons exchanged in the reaction, $\eta = \phi - V_{ext}$ is the overpotential, and c_{Ox} and c_{Red} are, respectively, the concentrations of the oxidized and reduced species at the electrodes' surfaces. **n** is a unit vector normal to the electrode's surface directed away from the fluid. When concurrent, multiple reactions take place at the electrodes' surfaces, a separate BV equation is needed for each reacting pair. All solid surfaces, other than the electrodes, are impermeable.

The boundary conditions associated with the momentum equation are no slip at all solid surfaces. In the problems considered here, we specify periodic conditions for the flow velocities at the inlet and outlet.

Electrical neutrality exists in the bulk of the solution, but not next to solid surfaces. Typically a surface in contact with an aqueous solution acquires a net charge, which attracts counterions to form a thin (a few nanometers in thickness) electrical double layer consisting mostly of counterions. The electric field's component tangent to the surface propels the ions in the electric double layer and gives rise to electroosmotic flow. When the device's length scale is much greater than the thickness of the EDL, the flow in the EDL is approximated by the Smoluchowski slip velocity (Probstein 1994):

$$u_{//} = -\varepsilon_s \zeta E_{//} / \mu , \qquad 4.16$$

where the zeta potential ζ is the potential difference across the EDL and E is the electric field. The subscript // denotes the vector component tangent to the

solid/liquid interface.

4.3 On the Existence of MHD Potential in Some Special Cases

Many microfluidic systems are planar (i.e., parallel to the *x*-*y* plane, Fig. 1). Since the conduits' depths (W in the $z-$direction) are relatively small, the magnetic field is nearly uniform and parallel to the $z-$direction, i.e., $\mathbf{b}=|\mathbf{b}|\mathbf{e}_z$, where $\mathbf{e}_z$ is a unit vector in the $z-$direction. Often, the electrodes and embedded features, such as pillars, are parallel to the $z-$axis and extend the entire conduit's depth. See Fig. 1 for an example. Under these conditions, the current flux and the Lorentz force can be expressed, respectively, with vectors $\mathbf{j}(x,y)=j_x(x,y)\mathbf{e}_x+j_y(x,y)\mathbf{e}_y$ and $\mathbf{f}_L(x,y)=|\mathbf{b}|\left(j_y(x,y)\mathbf{e}_x-j_x(x,y)\mathbf{e}_y\right)$ that are independent of the $z-$ coordinate. Although we used in the above Cartesian coordinates, the same holds true for any cylindrical coordinate system (Moon and Spencer 1988). Given that the electric current flux is solenoidal and $\mathbf{b}$ is constant, the Lorentz force $\mathbf{f}_L$ is irrotational (curl-free). To see this, consider

$$\nabla\times\mathbf{f}_L=\nabla\times(\mathbf{j}\times\mathbf{b})=\mathbf{j}(\nabla\cdot\mathbf{b})-\mathbf{b}(\nabla\cdot\mathbf{j})+(\mathbf{b}\cdot\nabla)\mathbf{j}-(\mathbf{j}\cdot\nabla)\mathbf{b}=0. \qquad 4.17$$

The first and last terms on the RHS of equation (4.17) vanish because $\mathbf{b}$ is a constant. The second term vanishes because the electric current flux is solenoidal ($\nabla\cdot\mathbf{j}=0$). The third term vanishes because, in our particular case, $\mathbf{b}$ and $\mathbf{j}$ are orthogonal and $\mathbf{j}$ doesn't vary in the direction of $\mathbf{b}$ (the z-direction). In other words, the Lorentz force is a conserving vector field, and one can define the "Lorentz

potential" Ξ such that

$$\mathbf{f}_L = -\nabla \Xi \,. \qquad 4.18$$

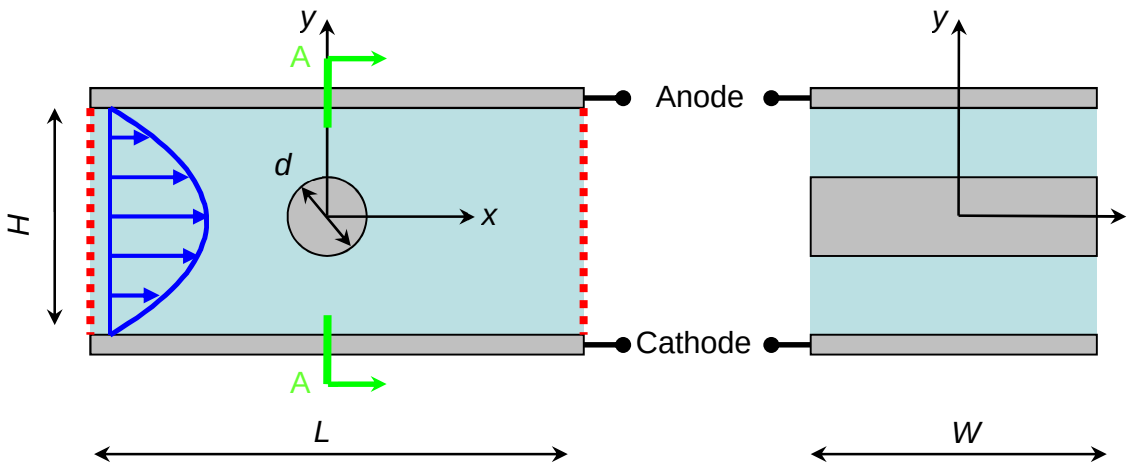

Figure 4.1 A schematic depiction of a segment of a flow conduit patterned with pillars. The image on the left is a top view and the image on the right is cross-section A-A. The red, dotted line denotes periodic boundary conditions

We emphasize that the Lorentz "potential" exists only in the special circumstances outlined above. Although these circumstances occur frequently in microfluidic systems, they *do not* apply to MHD flows in general. Unless the outlined special circumstances are satisfied, the Lorentz force is *not* curl-free.

Since in microfluidic systems the Reynolds number is typically small, one can neglect inertial effects in equation (4.12). In the absence of magnetophoretic and electrostatic forces, the dimensionless Stokes equation can be rewritten as

$$-\hat{\nabla}(\hat{p} + \hat{\Xi}) + \hat{\nabla}^2 \hat{\mathbf{u}} = 0 \qquad 4.19$$

so that the pressure can be modified to include the Lorentz "potential," $\hat{\Xi} = \dfrac{\Xi}{j_0 |\mathbf{b}|}$. On

account of the continuity equation, we also have

$$\hat{\nabla}^2(\hat{p}+\hat{\Xi})=0\,. \qquad 4.20$$

Hence, when the boundary conditions are equivalent, the MHD flow patterns are similar to pressure driven flow patterns.

In this section, we have shown that under special circumstances, which often occur in microfluidic systems, the MHD flow is equivalent to pressure-driven flow. Consequently, one can utilize the wealth of data available in the literature for pressure-driven flows to infer MHD flow patterns, as we demonstrate through a few examples in the following sections.

4.4 MHD Flow in a Conduit with a Uniform Cross-Section (MHD Pump)

Consider a straight conduit with rectangular cross-section of width W and height H (Fig. 1b without the pillar). The opposing walls of the conduit ($y=\pm\frac{H}{2}$) are plated with electrodes along the conduit's entire length L. An external potential difference ΔV_{ext} is imposed across the electrodes. It is well-known that the classical expression for fully-developed, pressure driven flow (White 2006) can be used to describe the velocity profile of low Hartman number, MHD flow in a conduit with a uniform, rectangular cross-section. Indeed, this is a special consequence of the derivation presented in section 3. The flow rate is (Bau et al. 2003):

$$Q=\frac{1}{R_H}\left(-\frac{dp}{dx}+j_y|\mathbf{b}|\right). \qquad 4.21$$

where $R_H = \frac{12\mu}{\chi W H^3}$ is the hydraulic resistance of the pump and $\chi = 1 - \frac{192H}{\pi^5 W}\sum_{n=0}^{\infty}\frac{1}{(1+2n)^5}\tanh\frac{(1+2n)\pi W}{2H}$. Witness that the sum in χ converges rapidly and, in many cases, just the first two terms in the series provide an adequate approximation. In the absence of an external pressure gradient, the average velocity is proportional to the $y-$ component of the current flux j_y. The stall pressure is $\Delta p_{stall} = |\mathbf{b}| I / W = |\mathbf{b}| j_y L$, where $I = j_y LW$ is the total current transmitted between the electrodes. Equation (4.21) can be rewritten in a slightly different form

$$Q = Q_{\max}\left(1 - \frac{\Delta p_b}{\Delta p_{stall}}\right). \qquad 4.22$$

In the above, $Q_{\max}$ is the flow rate in the absence of adverse (back) pressure and Δp_b is the back pressure.

4.4.1 Current-Potential Relationship in the MHD Pump

In contrast to the case of liquid metals, in the case of electrolyte solutions, the current density is not a linear function of the potential difference across the electrodes. Furthermore, as the potential difference across the electrodes increases, the current eventually reaches a limiting value.

To illustrate the complex current-potential dependence, we consider the reversible reaction $A^{z_1+} + (z_1 - z_2)e^- \Leftrightarrow B^{z_2+}$ of the RedOx species A^{z_1+}, B^{z_2+}, and C^{z_3-}. A specific example consists of the solution Fe^{3+}, Fe^{2+}, and Cl^- with the reducing reaction $Fe^{3+} + e^- \rightarrow Fe^{2+}$ at the cathode and the oxidizing reaction $Fe^{3+} \rightarrow Fe^{2+} + e^-$ at the anode. The steady state, dimensionless equations (4.1) and

(4.2) reduce to:

$$\begin{aligned}
&\frac{d\hat{c}_1}{d\hat{y}} + z_1\hat{c}_1\frac{d\hat{\phi}}{d\hat{y}} = -\frac{\hat{j}_{\hat{y}}}{z_1 - z_2} \\
&\frac{d\hat{c}_2}{d\hat{y}} + z_2\hat{c}_2\frac{d\hat{\phi}}{d\hat{y}} = \frac{D_1}{D_2}\cdot\frac{\hat{j}_{\hat{y}}}{z_1 - z_2} \\
&\frac{d\hat{c}_3}{d\hat{y}} - z_3\hat{c}_3\frac{d\hat{\phi}}{d\hat{y}} = 0
\end{aligned} \qquad 4.23$$

In the above, the concentrations are normalized with $\overline{c}_3$ and the current's density with $D_1 F\overline{c}_3 / H$. In general, equations like (4.23) must be solved numerically. Here, we consider a special case which allows us to obtain a relatively simple expression for the current-potential relationship.

Let $\overline{c}_1 = g\overline{c}_3$. When $z_1 = 3,\ z_2 = 2$, and $z_3 = 1$ (as in the case of ferri/ferro-chloride), and $D_1 / D_2 = 3/4$, one obtains (Grigin 1993) $\left(\hat{c}_1 + \hat{c}_2\right)\left(3\hat{c}_1 + 2\hat{c}_2\right) = m$, where m is an integration constant. Using mass conservation, one can determine m as a function of $\hat{j}_{\hat{y}}$ for any g. In the absence of current ($\hat{j}_{\hat{y}} = 0$), $m = (1-g)/2$. It turns out that m is nearly independent of $\hat{j}_{\hat{y}}$. Using the Butler-Volmer boundary conditions (15), we obtain an implicit relation between the current and the electrodes' potential difference (Qin and Bau, 2009) (Fig. 2). The hollow circles, crosses, and solid line correspond, respectively, to the exact solution (which does not assume fixed m), an analytic solution that assumes $m \sim (1-g)/2$, and a finite element solution of the NP equations. Witness that as the potential difference between the electrodes increases, the current flux initially increases slowly, then nearly linearly, and, eventually, it saturates at higher values of the potential difference. When $D_1 = 10^{-9} m^2 / s$, $\overline{c}_3 = 1M$ and $H = 1mm$, the

maximum (limiting) current is $j_{y,\lim} = 45.3 A/m^2$ (Fig. 2). For a conduit with width $W = 1mm$, flow viscosity $\mu = 10^{-3} Pa \cdot s$, and magnetic field $|\mathbf{b}| = 0.4T$, the predicted average MHD velocity is ~0.6 mm/s.

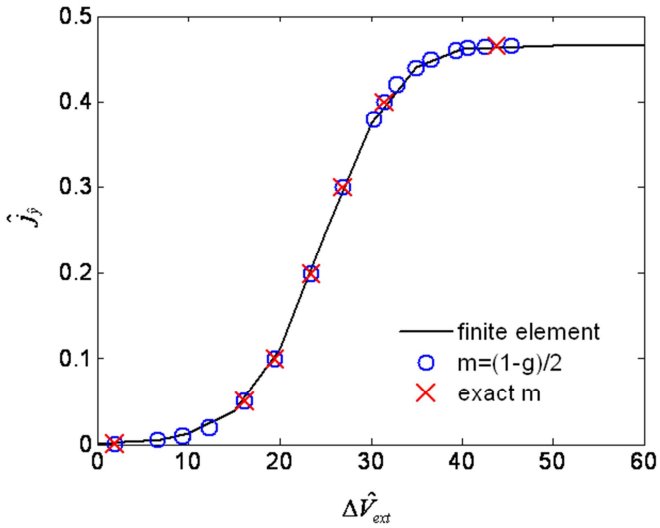

Figure 4.2 The dimensionless current flux as a function of the dimensionless electrodes' potential difference calculated by solving the full NP equations with finite elements (solid line), using the approximation $m \sim (1-g)/2$ (hollow circles), and using exact m values (crosses). $\alpha = 0.5$. $g = 0.2$. $\hat{j}_e = 10^{-3}$. The dimensionless, limiting current $\hat{j}_{\hat{y},\lim} = 0.47$. $D_2 / D_1 = 4/3$. $D_1 = D_3$

One take-away message is that, generally, in electrolyte solutions, the current is a nonlinear function of the potential difference across the electrodes. A linear relationship between the current and the potential difference can be assumed only for a limited range of operating conditions. The second observation is the existence of a limiting current. In other words, the amount of electric current that can be transmitted through the electrolyte solution does not increase monotonically with increasing potential difference due to mass transfer limitations (diffusion limited reaction).

Although, in practice, further increases in the potential difference across the electrodes may increase the current flux, this increase will typically be due to other (usually undesirable) electrochemical interactions at the electrode surfaces such as the electrolysis of water. In a closed system, the electrolysis of water will cause the formation of a gas blanket along the electrodes' surfaces that will greatly reduce the amount of current transmitted in the solution.

4.4.2 The Average Velocity and Efficiency of the MHD Pump

Kabbani *et al.* (2007) and Ho (2007) investigated the flow rate and the average velocity in the MHD pump as functions of the conduit's dimensions when the current injection is controlled. Since, in most applications, one controls the electrodes' potentials rather than the current, we briefly comment here on the situation when the potential difference between the electrodes is controlled. The current flux j_y is inversely proportional to the distance between the electrodes H. The flow rate in the absence of external back pressure: $Q = \frac{|\mathbf{b}| D_1 F \overline{c}_3 \hat{j}_{\hat{y}}}{12\mu} \chi H^2 W$ and the fluid's average velocity is

$$\overline{u} = \frac{|\mathbf{b}| D_1 F \overline{c}_3 \hat{j}_{\hat{y}}}{12\mu} \chi H \, . \qquad 4.24$$

The above expression is valid when the entire conduit's length is decorated with active electrodes.

Fig. 4.3 depicts the average flow velocity as a function of the conduit's height and width when $|\mathbf{b}| = 0.4T$, $D_1 = D_3 = 10^{-9} m^2 / s$, $\overline{c}_1 = \overline{c}_2 = 0.2M$, $\overline{c}_3 = 1M$,

$\Delta\hat{V}_{ext} = 32$, $\hat{j}_{\hat{y}} = 0.42$, and $\mu = 10^{-3} Pa \cdot s$. We assume that W is sufficiently small compared to the size of the source of the magnetic field so that the magnetic field is nearly uniform inside the conduit.

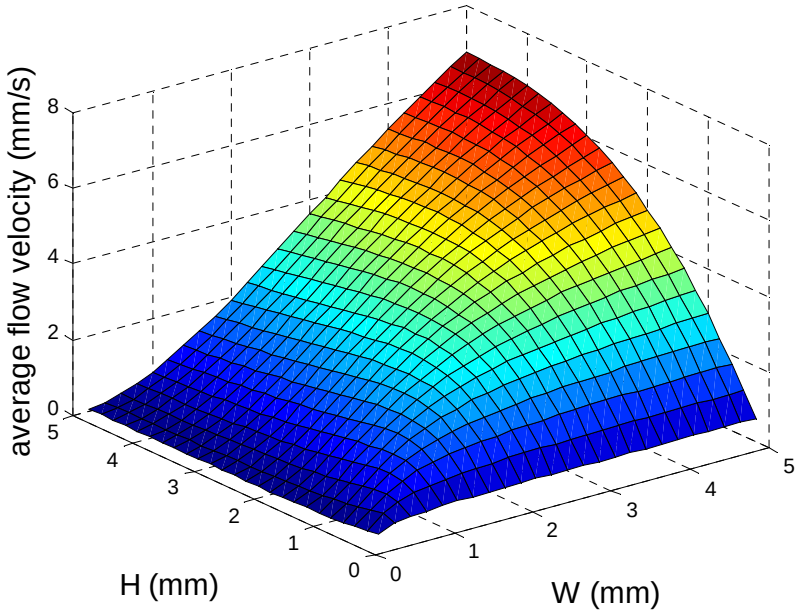

Figure 4.3 The average velocity of MHD flow as a function of the conduit height H and width W (equation 4.24). $|\mathbf{b}| = 0.4T$, $D_1 = 10^{-9} m^2/s$, $\bar{c}_3 = 1M$, $\hat{j}_{\hat{y}} = 0.42$, and $\mu = 10^{-3} Pa \cdot s$

At a fixed conduit width, as the height H increases, $\bar{u}$ first increases, attains a maximum at $H \sim W$, and then decreases. This behavior results from the drag force attaining a minimum in a square ($H = W$) cross-section while the total Lorentz driving force is nearly independent of the conduit's height. The latter is true because the current's density is inversely proportional to the distance between the electrodes ($j_y \propto 1/H$) and the Lorentz force is the product of the magnetic field, the current's

density and the fluid's volume. Thus, the total force is independent of the distance between the electrodes.

In the limit of $H >> W$, we approach the case of flow between two, infinite parallel plates, and the resistance imposed by the top ($y = H/2$) and bottom ($y = -H/2$) walls (the electrodes) can be neglected. Under this circumstance, along most of the conduit's cross-section, the velocity profile is parabolic in the *z*-direction and independent of *y*. The drag force is proportional to H/W and the Lorentz force is proportional to W. Thus, the average velocity is proportional to W^2/H. Witness the parabolic increase in the average velocity with W and the inverse proportionality to H in Fig. 4.3 when H is large and W is small. As W increases, the drag induced by the surfaces $y = \pm H/2$ starts to play a role and the rate of increase of the average velocity with W declines. When W is large, the average velocity is independent of W.

The MHD–induced velocities are relatively small. More appreciable velocities can be attained with higher conductivity electrolytes. For example, in the case of the RedOx pair $FeCl_3/FeCl_2$ ($D_1 = 6.04\times10^{-10} m^2/s$, $D_2 = 7.19\times10^{-10} m^2/s$, $D_3 = 2.03\times10^{-9} m^2/s$, and exchange current density $j_e = 10^{-6} A/m^2$, Qian and Bau, 2005) at maximum solute concentrations $c_1 = 1.54M, c_2 = 2.05M$, and $c_3 = 8.73M$, the limiting current density $j = 208.1A/m^2$ and the average flow velocity $\bar{u} = 2.9mm/s$ when $W = H = 1mm$ and $|\mathbf{b}| = 0.4T$.

We define the MHD pump's efficiency as the power needed to drive the flow, which includes the power needed to overcome the drag and the power invested to

overcome the adverse (back) pressure, normalized with the electrical power consumed.

$$eff = \frac{\Delta p_{stall} Q}{\Delta V_{ext} I}. \qquad 4.25$$

Our definition of the efficiency differs from that of Laser and Santiago (2004) and Ramos (2007), who treated the power needed to overcome the drag as internal pump loss and did not include it in the numerator of equation (4.25). Given that the entire length of conduits in microfludic devices may be equipped with electrodes and backpressure may be absent, it is appropriate to count the work carried out against the drag as part of the pump's output. In view of equation (4.22), the maximum efficiency is attained in the absence of backpressure ($\Delta p_b = 0$), i.e., $eff = \frac{\Delta p_{stall} Q_{\max}}{\Delta V_{ext} I}$. This efficiency is four times larger than the value reported in Laser and Santiago (2004) (Fig. 4.4).

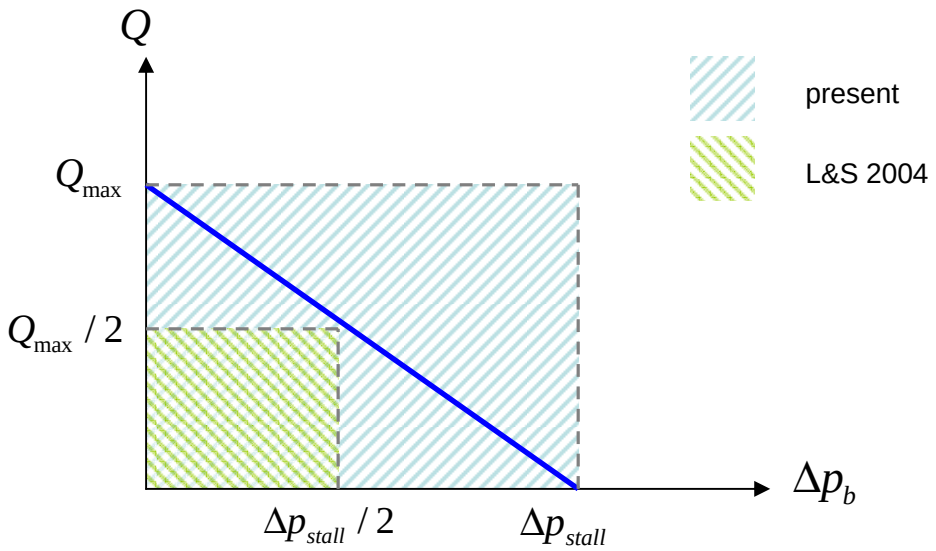

Figure 4.4 The pumping efficiency as defined in the present work and as defined in Laser and Santiago, 2004.

Upon substituting the expressions for the flow rate and the pressure drop, we can rewrite the efficiency (in the absence of backpressure) as:

$$eff = \frac{|\mathbf{b}|^2 D_1 F^2 \overline{c}_3}{12\mu RT} \cdot \frac{\hat{j}_{\hat{y}}}{\Delta \hat{V}_{ext}} \cdot \chi H^2 . \qquad 4.26$$

Equation (4.26) suggests that for a given conduit geometry, the efficiency depends on the ratio $\hat{j}_{\hat{y}} / \Delta \hat{V}_{ext}$. Fig. 4.5 depicts the ratio $\hat{j}_{\hat{y}} / \Delta \hat{V}_{ext}$ as a function of $\Delta \hat{V}_{ext}$. Witness that this ratio attains its maximum when $\Delta \hat{V}_{ext} = 32$ and $\hat{j}_{\hat{y}} = 0.42$.

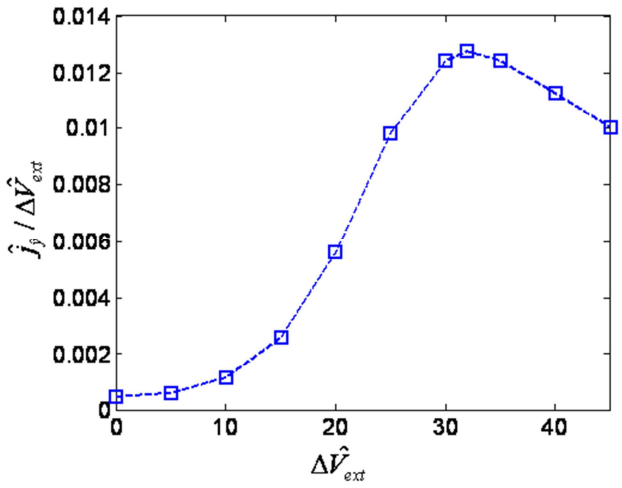

Figure 4.5 The ratio of $\hat{j}_{\hat{y}} / \Delta \hat{V}_{ext}$ as a function of $\Delta \hat{V}_{ext}$. The conditions are the same as in Fig. 4.2

Fig. 4.6 depicts the maximum efficiency as a function of the conduit's height and width when $|\mathbf{b}| = 0.4T$, $D_1 = D_3 = 10^{-9} m^2 / s$, $D_2 = 4/3 \times 10^{-9} m^2 / s$, $\overline{c}_1 = \overline{c}_2 = 0.2M$, $\overline{c}_3 = 1M$, $\Delta \hat{V}_{ext} = 32$, $\hat{j}_{\hat{y}} = 0.42$, and $\mu = 10^{-3} Pa \cdot s$.

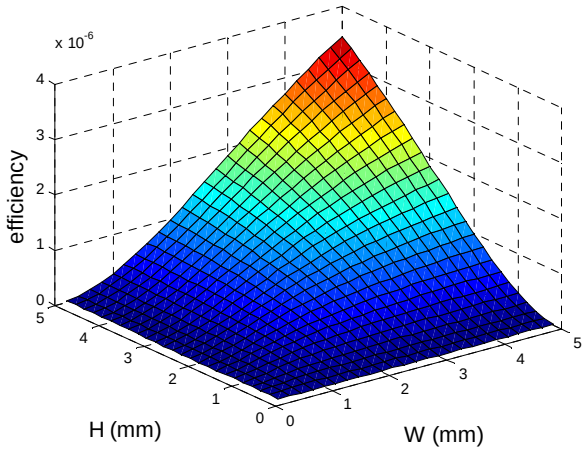

Figure 4.6 The maximum MHD pumping efficiency (equation 4.26) as a function of the conduit's height H and width W. $\Delta\hat{V}_{ext} = 32$ and all the other parameters are the same as in Fig. 4.3

Fig. 4.6 suggests that MHD pumps operating with electrolyte solutions have extremely low efficiency. The efficiency of the pump can be somewhat increased by using higher electrolyte molar concentrations to increase the electric conductivity of the solution.

Almost all the energy dissipated in the MHD pump is converted into heat. Nevertheless, the temperature increase of the electrolyte solution is relatively small. This is because of the relatively small dimensions of the conduits encountered in microfluidics, which facilitate highly efficient heat interaction with the ambient.

To estimate the temperature increase that one may expect in MHD flow, we consider the particular example of a conduit with a $1mm \times 1mm$ cross-section embedded in a $2mm$ thick polycarbonate (pc) sheet. Fig. 4.7 depicts the cross-section of the conduit and the substrate in which the conduit is embedded. The heat transfer coefficient at the surface of the plastic is assumed to be $h \sim 5W/m^2 \cdot K$,

which is at the low end of heat transfer coefficients corresponding to natural convection in air. When the applied potential is $\Delta V_{ext} = 40RT/F$, the current's density is $j_y = 45.3A/m^2$, and the heat dissipation per unit volume is $46.5kW/m^3$, the maximum temperature in the conduit is $\sim 0.5K$ above the ambient temperature. The thermal properties used are: $\rho_{fluid} = 1000kg/m^3$, $C_{p,fluid} = 1.2kJ/kg \cdot K$, $k_{fluid} = 0.21W/m \cdot K$, $\rho_{pc} = 1300kg/m^3$, $C_{p,pc} = 4.18kJ/kg \cdot K$ and $k_{pc} = 0.6W/m \cdot K$

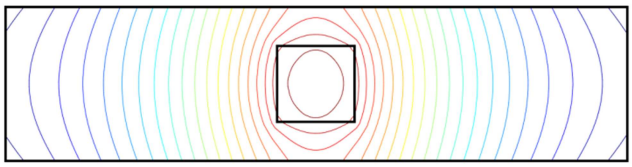

Figure 4.7 Temperature distribution (contours of constant temperature) in and around a MHD conduit embedded in a polycarbonate sheet. The chip size is $8mm \times 2mm$ and the conduit's cross-section is $1mm \times 1mm$

4.5 MHD Flow in a Conduit Patterned with a Pillar Array

In this section, we consider a uniform, long conduit patterned with a pillar array. Fig. 4.1 depicts one unit cell of depth W. The pillar diameter is d and the pillar's center is at the conduit's mid-width (Fig. 4.1a). We focus on a two-dimensional case ($W >> H, L$) in the absence of an external pressure gradient. We first consider the case when the current supplied to the unit cell is controlled (known) and one wishes to determine the flow pattern and the flow rate. To this end, we take advantage of results available in the literature for pressure-driven flows.

Integrating equation (4.19) over the volume of interest, we have, in the absence of external pressure differences:

$$\begin{aligned} \oiint \boldsymbol{\tau}_w d\mathbf{S} &= \mathbf{F}_{drag,cylinder} + \mathbf{F}_{drag,walls} \\ &= \iiint |\mathbf{b}| \, j_y(x,y)\mathbf{e}_x dV \\ &= |\mathbf{b}| \, IL \cdot \mathbf{e}_x \end{aligned} \qquad 4.27$$

where $\boldsymbol{\tau}_w$ is the stress tensor at the conduit's walls and the pillar's surface. The stress includes both pressure and viscous contributions. $\mathbf{S}$ is the surface enclosing the volume V. The drag coefficient $\lambda = \frac{F_{drag}}{\mu \bar{u} W}$. In the Stokes regime, the drag coefficients associated with both the cylinder and the conduit wall depend only on the geometry (Faxen 1946). Once the total current injection I is known, one can use the drag coefficient and the equivalency between pressure driven flow and MHD flow to compute the average velocity

$$\bar{u} = \frac{|\mathbf{b}| \, IL}{\mu(\lambda_{cylinder} + \lambda_{walls})W}. \qquad 4.28$$

The drag coefficient of a single circular pillar placed midway between two long, flat plates as a function of the ratio of the pillar's diameter and the distance between the plates is available in Harrison (1924), Faxen (1946) and Ben Richou *et al.* (2004). There's also a wealth of data for drag coefficients of pressure driven flow around pillar arrays. For example, Sangani and Acrivos (1982) provide drag coefficients of square and hexagonal pillar arrays.

For conciseness, we consider here in detail only a single row of uniformly spaced pillars confined between two parallel electrodes (Fig. 4.1). We carried out one

set of finite element simulations in which we specified the pressure drop across the length of the conduit, obtained the flow field, and determined the drag coefficient. In another set of simulations, we applied a potential difference across the electrode, specified the electrolyte's properties and solved the Nernst Planck equations with electro-neutrality (section 2) with finite elements to obtain the current distribution, the Lorentz body force, and the corresponding drag coefficients. In both cases, periodic velocity boundary conditions were specified at the flow inlet ($x = -L/2$) and exit ($x = L/2$). Fig. 4.8 depicts the drag coefficient associated with the pillar and the conduit's walls as functions of the pillar's diameter normalized with the conduit's width (H). The solid lines and symbols correspond, respectively, to the drag coefficients obtained with the pressure-driven flow simulations and the MHD simulations. The dashed line and hollow circles correspond to the pillar's drag coefficient, and the solid line and hollow squares correspond to the drag coefficient associated with the conduit's walls. The unit cell dimensions are $H = L = 1mm$. The electrolyte solution consisted of three ionic species with $D_i = (1, 4/3, 1) \times 10^{-9} m^2/s$, $\overline{c_i} = (0.2, 0.2, 1)M$, and $z_i = (3, 2, -1)$. In the Butler-Volmer equation, we specified $\alpha = 0.5$ and $j_e = 10^{-6} A/m^2$. Given the theory presented in section 4.3 on the equivalence between MHD flow and pressure-driven flow, it is not surprising that the drag coefficients associated with these two flows are identical.

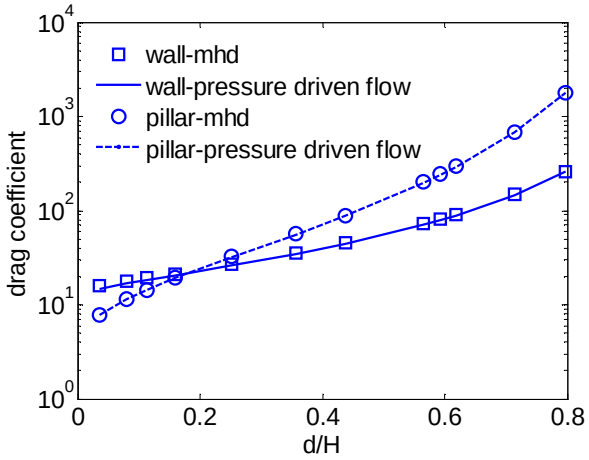

Figure 4.8 The drag coefficient at the pillar's surface (dashed line and hollow circles) and at the conduit's surface (solid line and hollow squares) as functions of the pillar's diameter normalized with the conduit's width (H). The lines and symbols correspond, respectively, to pressure-drive flow and the solution of the NP-NS model. For MHD flow, we used $|\mathbf{b}| = 0.4T$, $D_1 = D_3 = 10^{-9} m^2/s$, $D_2 = 4/3 \times 10^{-9} m^2/s$, $z_1 = 3, z_2 = 2, z_3 = -1$, $\bar{c}_1 = \bar{c}_2 = 0.2M$, $\bar{c}_3 = 1M$, $\Delta\hat{V}_{ext} = 25$, $\rho = 10^3 kg/m^3$, $\mu = 10^{-3} Pa \cdot s$, $H = W = 1mm$, $\alpha = 0.5$ and $j_e = 10^{-6} A/m^2$

When the total current is given, it is a simple matter to take advantage of the data available in the literature for pressure-driven flows to determine the MHD velocity profile and the flow rate. The same method can be applied to situations when the fluid is subjected to both Lorentz body force and pressure gradients (either assisting or adverse). Since the momentum equation is linear at low Reynolds numbers, one can simply superpose MHD and pressure-driven flows.

Matters get more complicated when the potential difference between the electrodes is the control input rather than the electric current. In this case, to obtain

the concentration distribution, one requires knowledge of the flow field and to obtain the flow field, one needs to know the current, which, in turn, depends on the concentration distribution. Since the various fields are coupled nonlinearly, one cannot take advantage of superposition. When the effects of advection on the concentration distribution cannot be neglected, the data available in the literature for pressure driven flow can only be used to verify the MHD computations.

Next, we consider a case when the electrode potential difference is controlled and the current is not apriori known. To obtain the current distribution, we solve the Nernst-Planck equations with Buttler-Volmer boundary conditions together with the Navier-Stokes equations (section 4.2). Fig. 4.9 depicts the total, dimensionless current in the unit cell as a function of d/H when the effects of advection on the concentration distribution are neglected (zero Peclet number, solid line) and when the effect of the flow on the concentration distribution (dashed line with hollow squares) is accounted for. Fig. 4.9a and 4.9b correspond, respectively, to a dimensionless potential difference between the electrodes of 25 and 40. Clearly advection significantly affects the current both quantitatively and qualitatively. When $d/H = 0.44$ and $\Delta\hat{V}_{ext} = 25$, neglecting advection leads to a current underestimate of ~25% (Fig. 9a). When $\Delta\hat{V}_{ext} = 40$, neglecting advection leads to up to a 45% underestimate in the current (Fig. 4.9b). As the potential difference across the electrodes $\Delta\hat{V}_{ext}$ increases, the magnitude of the velocity increases, advection effects become more important, and the error resulting from neglecting advection increases.

a) b)

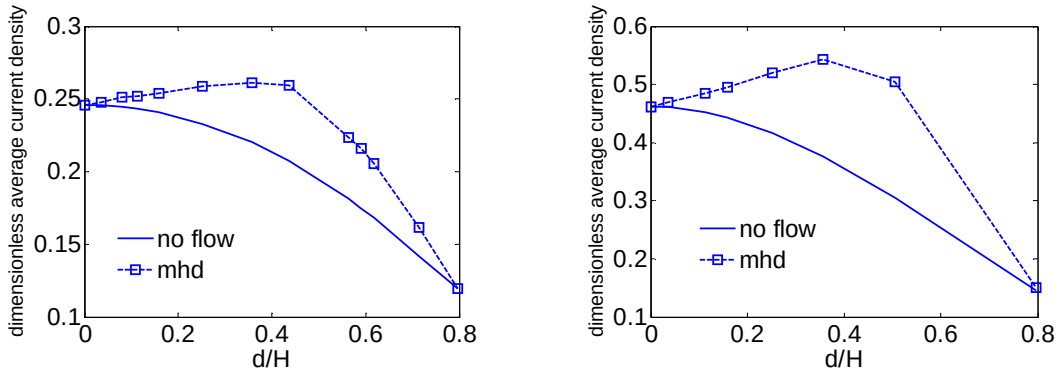

Figure 4.9 The average y-component of the dimensionless current flux as a function of d/H in the absence (solid line) and the presence (dashed line with hollow squares) of MHD flow. The potential difference between the electrodes is $\Delta\hat{V}_{ext} = 25$ (a) and 40 (b). All other conditions are the same as in Fig. 4.8

In the absence of advection (solid lines in Fig. 4.8), as the pillar diameter increases, the current decreases monotonically. This is intuitively expected. As the pillar diameter increases, the area available to current flow decreases and one would expect the current to decrease. Counter to intuition, however, when convection is accounted for (dashed lines in Fig. 8), as the pillar diameter increases from zero, the limiting current initially increases, attains a maximum, and then decreases.

A similar trend is evident in Fig. 4.10. The figure depicts the average dimensionless current flux in the *y*-direction as a function of the potential difference between the electrodes $\Delta\hat{V}_{ext}$ when $d/H = 0$, 0.036, 0.11, 0.16, 0.25, 0.36, 0.71 and 0.8. The electrolyte solution is the same as in Fig. 4.9. As the potential difference $\Delta\hat{V}_{ext}$ increases, the current initially increases slowly, then nearly linearly, and eventually reaches an asymptotic, limiting value $\hat{j}_{\hat{y},lim}$. Witness that the currents

associated with $0 < d/H < 0.36$ are higher than the one associated with $d/H = 0$.

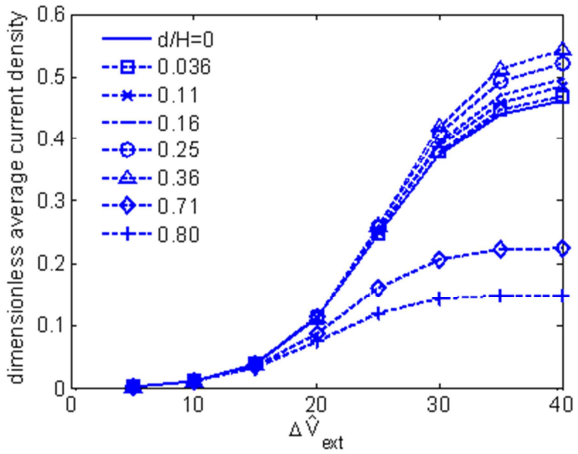

Figure 4.10 The average dimensionless current flux $\overline{\hat{j}}_{\hat{y}}$ as a function of the applied dimensionless potential difference $\Delta\hat{V}_{ext}$ when $d/H = 0$, 0.036, 0.11, 0.16, 0.25, 0.36, 0.71 and 0.8. All other conditions are the same as in Fig. 4.8

What then is the mechanism by which the pillar presence enhances the current flow in certain circumstances? One possible explanation is, that in the presence of the pillar, the magnitude of the velocity $u_x(0, y)$ in the region above and beneath the pillar ($d/2 < |y| < H/2$) increases above the corresponding value upstream of the pillar. This, in turn, increases the concentration gradients next to the electrodes' surfaces and enhances the diffusion's contribution to the current flow. Fig. 4.11a depicts the concentration field c_1 in the presence of the pillar and the MHD flow when $\Delta\hat{V}_{ext}$ =25 and $d/H = 0.2$. The solid longitudinal lines and the transverse solid lines represent, respectively, concentration contour lines and current flux lines. Fig. 4.11b depicts the concentration field c_1 in the presence of a pillar and in the absence of flow motion. Fig. 4.11c depicts the concentration field c_1 in the absence of the pillar. In the last case, the concentration field is independent of the flow. In

cases (b) and (c), the concentration field is symmetric with respect to the $y = 0$ axis while in Fig. 4.11a, due to transverse velocity components in the vicinity of the pillar, the concentration field is asymmetric with respect to the $y = 0$ axis. In other words, in the presence of the pillar, there is a transverse velocity component that contributes to electrolyte advection. To better demonstrate the effect of the pillar on the concentration distribution, Figs. 4.11d and 4.11e depict, respectively, $c_1(x, H/2)$ along the surface of the cathode as a function of x and $c_1(0, y)$ as a function of y in the presence of motion (solid lines), in an absence of the pillar (dotted line with hollow circles), and in the presence of the pillar and the absence of motion (dashed line). Witness that in the presence of the pillar and the flow, the concentration of c_1 next to the electrode's surface (in the vicinity of $x = 0$, solid line, Fig. 4.11d) is significantly higher than in the absence of a pillar (dotted line with hollow circles) or in the presence of a pillar without flow (dashed line). The latter case demonstrates clearly that, in the absence of flow, the presence of the pillar adversely affect the current flow. The average current is lower than in the absence of a pillar. In the presence of both a pillar and flow, the concentration next to the electrode's surface is higher than otherwise and, thus, the average current flux is higher. Similarly, Fig. 4.11e shows that the concentration gradient is highest in the presence of the pillar and MHD flow (solid line) and lowest in the presence of a pillar and an absence of flow (dashed line). In summary, on the one hand, the pillar reduces the cross-sectional area available to the current flow and increases the drag, both adversely affecting the flow rate. On the other hand, the pillar indirectly modifies that concentration field, which

enhances current flow. These two competing effects lead to an optimal pillar size that maximizes current flow.

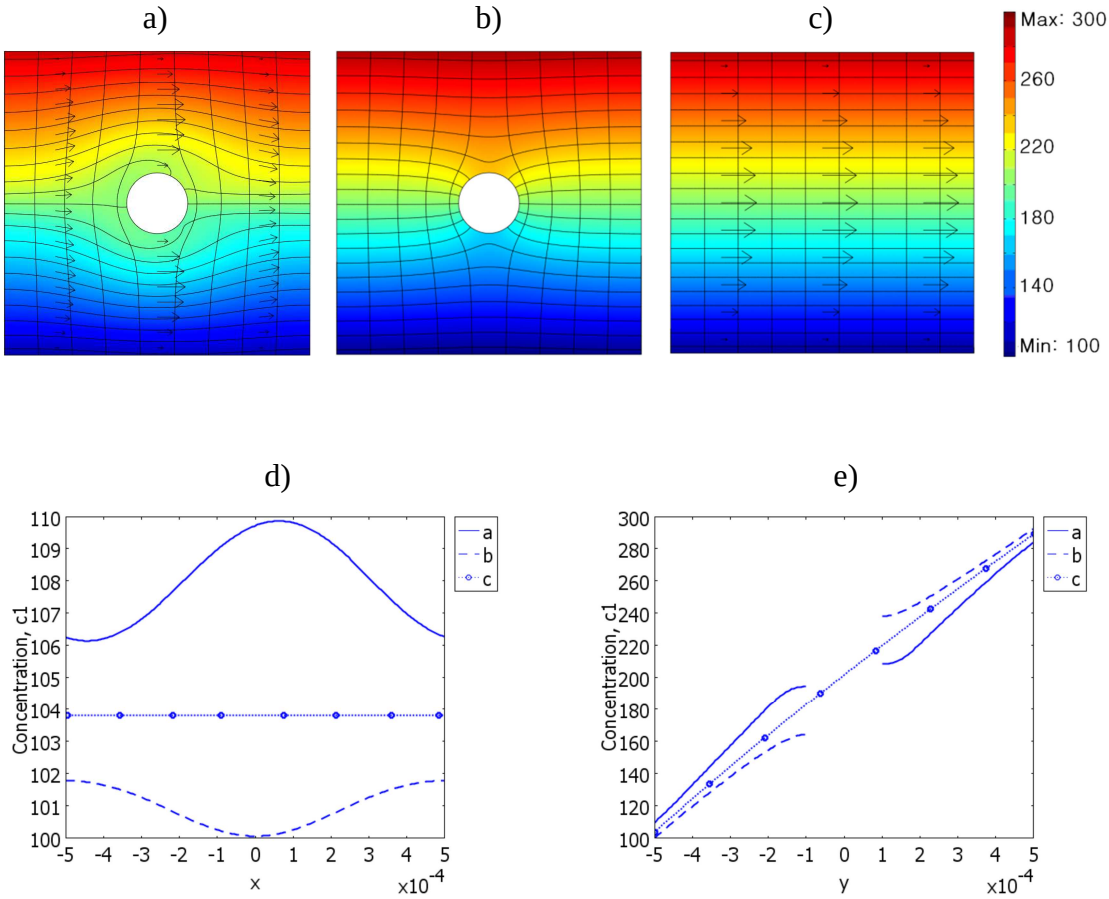

Figure 4.11 (a) The concentration field c_1 in the presence of a cylinder ($d/H = 0.2$) and MHD flow. (b) The concentration field for c_1 in the presence of a cylinder ($d/H = 0.2$) and in the absence of motion. (c) The concentration field c_1 in the absence of a cylinder. The color code and the solid longitudinal lines in (a), (b), and (c) correspond, respectively, to concentration and concentration contours. The transverse solid lines are the current fluxes. The arrows are velocity vectors. (d) The concentration distribution $c_1(x,-H/2)$ along the surface of the cathode as a function of x in the presence of motion (solid line), in the absence of the cylinder (dotted line with hollow circles), and in the presence of the cylinder and an absence of motion

(dashed line). (e) The concentration distribution $c_1(0, y)$ as a function of y in the presence of motion (solid line), in the absence of the cylinder (dotted line with hollow circles), and in the presence of the cylinder and an absence of motion (dashed line). $\Delta\hat{V}_{ext} = 25$. All other conditions are the same as in Fig. 4.8

The pillar could contribute to current flow in yet another way. The electric double layer surrounding the pillar is rich in ions, which is described macroscopically as surface conduction. The Bikerman-Dukhin number quantifies the ratio of the surface conductivity to the bulk conductivity (Bazant *et al.* 2006, Chu and Bazant 2006). Since MHD devices typically operate with moderate DC potential and thin electric double layers, the double layer remains near equilibrium and the Dukin number is much smaller than 1, leading to negligible surface conductance.

In the range of parameters considered here and consistent with equation (4.26), the flow rate is linearly proportional to the total current. Fig. 4.12 depicts the average flow velocities as functions of the current when $d/H = 0.11$, 0.16, 0.25, 0.36, 0.50 and 0.71. Fig. 4.13 depicts the average flow velocity as a function of the pillar size when the dimensionless potential difference between the electrodes is $\Delta\hat{V}_{ext} = 25$. Although the current attains its maximum value at $d/H = 0.4$, the flow rate decreases monotonically as d/H increases from zero. In other words, the presence of the pillar enhances the drag to a greater extent than the propulsive force (which is proportional to the current).

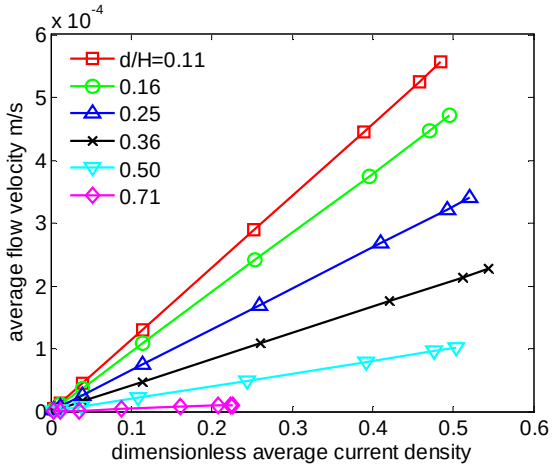

Figure 4.12 The average flow velocity $\bar{u}$ as a function of the average dimensionless current $\bar{\hat{j}}_{\hat{y}}$ when $d/H = 0.11$ (square), 0.16 (circle), 0.25 (upright triangle), 0.36 (cross), 0.50 (downward triangle) and 0.71 (diamond). All other conditions are the same as in Fig. 4.8

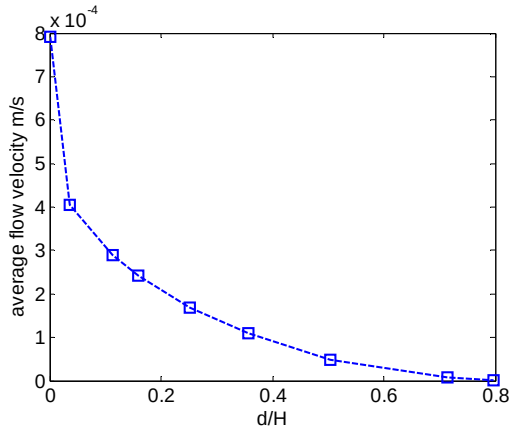

Figure 4.13 The average flow velocity $\bar{u}$ as a function of d/H at $\Delta\hat{V}_{ext} = 25$. All other conditions are the same as in Fig. 4.8. $d/H = 0$ denote the situation of flow in an empty straight channel.

4.6 Dispersion Associated with MHD Flow with Slip BC

Consider solvent laden with analytes driven through the column by MHD flow.

The analytes are assumed to be dilute, do not affect the solvent's properties, and do not interact among themselves. The chromatographic, longitudinal dispersion coefficient depends sensitively on the velocity profile. Since the velocity profile of MHD flow can be controlled by judicious patterning of the electrodes, one can seek electrode pattern that yield velocity profiles, which, in turn minimize the dispersion coefficient. The objective of this section is to demonstrate that the dispersion coefficient in a MHD chromatograph can be reduced by appropriate patterning of the electrodes.

Consider a uniform MHD conduit with a rectangular cross-section as depicted in Fig. 4.14. The conduit's width is W and its height is H. The electrodes are located along the channel walls that are parallel to the x axis. A uniform magnetic field is directed along $x-$ axis. The conduit is filled with a RedOx electrolyte solution that undergoes a reversible reaction at the electrodes' surfaces. A potential difference is applied between the top electrodes (located along the surface $y = H/2$) and the bottom electrodes (located along the surface $y = -H/2$). The current transmitted in the electrolyte solution interacts with the magnetic field to produce Lorentz body force that propels the fluid in the $z-$direction.

Suppose that the top and bottom surfaces are divided into N segments each. Here, we will carry out calculations for $N = 10$ and we assume that the arrangement is symmetric with respect to the axis $y = 0$. Each segment can be either an active electrode or an insulating surface. To ensure fluid motion, we fix the four segments next to the corners to be active electrodes. We number the other segments

away from the corners $i = 1, 2, 3$ and 4. See Fig. 4.14. We wish to find which segments should be active so that the dispersion coefficient is minimized. In other words, we consider an optimization space consisting of the variables E_i, where $E_i = 1$ indicates that segment i is active and $E_i = 0$ indicates that segment i is insulated.

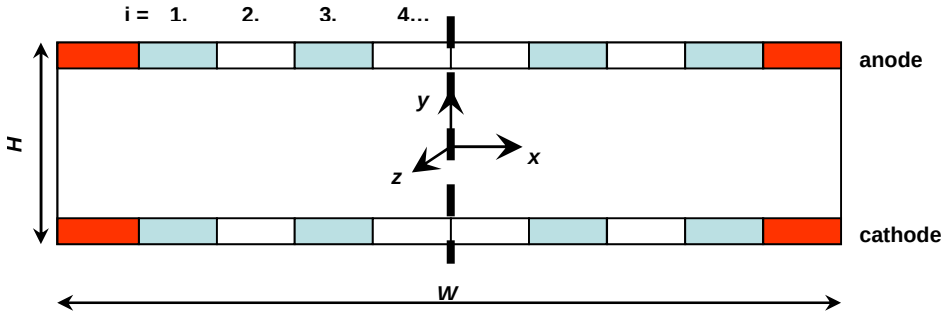

Figure 4.14 Cross-section of MHD flow channel. Top and bottom channel walls are partially coated with electrodes.

Note that the conduit cross-section is uniform, the velocity vector only has component in the $z-$ direction and does not affect the concentration field (fully developed flow). Thus, we can solve the two dimensional electrochemical current injection problem independently of the flow field. Also note that at small Reynolds numbers and in the absence of an external applied pressure gradient, equation (4.6) reduces to $\mu\nabla^2 w + j_y b_x = 0$, which allows us to determine the flow velocity $w(x, y)$ in the z-direction once the current density flux has been calculated. We assume uniform magnetic field with known intensity.

Recently, Yan et al. 2010 developed a model that allows one to estimate the longitudinal dispersion coefficient in a periodic medium. The model can be applied to the open column chromatograph as a special case. To estimate the dispersion

coefficient, one needs to compute the closure variable f by solving the closure equations:

$$w\frac{\partial f}{\partial z} - D_{\mathrm{m}}\nabla^2 f = -\left(w - \frac{\langle w\rangle^{\mathrm{m}}}{1+k''} \right), \qquad 4.29$$

$$D_{\mathrm{m}}\frac{\partial f}{\partial n} = \left(-D_{\mathrm{m}} + \gamma\delta\frac{\langle w\rangle^{\mathrm{m}}}{1+k''} \right), \qquad 4.30$$

$$\int_{V_{\mathrm{m}}} f dV + \gamma\delta \int_{A_{\mathrm{ms}}} f dA = 0, \qquad 4.31$$

For detail derivation of the model, see Yan et al. 2010.

Once the function $f(x,y)$ is known, the dispersion tensor could be calculated using the expression:

$$D = D_{\mathrm{m}}\left[1 + \frac{1}{V_{\mathrm{m}}}\int_{A_{\mathrm{ms}}} f dA \right] - \langle w' f\rangle^{\mathrm{m}} + \frac{\gamma\delta}{V_{\mathrm{m}}}\langle w\rangle^{\mathrm{m}}\int_{A_{\mathrm{ms}}} f dA + \frac{(k'')^2}{(1+k'')^2}\frac{V_{\mathrm{m}}}{k\gamma A_{\mathrm{ms}}}\langle w\rangle^{\mathrm{m}}\langle w\rangle^{\mathrm{m}} \qquad 4.32$$

In the above, w denote the velocity field; $k'' = \frac{\gamma V_{\mathrm{s}}}{V_{\mathrm{m}}}$ is the retention factor; D_{m} is the molecular diffusivity; δ is the thickness of the stationary phase; γ is the partition coefficient at the interface. Subscripts m and s denote, respectively, the mobile and stationary phases. The bracket pair $<\ >$ denotes volume average. $w' = w - \langle w\rangle^{\mathrm{m}}$.

We carried out numerical simulations for the problem specified above and tabulated the longitudal dispersion coefficient D in Table 1. The 5$^{\mathrm{th}}$ configuration (with $E_2 = 1$ and $E_{1,3,4} = 0$) provides the smallest longitudinal dispersion coefficient. The 5$^{\mathrm{th}}$ configuration provides a dispersion coefficient which is about 40% of the dispersion coefficient in the case when the entire conduit surfaces are covered with electrodes (the normal case). Fig. 4.15 shows the concentration field (grey scale for

distribution of c_1), the velocity field (blue lines for the contour lines) and the current fluxes (red lines) associated with the optimal setting.

E_i	$i=1$	2	3	4	D/D_m
1	0	0	0	0	376.46
2	0	0	0	1	307.02
3	0	0	1	0	167.92
4	0	0	1	1	394.74
5	0	1	0	0	**90.39**
6	0	1	0	1	236.93
7	0	1	1	0	162.61
8	0	1	1	1	309.44
9	1	0	0	0	219.72
10	1	0	0	1	147.99
11	1	0	1	0	101.63
12	1	0	1	1	233.60
13	1	1	0	0	101.17
14	1	1	0	1	157.95
15	1	1	1	0	118.07
16	1	1	1	1	218.72

Table 4.1 16 possibilities of electrode arrangements for the cross-section depicted in Fig. 4.14 and the corresponding dispersion coefficients. ‘1’ and ‘0’ denote, respectively, the electrode to be ‘active’ and ‘passive.’

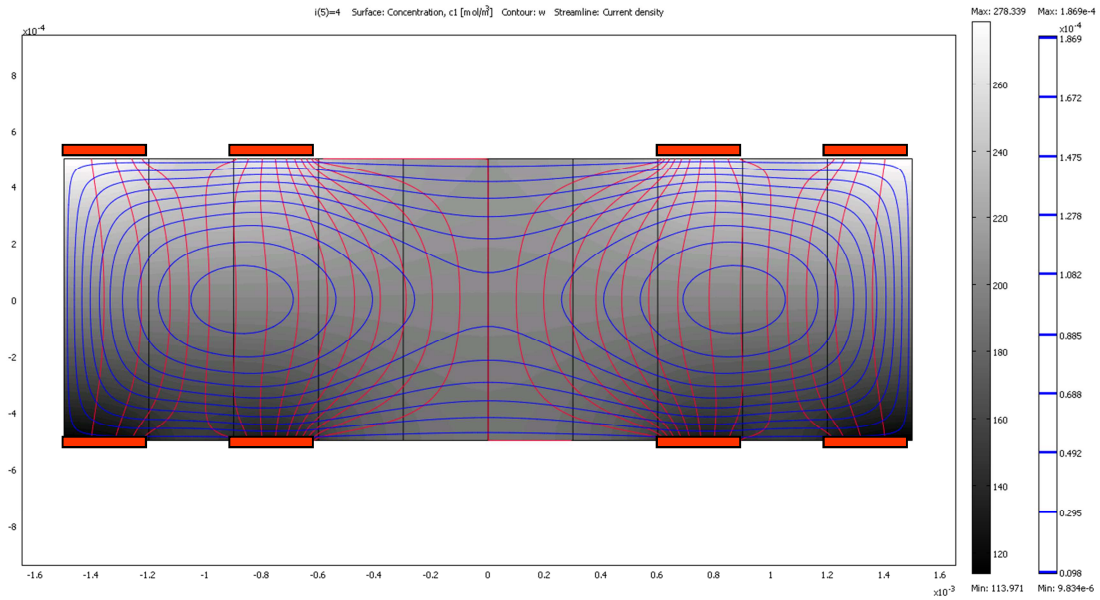

Figure 4.15 Concentration field and velocity field when $E_2 = 1$ and $E_{1,3,4} = 0$. The grayscale surface plot shows distribution of species c_1. The blue lines are the velocity contour lines. The red lines are the current fluxes. The red blocks symbolize the locations of active electrodes.

4.7 Conclusions

We describe the mathematical model for MHD flows of electrolyte solutions in microfluidic systems. In general, the model requires the concurrent solution of the Nernst-Planck equations and the momentum equations. The flow field modifies the concentration field and the concentration field affects the electric current, which, in turn, affects the body force in the momentum equation. MHD has the advantage of providing a convenient means to pump and stir fluids and control fluid flow with electrical signals and without a need for moving mechanical components. Flow can be directed along any desired path in a microfluidic network without a need for any valves. The disadvantage of MHD is that it involves a volumetric force that does not

scale favorably as the conduit size decreases. MHD pumps operating with electrolyte solutions also have very low conversion efficiency, as only a very small fraction of the electric power is converted into work. More serious shortcomings include the need to operate with electrolyte solutions that undergo reversible reactions to avoid bubble formation and undesirable electrochemical electrode reactions and the limitation on the maximum amount of current that can be transmitted in the solutions. It seems that MHD are most likely to benefit applications in which conduit sizes range from hundreds of micrometers to millimeters – a range of length scales in which the MHD drive provides significantly higher flow rates than electroosmosis.

We have shown that when the Reynolds number is low, the magnetic field is uniform, and the electric field is orthogonal to the magnetic field, the Lorentz body force is irrotational and one can define a “Lorentz” potential. In other words, the MHD flow is equivalent to pressure-driven flow, and one can use data available in the literature for pressure-driven flow to deduce the MHD flow patterns. The above conditions often prevail in microfluidic systems. We utilized this equivalence in two examples. The first example consisted of a uniform conduit. Here, the equivalence between MHD flow and pressure-driven flow has been known for many years. The second example consisted of a conduit patterned with pillars. This is a somewhat more general case as the electric flux is neither unidirectional nor uniform as in the first example. The equivalence between MHD flow and pressure-driven flow allows us to utilize drag coefficients available in the literature for pressure-driven flow to calculate the MHD flow patterns provided that the total electric current is controlled.

The use of the MHD – pressure driven flow equivalence requires caution, however, since the emergence of secondary flows such as may evolve when the fluid goes around a bend (Yi and Bau 2003) or a curve will destroy the analogy between MHD and pressure-driven flows.

When the electric potential difference across the electrodes is the control variable, the equivalence between the pressure-driven and MHD flow cannot be utilized directly and one needs to compute the concentration, current, and flow fields simultaneously by solving the coupled Nernst-Planck and Navier-Stokes equations.

We also computed the electric current, concentration, and flow field in a conduit and demonstrated that an optimal pillar diameter exists that maximizes the current flow. It is plausible that even higher current transmission can be obtained by optimizing the shape of the pillar. However, maximum flow rate still happens in the absence of pillars.

Finally, we showed that the dispersion coefficient associated with MHD flow in a rectangular channel could be minimized through designing the electrode settings, and thus modifies the flow field.

CHAPTER 5: Magneto-Hydrodynamic Flow of Binary Electrolyte in a Concentric Annulus

5.1 Introduction

Magneto-hydrodynamic (MHD) driven flow is of interest in many applications since one can induce fluid motion without a need for mechanical pumps and the flow velocity can be readily controlled by adjusting the current or the potential applied to electrodes (Qian & Bau 2009). Here, we consider MHD flow of a binary electrolyte confined in a conduit bent into a donut with an inner radius R_1 and an outer radius R_2. We use the cylindrical coordinate system (R, Θ, Z), where R, Θ, and Z are, respectively, the radial, azimuthal, and axial coordinates. The inner $(R = R_1)$ and outer $(R = R_2)$ surfaces of the annulus double-up as electrodes. The electrolyte is subjected to a uniform magnetic field directed parallel to the annulus axis (Z). When a potential difference is applied across the electrodes, radial current flows in the solution. The current interacts with the axial magnetic field to produce an azimuthal Lorentz body force, which, in turn induces azimuthal flow.

When the cylindrical annulus is infinitely long, purely azimuthal flow, analogous to the celebrated Dean's pressure-driven flow (Dean, 1928 and Ito, 1951), is possible. The flow stability can be characterized with the Dean number $\mathrm{Dn} = \mathrm{Re}\sqrt{d/R_1}$. Here $\mathrm{Re} = |\bar{V}|d/\nu$ is the Reynolds number; $\bar{V}$ is the average azimuthal velocity; ν is the kinematic viscosity; and $d = R_2 - R_1$ is the width of the gap between the two cylinders. When the Dean number is smaller than a critical value, the azimuthal flow is stable. When the Dean number exceeds its critical value, due to centrifugal

acceleration, the purely azimuthal flow loses stability and gives rise to convective rolls in the transverse $R-Z$ plane (Chandrasekhar, 1961, and Drazin and Reid, 2010). As the Dean number increases above a critical value so does the complexity of the flow (Winters et al., 1987). When the height of the annulus is finite, purely azimuthal flows are not possible and transverse circulation exists for all Dean numbers.

Various researchers studied pressure-driven flows in curved tubes with different cross-sections such as circular (i.e., Bara et al., 1992, and Berger & Talbot, 1983, Soh 1988, Bara et al. 1992, Bovendeerd et al. 1987, Boutabaa et al., 2009, Cheng et al. 1976, and Verkaik et al., 2009), elliptical (Cuming, 1955, and Silva et al., 1999), square (Soh 1988, Boutabaa et al., 2009, and Humphrey et al., 1977), and rectangular (Silva et al. 1999, Targett et al. 1995, De Vriend 1931, and Yanase et al. 2002). Since the annular geometry has applications in heat exchangers, the associated convective heat transfer has been studied by Avramenko et al. (2003), Cheng & Akiyama (1970), Gyves & Irvine (2000), and Mondal et al. (2008). Witness that pressure-driven flow in a perfectly closed loop is impractical. By necessity, the closed loop approximates a spiral geometry (Targett et al., 1995).

In contrast, MHD flow provides a practical means of propelling fluids in a closed loop (Zhong et al., 2002, and Eijkel et al., 2003). Velikhov (1959), Khalzov (2008), Hunt & Williams (1968), Hunt & Malcolm (1968), Hunt & Stewartson (1969), Baylis (1964 & 1971), and Kobayashi (1977) studied the stability of annular MHD flow of liquid metals and found that the magnetic field provides a stabilizing effect and

suppresses the evolution of secondary flows.

Hence to forth, the problem of MHD flow of electrolyte solutions in a concentric annulus and its stability has not been addressed. The case of electrolyte solutions is significantly different than that of liquid metals as the flow patterns affect the concentration field, which, in turn, affects the local electric conductivity (Qin & Bau, 2010). These types of problems are of interest among other things, in electroplating, where it is desirable to maintain unidirectional (azimuthal) flow to assure plating uniformity and avoid secondary flows that may cause non-uniform material deposition (Marshalls & Mocskos, 1999) and in liquid gyroscopes for navigation systems (Laughlin 2007).

More generally, in recent years, there has been growing interest in studying the interplay between hydrodynamic stability and electrochemistry. For example, Volgin and Davydov (2006) review the literature pertaining to the electrochemical Rayleigh-Benard problem. In this chapter, we study for the first time, the MHD motion of a binary electrolyte in an annulus and its stability characteristics. This chapter is organized as follows. Section 5.2 introduces the mathematical model. Section 5.3 derives a closed-form solution for the current flux and concentration and velocity fields in an infinitely long annulus. Section 5.4 examines the linear stability of the azimuthal flow derived in section 5.3 and delineates why electrochemical effects have a destabilizing effect when the current is directed outwardly and a stabilizing effect when the current is directed inwardly. Section 5.5 describes the MHD flow in a finite-height annular conduit. Section 5.6 concludes.

5.2 Mathematical Model

Consider a binary electrolyte $M_x^{z_1}A_y^{z_2}$ confined between two concentric cylinders of radii R_1 and R_2 $(R_2 > R_1)$. M^{z_1} is the metal ion and A^{z_2} is the anion. $d = R_2 - R_1$ is the gap between the cylinders. We consider both cases when the annulus is infinitely long and when it has a finite length L. The cylinders' surfaces in contact with the liquid are coated with metal M (same material as the cations) and serve as electrodes. We use the cylindrical coordinate system (R, Θ, Z) with its origin at the cylinders' center. The symbols $\mathbf{e}_R$, $\mathbf{e}_\Theta$, and $\mathbf{e}_Z$ denote, respectively unit vectors in the radial (R), azimuthal (Θ), and axial (Z) directions (**Fig. 5.1**). The electrolyte is subjected to a uniform magnetic field $\mathbf{B} = -B\mathbf{e}_Z$**.** When a potential difference is imposed between the electrodes' pair, electric current flux **J** is transmitted in the solution. The electric current interacts with the magnetic field to produce a Lorentz body force, which in turn, induces fluid motion. The electrolyte undergoes the backward reaction of $M^{z_1} + z_1 e^- \leftrightarrow M(s)$ at the anode and the forward reaction at the cathode. We consider sufficiently short times so that the geometry of the electrodes does not change appreciably during the process.

The ions' concentrations satisfy the Nernst-Planck equation (Newman, 2004)

$$\frac{\partial C_i}{\partial T^*} = -\nabla \cdot \mathbf{H}_i, \qquad (i = 1, 2), \tag{5.1}$$

where C_1 and C_2 are, respectively, the concentrations of M^{z_1} and A^{z_2}; T^* is time;

$$\mathbf{H}_i = \mathbf{U}C_i - D_i^*\nabla C_i - z_i v_i F C_i(\nabla\Phi - \mathbf{U} \times \mathbf{B}) \tag{5.2}$$

is the ionic flux of species i; $\mathbf{U} = U\mathbf{e}_R + V\mathbf{e}_\Theta + W\mathbf{e}_Z$ is the velocity vector; D_i^*, z_i, and $v_i = D_i^*/(R_u T)$ are, respectively, the diffusion coefficient, valence, and mobility

of species i. F is the Faraday constant; T is the absolute temperature; R_u is the ideal gas constant; and Φ is the electric potential. We adopt here the convention that regular fonts represent scalar quantities while bold letters represent vectors.

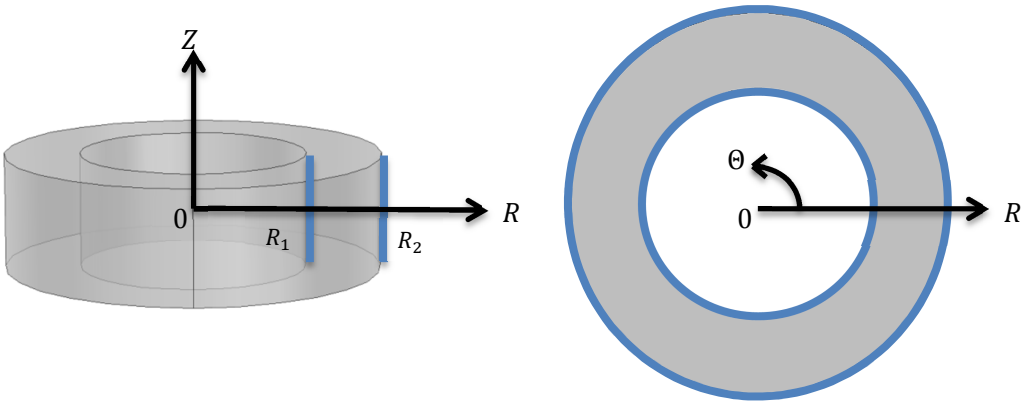

Figure 5.1 A schematic depiction of the flow cell and the cylindrical coordinate system (R, Θ, Z). The electrolyte is confined in a concentric annulus with an inner radius R_1 and an outer radius R_2. The electrodes coincide with the cylindrical surfaces.

With the exception of very thin electric double layers next to the electrodes and other solid surfaces, the electro-neutrality condition requires that

$$\sum_{i=1}^{2} z_i C_i = 0. \tag{5.3}$$

The fluid motion satisfies the Navier-Stokes equation:

$$\rho\left(\frac{\partial \mathbf{U}}{\partial T^*} + \mathbf{U}\cdot\nabla\mathbf{U}\right) = -\nabla P + \mu\nabla^2\mathbf{U} + \mathbf{J}\times\mathbf{B}. \tag{5.4}$$

The fluid is incompressible:

$$\nabla\cdot\mathbf{U} = 0. \tag{5.5}$$

In the above, ρ is the electrolyte's density; P is the hydrodynamic pressure;

and μ is the dynamic viscosity. The term $\mathbf{J} \times \mathbf{B}$ in equation (5.4) is the Lorentz body force. We assume that the solution is dilute; the solution properties are independent of the ion concentrations and are uniform throughout the solution; and buoyancy forces are negligible. The latter assumption is not always valid and, in fact, in many electrochemical processes buoyancy may play an important role (Qian et al., 2006). Nevertheless, since we wish to focus on centrifugal effects, we neglect buoyancy in this work.

The electron exchange reactions at the electrodes' surface are described by the Butler-Volmer kinetics (Bard & Faulkner, 2001):

$$\mathbf{n} \cdot \mathbf{H}_1|_{R=R_1,R_2} = \frac{J_e}{F}\left\{\frac{C_1}{\bar{C}_1} e^{-\alpha z_1 F/R_u T(V_{ext}^* - \Phi)} - e^{(1-\alpha) z_1 F/R_u T(V_{ext}^* - \Phi)}\right\}. \quad 5.6$$

Additionally, when the annulus if of a finite length,

$$\mathbf{n} \cdot \mathbf{H}_1|_{Z=0,L} = 0. \quad 5.7$$

In the above, V_{ext}^* is the external potential difference imposed across the electrodes, $\bar{C}_1$ is the uniform cation bulk concentration before the current was switched-on, J_e is the exchange current flux, α is the transfer coefficient, $\mathbf{n}$ is an outward unit vector, and Φ is the potential in the solution next to the electrode.

Mass conservation requires that

$$\int_{R_1}^{R_2}\int_{0}^{L} C_1 R \, dR \, dZ = \bar{C}_1 \frac{(R_2^2 - R_1^2)L}{2}. \quad 5.8$$

All solid surfaces are impermeable to the inert species A^{z_2},

$$\mathbf{n} \cdot \mathbf{H}_2|_{R=R_1,R_2;Z=0,L} = 0. \quad 5.9$$

The fluid velocity satisfies non-slip conditions at all solid surfaces

$$\mathbf{U}|_{R=R_1,R_2;Z=0,L} = 0. \tag{5.10}$$

The electric current flux:

$$\mathbf{J} = F\sum_{i=1}^{2} z_i \mathbf{H}_i. \tag{5.11}$$

Taking advantage of electro neutrality, we eliminate the potential from equation (5.1) to obtain the advection-diffusion equation

$$\frac{\partial C_i}{\partial T^*} = D^*\nabla^2 C_i - \mathbf{U}\cdot\nabla C_i, \tag{5.12}$$

where $D^* = (z_1 - z_2)D_1^* D_2^*/(z_1 D_1^* - z_2 D_2^*)$ and

$$\nabla\cdot(C_i\nabla\Phi) = -\frac{R_u T}{F} z^*\nabla^2 C_i \tag{5.13}$$

where $z^* = (D_1^* - D_2^*)/(D_1^* z_1 - D_2^* z_2)$.

Next, we convert the equations to a dimensionless form. To this end, we use the distance between the electrodes $d = R_2 - R_1$ as the length scale; $U_0 = \mu/\rho d$ as the velocity scale; the viscous shear $\mu U_0/d$ as the stress/pressure scale; $d/U_0 = \rho d^2/\mu$ as the time scale; the diffusive flux $H_0 = \bar{C}_1 D_1^*/d$ as the ion flux scale; $J_0 = FH_0$ as the electric current density scale; the thermal potential $R_u T/F$ as the electric potential scale; and the average concentration of the species M^{z_1}, $\bar{C}_1$ as the concentration scale. Furthermore, we define the mean radius $R_0 = (R_1 + R_2)/2$. Below, with the exceptions of V_{ext} and D_i, we express the dimensionless variables with the lower case version of their dimensional, upper case counterparts. The dimensionless applied potential is denoted as $V_{ext} = V_{ext}^* F/R_u T$ and the dimensionless diffusion coefficient $D_i = D_i^*/D_1^*$. The dimensionless time is denoted by t.

The dimensionless equations are:

$$\frac{\partial c_i}{\partial t} = -\frac{1}{\mathrm{Sc}}\nabla \cdot \mathbf{h}_i, \tag{5.14}$$

$$\mathbf{h}_i = \mathrm{Sc} \cdot \mathbf{u}c_i - D_i[\nabla c_i + z_i c_i(\nabla\phi - \chi \mathbf{u} \times \mathbf{e}_z)], \tag{5.15}$$

and

$$\frac{\partial \mathbf{u}}{\partial t} + \mathbf{u} \cdot \nabla \mathbf{u} = -\nabla p + \nabla^2 \mathbf{u} + \kappa(j_r \mathbf{e}_\theta - j_\theta \mathbf{e}_r). \tag{5.16}$$

In the above, $\mathrm{Sc} = \nu/D_1^*$ is the Schmidt number. The Lorentz number $\chi = \nu BF/(R_u T)$. $\kappa = J_0 B \cdot d^2/\mu U_0 = \rho F d^2 B \bar{C}_1 D_1^*/\mu^2$ is the ratio of the Lorentz force and the viscous shear. In electrolyte solutions, $\chi \ll 1$ and one can neglect the induced electromagnetic force in (5.15). In this chapter, we focus only on the axi-symmetric problem ($\partial/\partial\theta = 0$) and $j_\theta = 0$. The boundary conditions for ion fluxes $\mathbf{h}_i$ are

$$\mathbf{n} \cdot \mathbf{h}_1|_{r=r_1,r_2} = j_e\left\{c_1 e^{-\alpha z_1(V_{ext}-\phi)} - e^{(1-\alpha)z_1(V_{ext}-\phi)}\right\} \tag{5.17}$$

and

$$\mathbf{n} \cdot \mathbf{h}_2|_{r=r_1,r_2} = 0. \tag{5.18}$$

The electroneutrality condition requires that

$$\sum_{i=1}^{2} z_i c_i = 0. \tag{5.19}$$

The electric current density

$$\mathbf{j} = \sum_{i=1}^{2} z_i \mathbf{h}_i. \tag{5.20}$$

Mass conservation requires that

$$\int_{r_1}^{r_2}\int_{0}^{l} c_1 r \, dr \, dz = r_0 l. \tag{5.21}$$

The dimensionless form of equation (5.12)-(5.13) becomes:

$$\frac{\partial c_i}{\partial t} = -\frac{1}{\mathrm{Sc}}\nabla \cdot (\mathrm{Sc} \cdot \mathbf{u}c_i - D\nabla c_i), \tag{5.22}$$

where $D = D^*/D_1^*$ and

$$\nabla \cdot (c_i \nabla \phi) = -z^* \nabla^2 c_i. \tag{5.23}$$

5.3 Steady Flow of Binary Electrolyte in an Infinitely Long Annulus ($l \to +\infty$)

The Dean problem of pressure driven flow between two concentric cylinders has been studied extensively. Here, we consider the analogous MHD flow. While the Dean problem cannot be realized in a concentric annulus, the MHD flow can. When the flow is one-dimensional, the MHD flow is equivalent to pressure-driven flow (Qin & Bau 2010) and we can adopt the classical solution for Dean flow (Goldstein, 1938). We use the subscript "b" to denote the various dependent variables associated with the purely azimuthal flow.

Since the electric current is divergence-free, the electrical current flux

$$j_{r,b}(r) = \frac{j^* r_0}{r}, \tag{5.24}$$

where $j^* = j_{r,b}(r_0)$ is the current flux at the mid-distance between the electrodes $r_0 = r_1 + 1/2$. The azimuthal velocity is:

$$v_b(r) = \frac{\kappa j^* r_0}{2} r \left[\frac{1 - \left(\frac{r_2}{r}\right)^2}{1 - \left(\frac{r_2}{r_1}\right)^2} \ln\frac{r_2}{r_1} - \ln\frac{r_2}{r} \right]. \tag{5.25}$$

Fig. 5.2 depicts v_b as a function of $x = r - r_1$ $(0 \le x \le 1)$ for various values of r_1. Digilov (2007) derived equation (5.25) for MHD flow of liquid metals in the limit of a small Hartmann number. Since the magnitude of the current flux and thus

the body force decreases as r increases, the velocity attains its maximum value in the interval $r_1 < r < r_0$ $(0 < x < 0.5)$. When $r_1 \ll 1$, the velocity maximum is attained at $x \to 1/e$, and equation (5.25) simplifies to

$$v_b(x) = \frac{\kappa j^*}{4} x \ln x. \qquad 5.26$$

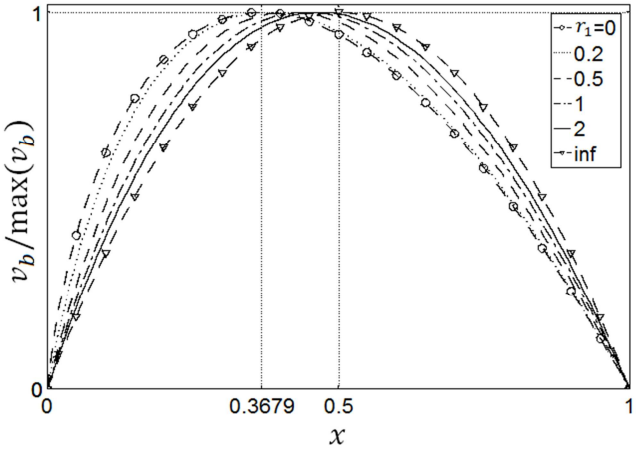

Figure 5.2 The azimuthal velocity v_b (normalized with its maximum value) as a function of x when $r_1 = 0,\ 0.2,\ 0.5,\ 1,\ 2, \text{and}\ \infty$. The vertical lines at $x = 1/e$ and $x = 1/2$ correspond, respectively, to the positions of the velocity maximum when the curvature is large and small.

As r_1 increases, the position of the velocity maximum shifts towards r_0 $(x = 0.5)$. When $r_1 \gg 1$ (small curvature), the velocity profile can be approximated as:

$$v_b(x) = \frac{\kappa j^*}{2} x(1 - x). \qquad 5.27$$

The latter expression is identical to the velocity profile of pressure-driven (Poiseuille) flow between two long parallel plates. The Reynolds number $\mathrm{Re} = \bar{v}_b$.

Next, we compute the concentration distribution. To this end, we solve the

Nernst-Planck equations (5.14) and (15)

$$\frac{d}{dr}\begin{pmatrix}c_{1b}\\c_{2b}\end{pmatrix}+\begin{pmatrix}z_1c_{1b}\\z_2c_{2b}\end{pmatrix}\frac{d\phi_b}{dr}=\begin{pmatrix}-r_0j^*/z_1r\\0\end{pmatrix}. \tag{5.28}$$

By introducing the scaled coordinate $\eta=\ln r$ ($\eta_1=\ln r_1<\eta<\ln r_2=\eta_2$), we convert equation (5.28) into a form similar to the one encountered in a planar geometry

$$\frac{d}{d\eta}\begin{pmatrix}c_{1b}\\c_{2b}\end{pmatrix}+\begin{pmatrix}z_1c_{1b}\\z_2c_{2b}\end{pmatrix}\frac{d\phi_b}{d\eta}=\begin{pmatrix}-r_0j^*/z_1\\0\end{pmatrix}=\begin{pmatrix}A\\0\end{pmatrix}. \tag{5.29}$$

In the above, the definition of the new variable A is apparent from the context. The solution of equation (5.29) together with the electroneutrality condition (5.19) and mass conservation (5.21) is

$$c_{1b}=1-\frac{Az_2}{(z_1-z_2)}\left[\eta+\frac{1}{2}+\frac{r_1^2\eta_1-r_2^2\eta_2}{2r_0}\right], \tag{5.30}$$

$$c_{2b}=-\frac{z_1}{z_2}c_{1b}, \tag{5.31}$$

and

$$\phi_b=G-\frac{1}{z_2}\ln[4r_0z_1(z_1-z_2)c_{1b}]. \tag{5.32}$$

The constant G in equation (5.32) is determined by one of the electrodes' potentials.

When an electric potential difference is applied across the electrode pair instead of the electric current, one needs to use the Butler-Volmer boundary conditions (5.17). Solving equation (5.17) and (5.30-5.32) provide the current-voltage relation.

Fig. 5.3 depicts the current flux as a function of the potential difference (ΔV_{ext}) across the electrode pair when $z_1=1$, $z_2=-1$, $r_1/r_2=2/3$, and $D_1=D_2=1$. The exchange current density $j_e=10^3$. The symbols and the solid line correspond, respectively, to the analytical solution and finite element solution of the Nernst-Planck

equations. The excellent agreement between the numerical and analytical results partially verifies the numerical code, which we will use later in the chapter.

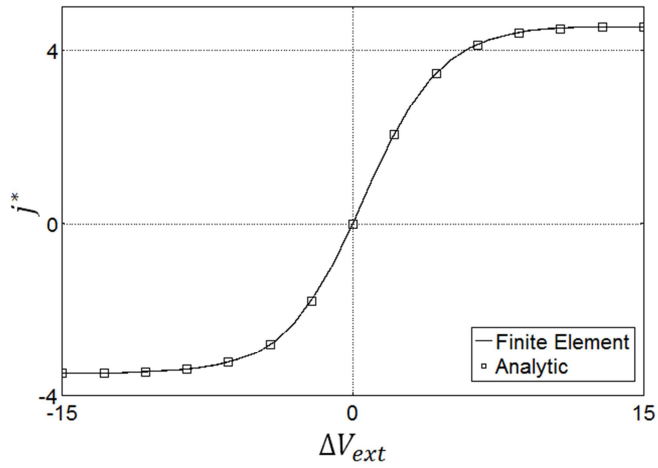

Figure 5.3 The electric current flux as a function of the potential difference between the electrodes. The dimensionless inner radius $r_1 = 2$. Binary, symmetric electrolyte, $z_1 = -z_2 = 1$. Dimensionless diffusion coefficients: $D_1 = D_2 = 1$. Exchange current density: $j_e = 10^3$. The symbols (squares) and the line correspond, respectively, to analytical solution and finite element simulation.

The positive (outward) $j_+^* = \frac{4z_1(z_1-z_2)(1-\delta)^2}{z_2(\delta^2-1-2\ln\delta)}$ and the negative (inward) $j_-^* = \frac{4z_1(z_1-z_2)(1-\delta)^2}{z_2(\delta^2-1-2\delta^2\ln\delta)}$ diffusion-limited electric current fluxes are, respectively, obtained by setting $c_{1b}(\eta = \eta_1) = 0$ and $c_{1b}(\eta = \eta_2) = 0$ in equation (5.30). In the above, $\delta = r_2/r_1 > 1$ is the radii ratio, $r_1 = 1/(\delta - 1)$, $r_2 = \delta/(\delta - 1)$, and $r_0 = (\delta + 1)/(2(\delta - 1))$. The forward and backward limiting current fluxes differ in magnitude ($|j_+^*| > |j_-^*|$). For example, for the conditions of Fig. 5.3, $-3.48 \le j^* \le 4.56$. **Fig. 5.4** depicts the ratio of the outward and inward limiting current fluxes $|j_+^*|/|j_-^*|$ as a function of the radii ratio δ. When $\delta \sim O(1)$, $|j_+^*|/|j_-^*| \sim (2\delta + 1)/3$

(dotted line in Fig. 5.4). When $\delta \gg 1$, $|j_+^*|/|j_-^*| \sim (2\ln\delta - 1)$ (dashed line in Fig. 5.4).

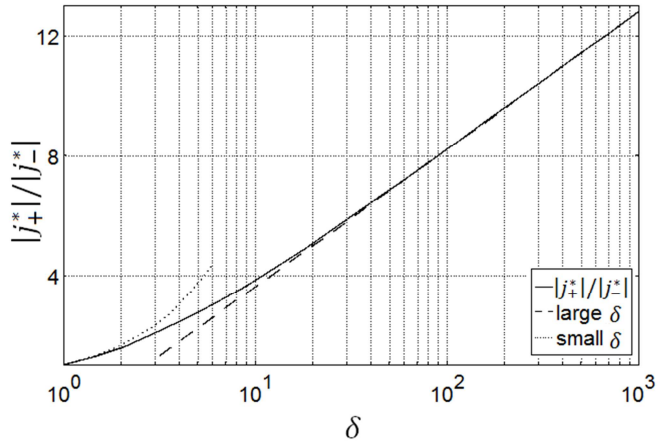

Figure 5.4 The ratio between the outward and the inward limiting current fluxes ($|j_+^*|/|j_-^*|$) as a function of the radii ratio δ. $D_1 = D_2 = 1$, $z_1 = -z_2 = 1$, and $j_e = 10^3$. The dashed line $(2\ln\delta - 1)$ corresponds to the large δ asymptote. The dotted line is the small δ asymptote $(2\delta + 1)/3$.

Fig. 5.5 depicts the concentration c_{1b} as a function of the radial coordinate r under conditions of outward (dashed line) and inward (solid line) limiting current fluxes. In the inward current flow case, the concentration c_{1b} builds up next to the surface of the outer electrode and depletes next the surface of the inner electrode. In the outward current case, the opposite is true. Since the surface area of the outer electrode is δ times larger than that of the inner electrode, the maximum concentrations in the case of outer directed current is larger than that in the case of inward directed current. Accordingly, the concentration gradient in the inward current case is smaller than in the outward current case, providing less diffusive flux, and thus

less net current density.

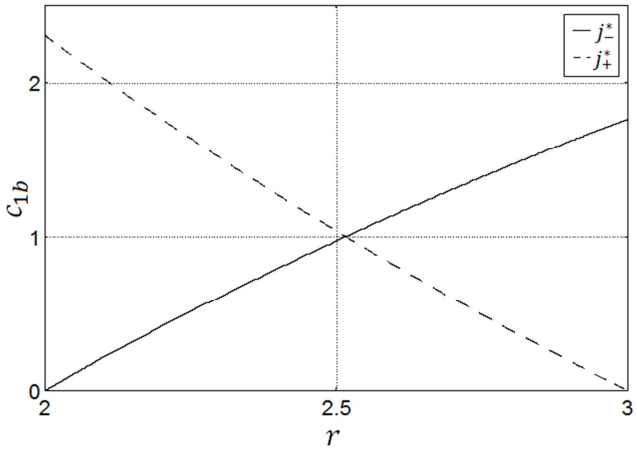

Figure 5.5 The concentration c_{1b} as functions of the radius r under limiting current conditions when the current is directed outwardly (dashed line) and inwardly (solid line). All other conditions are the same as in Fig. 5.3.

Next, we consider the case of a small gap size ($r_1 \gg 1$), i.e., small curvature and nearly planar geometry. In this case, the electric current flux $j_{r,b} \sim j^*$ is independent of radial position. Equations (5.30-5.32) reduce to

$$c_{1b} = 1 - \frac{j^*}{j_1}(2x - 1), \tag{5.33}$$

$$c_{2b} = -\frac{z_1}{z_2} c_{1b}, \tag{5.34}$$

and

$$\phi_b = G - \frac{1}{z_2} \ln(j_1 c_{1b}). \tag{5.35}$$

The potential difference across the gap

$$\Delta\phi = \phi_b(x = 0) - \phi_b(x = 1) = -\frac{1}{z_2} \ln \frac{j_1 + j^*}{j_1 - j^*}, \tag{5.36}$$

where $j_1 = 2z_1(z_2 - z_1)/z_2$ is the dimensionless limiting diffusion-migration current.

With the aid of the Butler-Volmer boundary condition, we obtain the current-voltage relation. **Fig. 5.6** depicts the electric current flux as a function of the potential difference $\Delta V_{ext} = V_{ext}(x=0) - V_{ext}(x=1)$ when the exchange current density $j_e = 10^{-3}$, 10^{-2}, $10^{-1}, 1$, 10^{1}, 10^{2} and 10^{3}. $z_1 = -z_2 = 1$, $D_1 = D_2 = 1$, and $\alpha = 0.5$.

At large values of the exchange current density j_e, the Butler-Volmer relation (5.17) reduces to the Nernst equation at both boundaries $x = 0$ and $x = 1$:

$$\phi_b = V_{ext} - \frac{1}{z_1}\ln c_{1b}. \qquad 5.37$$

With the aid of equation (5.36) , the current-potential relation could be expressed as:

$$j^* = j_1 \tanh\frac{z_2 \Delta V_{ext}}{2(z_2 - 1)}. \qquad 5.38$$

Fig. 5.6 compares the predictions of the Nernst model (solid line) with the Butler-Volmer model when $j_e = 10^3$ (stars). Witness that both models provide nearly identical results when the exchange current is large.

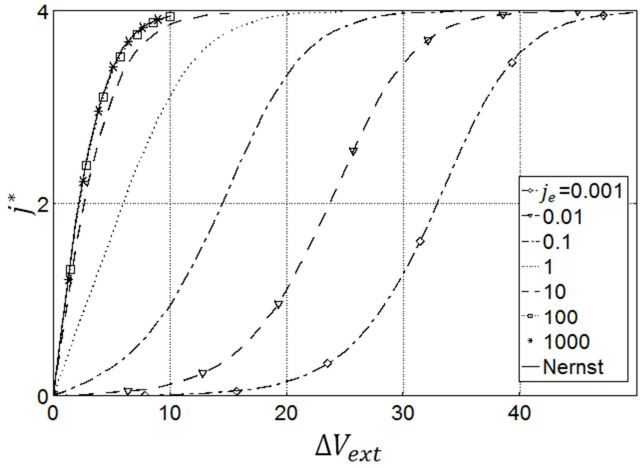

Figure 5.6 The current flux as a function of the potential difference between the electrodes when the exchange current density $j_e = 10^{-3}, 10^{-2}, 10^{-1}, 1, 10^{1}, 10^{2}, \text{and } 10^{3}$. The curvature is neglected. Binary,

symmetric electrolyte, $z_1 = -z_2 = 1$, and $D_1 = D_2 = 1$. Butler-Volmer electrode kinetics are used with $\alpha = 0.5$. The solid line corresponds to predictions obtained with the Nernst equation.

5.4 The Stability of the Azimuthal Flow

In this section, we study for the first time, the linear stability of the MHD azimuthal flow in an infinitely long annulus. In the classical Dean problem, at sufficiently high azimuthal velocities, centrifugal accelerations destabilize the purely azimuthal flow and give rise to convective rolls in the transverse $r - z$ plane. In the electrochemical problem, the secondary flows modify the concentration distribution and, thus, the current flux, which, in turn, affects the Lorentz body force. Hence, the stability characteristics of the electrochemical problem are expected to significantly differ from those of the classical pressure-driven, Dean problem.

The analysis presented here is restricted to an annulus with small curvature (small gap approximation). Following Dean's (1928) original treatment, we neglect the effect of centrifugal accelerations on the base flow. Centrifugal effects are, however, accounted for in the perturbation equations.

We perturb the base flow variables (equations 5.14-5.16) with small disturbances, which we denote with the superscript tilde. For example, the concentration field assumes the form $c_i = c_{ib} + \varepsilon \tilde{c}_i$, where $\varepsilon \ll 1$, c_{ib} is the base solution (obtained in section 5.3), and $\tilde{c}_i$ is the first order perturbation. All other dependent variables are similarly perturbed. The perturbed variables are introduced into the equations and

only terms of $O(\varepsilon)$ are retained. Furthermore, we decompose the perturbations into normal modes, i.e.,

$$\tilde{c}_i = \hat{c}_i(x)e^{\sigma t+ikz}, \tag{5.39}$$

where σ is the growth rate; k is the wave number, and $\hat{c}_i$ is a function of x only. In the above, we assume that two-dimensional disturbances are less stable than three-dimensional ones. This assumption is consistent with Squire's theorem (Khalzov et al. 2006, Drazin & Reid, 2010). Accordingly, we consider only two-dimensional disturbances and all the perturbation variables are independent of θ (i.e., $\partial/\partial\theta = 0$).

Invoking the small curvature approximation, $1/x \ll \partial/\partial x$, and omitting the superscript tilde ($\widehat{\ }$), we obtain the $O(\varepsilon)$ linearized momentum equations:

$$(\mathrm{E}^2 - k^2 - \sigma)(\mathrm{E}^2 - k^2)g = vx(1-x), \tag{5.40}$$

$$(\mathrm{E}^2 - k^2 - \sigma)v + \kappa j_x = \Lambda k^2 g(1-2x), \tag{5.41}$$

and the continuity equation

$$\mathrm{E}u + ikw = 0. \tag{5.42}$$

The impermeability and no-slip boundary conditions at $x = 0$ and $x = 1$ are:

$$g = \mathrm{E}g = v = 0. \tag{5.43}$$

For convenience, we introduced in the above the rescaled, radial velocity $g = u \cdot r_1/(\kappa j^* k^2)$. The operator $\mathrm{E} = d/dx$. $\Lambda = 72\bar{v}_b{}^2/r_1 = 72\mathrm{Dn}^2$, where Dn is the Dean number $\mathrm{Dn} = |\bar{v}_b|\sqrt{1/r_1}$. Equations (5.40-5.43) with $\kappa = 0$ are identical to the ones associated with the classical Dean problem (Drazin and Reid, 2010). The term κj_x is due to the Lorentz body force. This term couples the hydrodynamics and the electrochemistry.

From equations 5.22 and 5.23, we obtain, respectively, the linearized mass conservation equations for species 1:

$$\mathrm{E}^2 c_1 = \left(\frac{\mathrm{Sc}}{D}\cdot\sigma + k^2\right)c_1 + \frac{\mathrm{Sc}}{D}\cdot u\mathrm{E}c_{1b}. \tag{5.44}$$

The equation for the potential ϕ is:

$$\begin{aligned} c_{1b}\mathrm{E}^2\phi = -z^*(\mathrm{E}^2 - k^2)c_1 + k^2 c_{1b}\phi - c_1\mathrm{E}^2\phi_b - \mathrm{E}c_1\mathrm{E}\phi_b \\ - \mathrm{E}c_{1b}\mathrm{E}\phi. \end{aligned} \tag{5.45}$$

The linearized flux of species i is:

$$h_{ix} = \mathrm{Sc}\cdot uc_{ib} - D_i\mathrm{E}c_i - z_i D_i(c_{ib}\mathrm{E}\phi + c_i\mathrm{E}\phi_b). \tag{5.46}$$

The perturbation in the electric flux is:

$$\begin{aligned} j_x = \sum_{i=1}^{2} z_i h_{ix} = -\sum_{i=1}^{2} z_i D_i[\mathrm{E}c_i + z_i(c_{ib}\mathrm{E}\phi + c_i\mathrm{E}\phi_b)] \\ = (D_2 - 1)z_1\mathrm{E}c_1 + (z_2 D_2 - z_1)(z_1 c_{1b}\mathrm{E}\phi + z_1 c_1\mathrm{E}\phi_b) \end{aligned} \tag{5.47}$$

The perturbed concentrations satisfy the electro-neutrality condition

$$\sum_{i=1}^{2} z_i c_i = 0. \tag{5.48}$$

Below, we consider two types of boundary conditions. In the first instant, we assume that the current flux is specified at the electrodes' surfaces. This problem is mostly of theoretical interest as it is difficult to control the local current flux in practice. In the second instance, we specify the electrodes' potentials.

In each case, we solve the eigenvalue problem (5.40-5.48) and the appropriate electrochemical boundary conditions (to be specified later) with finite elements. Briefly, we select a wave number k and either the base current j^* or the applied potential ΔV_{ext}. The growth rate $\sigma(\mathrm{Dn}, k)$ is then calculated as a function of the

Dean number Dn and the wave number k. The Dean number at marginal stability $\mathrm{Dn}_0(k)$ nullifies the real part of the growth rate, i.e., $\mathrm{real}\big(\sigma(\mathrm{Dn}_0, k)\big) = 0$. We seek the *most dangerous* wave number k_0 that minimizes $\mathrm{Dn}_0(k)$. In all our calculations, we find the growth rate σ to be real, and the principle of exchange of stability to hold.

To check our algorithm, we consider the hypothetical case of non-zero base velocity and $j_x = 0$. In this case, the κj_x term in equation (5.41) vanishes and the stability problem reduces to the classical Dean problem. Our finite element solution reproduces the well-known, classical results of $\mathrm{Dn}_0 = 35.92$ and $k_0 = 3.95$ (Dean, 1928, and Drazin & Reid, 2010). The bifurcating solution consists of convective rolls in the $r - z$ plane.

5.4.1 The Case of Controlled Current

When the current flux is specified, the perturbation in the current is zero. The corresponding boundary conditions at $x = 0,1$ are

$$\mathrm{E}c_1 = 0 \tag{5.49}$$

and

$$\mathrm{E}\phi = -\frac{c_1 \mathrm{E}\phi_b}{c_{1b}}. \tag{5.50}$$

To determine the marginal stability curve, we calculated the growth rate σ as a function of Dn for a given k. **Fig. 5.7** depicts σ as functions of Dn when $k = 1$ (dashed line), 2.39 (solid line), and 4 (dashed-dot line). In all cases, σ is real. At criticality, $\sigma = 0$. This calculation was done for a binary and symmetric electrolyte. $z_1 = -z_2 = 1$, diffusion coefficients ${D_1}^* = {D_2}^* = 10^{-9} m^2/s$, $\bar{C_1} = 10^4 mol/m^3$.

$R_1 = 0.5m$. $R_2 = 0.505m$. $B = 0.4T$. $\rho = 10^3 kg/m^3$. $\mu = 10^{-3} Pa \cdot s$, and $j^* > 0$.

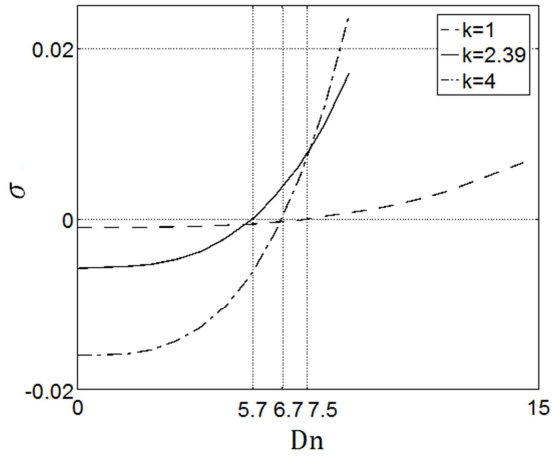

Figure 5.7 The disturbance growth rate σ as a function of the Dean number when k=1 (dashed line), 2.39 (solid line), and 4 (dashed-dot line). Binary electrolyte with $z_1 = -z_2 = 1$. $D_1^* = D_2^* = 10^{-9} m^2/s$, $\bar{C}_1 = 10^4 mol/m^3$. $R_1 = 0.5m$. $R_2 = 0.505m$. $B = 0.4T$. $\rho = 10^3 kg/m^3$. $\mu = 10^{-3} Pa \cdot s$.

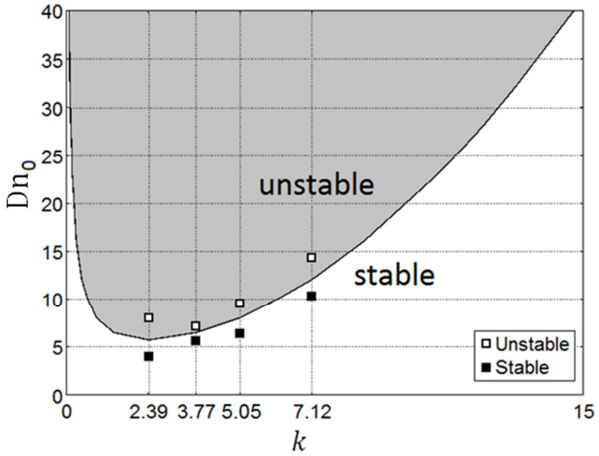

Figure 5.8 The critical Dean number Dn_0 at the onset of instability, predicted by linear stability analysis, as a function of the wave number k. The electrodes' current is controlled. The white and gray areas correspond, respectively, to stable ($\sigma < 0$) and

unstable ($\sigma > 0$) states. The symbols correspond to finite element solutions of the nonlinear equations. The solid and hollow symbols correspond, respectively, to subcritical (Dn^-) and supercritical (Dn^+) cases. The symbols are located at $\{k,\ \mathrm{Dn}^-,\ \mathrm{Dn}^+\} = \{2.39, 4.02,\ 8.04\}$, $\{3.77,\ 5.63,\ 7.24\}$, $\{5.05,\ 6.43,\ 9.65\}$ and $\{7.12,\ 10.45, 14.47\}$. The other conditions are the same as in Fig. 5.7.

Fig. 5.8 depicts the Dean number at marginal stability (Dn_0) as a function of the wave number k for the same conditions as in Fig. 5.7. The white and gray regions correspond, respectively, to stable ($\sigma < 0$) and unstable ($\sigma > 0$) states. Both the critical Dean number $\mathrm{Dn}_c = 5.7$ and the critical wave number $k_c = 2.39$ are smaller than that in the classical Dean's problem. Interestingly, when $j^* < 0$, the base state is linearly stable for *all* values of the Dean number.

The linear stability results were compared with the results of numerical solutions of the full nonlinear equations. The computational domain consisted of a segment of the annulus with height $0 < z < 2\pi/k$. Periodic boundary conditions imposed in the $z-$direction, i.e, all the dependent variables satisfy the condition: $a(x, z, t) = a(x, z + 2\pi/k\,, t)$. In the calculations, we used: $k = 2.39,\ 3.77,\ 5.05$ and 7.12. When the calculations converged to the azimuthal base flow, the state was designated as stable. When the calculation converged to a state that consisted of convective cells in the $x - z$ plane, the state was designated as unstable. In all the cases considered here, the calculations eventually converged to a steady-state. The numerically identified stable and unstable states are denoted, respectively, with solid

and hollow squares in Fig. 5.8. The finite element solutions of the nonlinear equations are consistent with the predictions of the linear stability theory.

In all cases, consistent with the principle of exchange of stability, the transients were monotonic and no oscillations were observed. The finite element simulations suggest that the bifurcation from the azimuthal base flow to the three-dimensional flow is supercritical.

Fig. 5.9 depicts the scaled eigenfunctions c_1 (dashed line), ϕ (dotted line with squares), g (dot-dashed line), v (solid line), and j_x (solid line with circles) as functions of x when $\mathrm{Dn} = 8.04$, and $k = 2.39$. In Fig. 5.9a, $j_b = 0.1$ and $\sigma = 0.011$. In Fig. 5.9b, $j_b = -0.1$ and $\sigma = -0.016$. All the other parameters are the same as in Fig. 5.7. Witness the significant difference in the structure of the eigenvectors between the case of the outwardly directed current (Fig. 5.9a) and the inwardly directed current (Fig. 5.9b). When the current is directed outwardly (Fig. 5.9a), the perturbations v, g, j_x and c_1 remain of the same sign for all values of x, and resemble a symmetric behavior about $x = 0.5$. In contrast, when the current is directed outwardly, all the depicted eigenvectors change sign in the domain $0 < x < 1$, and exhibit asymmetric behavior about $x = 0.5$.

Fig. 5.10 depicts a sample of the finite element solution of the nonlinear problem. The colors correspond to the concentration c_1. The lines are the streamlines of the secondary flow in the $r - z$ plane. Fig. 5.10a describes the case of inwardly directed current of magnitude $j^* = -0.1$ and $\mathrm{Dn} \approx 8$. Fig. 5.10b depicts the case when the outward current $j^* = 0.05$ and $\mathrm{Dn} \approx 4$. This corresponds to a subcritical state

($\mathrm{Dn} < \mathrm{Dn}_0$). Consistent with the predictions of the linear stability theory, there are no secondary flows in this case, and the concentration distribution is uniform in the z direction. Fig. 5.10c depicts the concentration and flow fields when the outward current $j^* = 0.1$ and $\mathrm{Dn} \approx 8$ are supercritical ($\mathrm{Dn} > \mathrm{Dn}_0$). Consistent with the predictions of the linear stability analysis, convective rolls appear in the $r - z$ plane. The center of rotation is at $r \sim r_C$, where r_C is slightly larger than r_0. This flow pattern is consistent with the eigenvectors depicted in Fig. 5.9a. Fig. 5.10d depicts the magnitude of the current flux under the same conditions as in Fig. 5.10c.

Fig. 5.10c should be contrasted with Fig. 5.10a. Although both cases correspond to the same Dean number, there are no secondary rolls present in the case of the inward current flow (a) while secondary flow is present in the case of the outward current flow (c). Consistent with the results of the linear stability theory, the nonlinear simulations predict absence of secondary flows in the case of inward (negative) current.

In conclusion, when the base current is directed outwardly, the magnetohydrodynamic Dean problem is less stable than the pressure-driven one, while when the base current is directed outwardly, the opposite is true. So, what are the mechanisms that modify the stability characteristics of the classical Dean problem? To answer this question, we need to consider the ion concentration field in the annulus. When the current is directed outwardly, the ion concentration next to the inner surface(electrode) is larger than in the bulk of the solution. See Fig. 5.10a and Fig. 5.5. When due to the Dean (centrifugal) instability, fluid motion is induced away from the

inner surface, the fluid advects ions into the bulk of the solution. This increases the local electric conductivity and the current flux. Witness the concentration “plumes” next to the bottom and top boundaries next on the left hand side of Fig. 5.10c. This, in turn, enhances the Lorentz body force, increases the local azimuthal velocity and the resulting centrifugal acceleration, thereby enhancing the instability. For this reason, the eigenvectors associated with the perturbed quantities c_1, g, v and j_x all have the same sign (Fig. 5.9a). And, for this reason, the magnetohydrodynamic Dean problem is less stable than the pressure-driven one.

a)

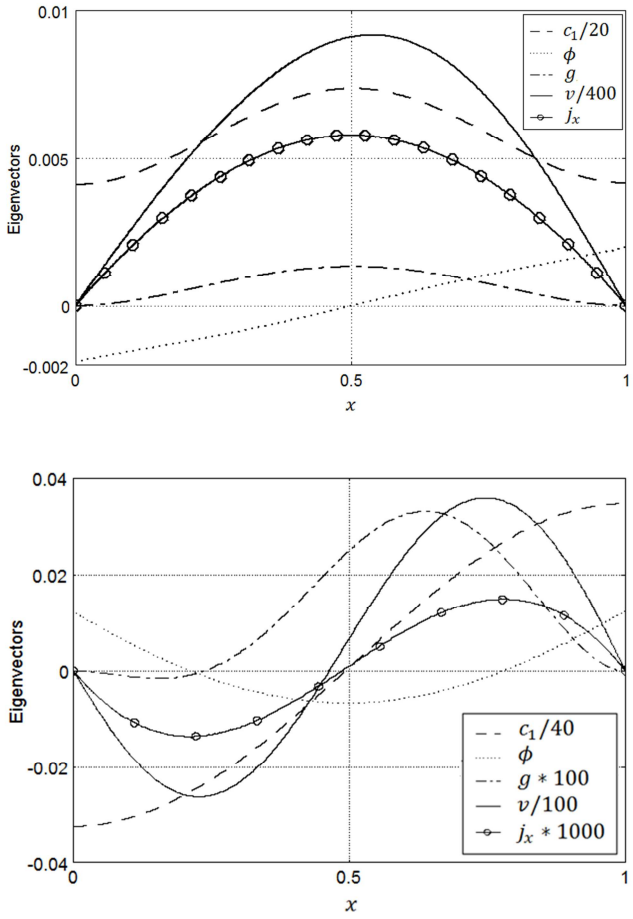

Figure 5.9 The scaled eigenvectors c_1, ϕ, g, v and j_x as functions of x. Constant electric current is imposed across the electrodes. $\mathrm{Dn} = 8.04$. $k = 2.39$. (a) $j_b = 0.1$,

$\sigma = 0.011$; (b) $j_b = -0.1,\ \sigma = -0.016$. Other parameters are the same as in Fig. 5.7.

When the base current is directed inwardly, the ion concentration next to the inner surface is smaller than in the bulk of the solution. See Fig. 5.10b and Fig. 5.5. When centrifugal effects (Dean instability) cause a radial, outward convective disturbance, the advection reduces the local ion concentration and the corresponding electric conductivity away from the surface, which in turn causes a reduction in the Lorentz body force, a reduction in the azimuthal velocity, and a reduction in the centrifugal acceleration, which mitigates the effect of the disturbance. Thus, the disturbance is suppressed. Thus, when the current is directed inwardly, electrochemical effects suppress centrifugal instabilities.

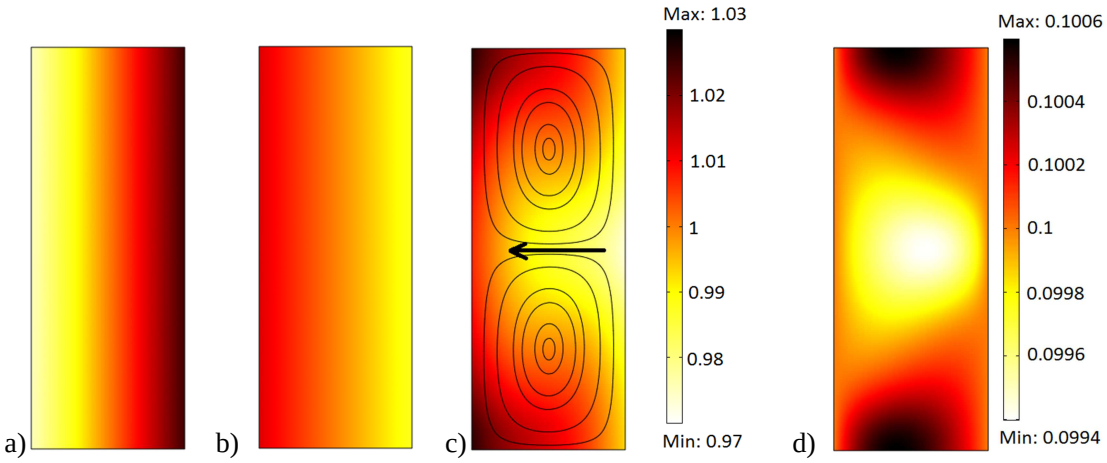

Figure 5.10 The concentration distribution of c_1 when (a) $j^* = -0.1,\ \mathrm{Dn} = 8.04$; (b) $j^* = 0.05,\ \mathrm{Dn} = 4.02$; and (c) $j^* = 0.1,\ \mathrm{Dn} = 8.04$. The black solid lines in (c) are the streamlines associated with the secondary flow in the $r - z$ plane. The arrow

shows the flow direction. (d) Electric current flux distribution for case (c). All the other parameters used are the same as in Fig. 5.7.

5.4.2 The Case of Controlled Potential and Butler-Volmer Boundary conditions

In this section, we consider the more realistic case when the potential difference between the electrodes is controlled. The injected current, as a function of the overpotential and the concentration, is given by the Butler-Volmer equation. The perturbed (linearized) Buttler-Volmer boundary conditions at the electrodes' surfaces are:

$$\mathbf{n}\cdot\mathbf{h}_{1x} = j_e\big[(c_{1b}\alpha z_1\phi + c_1)e^{-\alpha z_1(V_{ext}-\phi_b)} + (1-\alpha)z_1\phi e^{(1-\alpha)z_1(V_{ext}-\phi_b)}\big] \tag{5.51}$$

and

$$\mathbf{n}\cdot\mathbf{h}_{2x} = 0. \tag{5.52}$$

Together with equation (46), we obtain the boundary conditions:

$$\mathrm{E}\phi = -\frac{h_{1x}}{(z_1-z_2)c_{1b}} - \frac{c_1\mathrm{E}\phi_b}{c_{1b}} \tag{5.53}$$

and

$$\mathrm{E}c_1 = \frac{h_{1x}z_2}{z_1-z_2}. \tag{5.54}$$

We solve the linear stability problem in a similar way to what we have done in the previous section. Briefly, we specify the wave number and the Dean number and compute the eigenvalue $\sigma = \sigma(\mathrm{Dn}, k)$. As in the controlled current case, σ is always real and the principle of exchange of stability prevails. We then determine the value of $\mathrm{Dn}_0(k)$ that correspond to $\sigma = 0$.

Fig. 5.11 depicts the critical Dean number Dn_0 as a function of the wave

number. The white and gray areas correspond to stable ($\sigma < 0$) and unstable ($\sigma > 0$) cases. When using the same electrolyte and conditions as specified in Fig. 5.7 (outwardly directed base current), exchange current density of $j_e = 6 \times 10^{-3}$ and $\alpha = 0.5$, we find that the critical Dean number $Dn_0 = 4.17$ and the critical wave number $k_0 = 0.74$. Expectedly, since the potential boundary condition is less restrictive than the current flux condition (section 5.4.1), the critical Dean number in the potential-controlled case is smaller than in the current-controlled case. When the base current is directed inwardly, the azimuthal flow is stable for all Dean numbers.

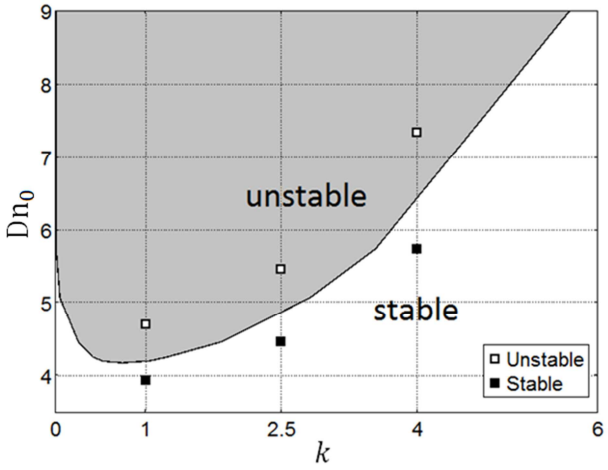

Figure 5.11 The critical Dean number Dn_0 at the onset of instability as a function of the wave number. An infinitely long annular conduit with controlled electric potential applied across the electrodes. The white and gray areas correspond, respectively, to stable ($\sigma < 0$) and unstable ($\sigma > 0$) cases. The hollow (Dn^+) and solid (Dn^-) symbols correspond, respectively to subcritical and supercritical cases. The symbols are located at $\{k, \mathrm{Dn}^- \mid \mathrm{Dn}^+\} = \{1, 3.93 \mid 4.69\}$, $\{2.5, 4.46 \mid 5.45\}$ and $\{4, 5.73 \mid 7.34\}$. $j_e = 6 \times 10^{-3}$. $\alpha = 0.5$. $D_1^* = D_2^* = 10^{-9} m^2/s$, $\bar{C}_1 = 10^4 mol/m^3$.

$R_1 = 0.5m.\ R_2 = 0.505m.\ B = 0.4T.\quad \rho = 10^3 kg/m^3.\ \mu = 10^{-3} Pa \cdot s.$

The predictions of linear stability theory were compared with the results of the nonlinear, finite element simulations of equations (5.14-5.16) and Butler-Volmer boundary conditions. The simulations were carried out for an annuli with heights $l = 2\pi/k$, where $k = 1,\ 2.5,$ and 4, and periodic boundary conditions at the top and bottom boundaries. The results of the numerical simulations are summarized with symbols in the stability diagram (Fig. 5.11). The solid and hollow squares correspond, respectively, to subcritical $(\mathrm{Dn} = 3.93,\ 4.46, \text{and } 5.73)$ and supercritical $(\mathrm{Dn} = 4.69, 5.45, \text{and } 7.34)$ flows. The finite elements, nonlinear solutions are consistent with the predictions of the linear stability analysis.

Fig. 5.12a and 5.12b depict, respectively, the results of the nonlinear finite elements simulations when the electrodes' potentials are controlled. Fig. 5.12a and Fig. 5.12b correspond, respectively, to the subcritical $(\mathrm{Dn} = 5.73)$ and supercritical $(\mathrm{Dn} = 7.34)$ concentrations and flow fields in the $r - z$ plane when $k = 4$ and the base current is outwardly directed. All other conditions are the same as in Fig. 5.11. When the base current is inwardly directed, the finite element calculations converged to a purely azimuthal flow consistent with predictions of linear stability analysis.

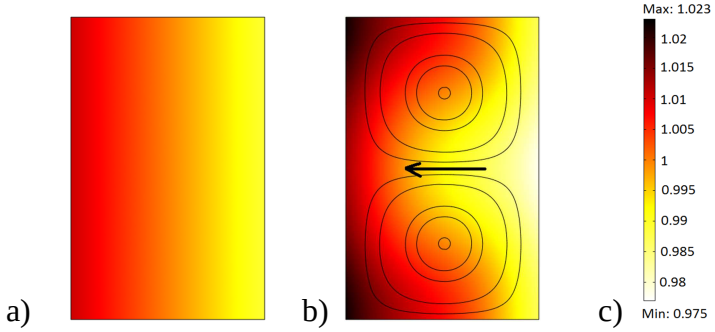

Figure 5.12 Ion concentration distribution c_1 in the controlled potential case described in Fig. 5.10. (a) subcritical state $\mathrm{Dn} = 5.73$. (b) supercritical state $\mathrm{Dn} = 7.34$. The solid lines are the streamlines of the secondary flow. $k = 4$. All the other parameters are the same as used in Fig. 5.11.

5.4.3 The Case of Controlled Potential with Nernst Boundary condition

When the electrode kinetics is rapid (large exchange current), the Butler-Volmer equations can be simplified to the Nernst boundary conditions (equation 5.37). The perturbed boundary conditions are then:

$$\phi = \frac{c_1}{z_1 c_{1b}} \tag{5.55}$$

and

$$\mathrm{E}c_1 = c_{1b}\mathrm{E}\phi + c_1\mathrm{E}\phi_b. \tag{5.56}$$

To verify the linear stability analysis presented in section 5.4.2, we repeated the linear stability calculations using the simpler boundary conditions (5.55) and (5.56). All other parameters are the same as in Fig. 5.11. **Fig. 5.13** depicts Dn_0 as a function of k as obtained using Butler-Volmer electrode kinetics when $j_e = 10^3$ (solid line) and the Nernst condition (symbols). The agreement between calculations based on the Butler-Volmer kinetics and the Nernst kinetics is nearly perfect in the case of large exchange current density.

5.5 An Annulus with a Finite Height ($\mathbf{l < \infty}$)

When the annulus has a finite height, purely azimuthal flow is not possible and

secondary flows will always be present in the $r-z$ plane. We first examine the range of validity of the small gap approximation, which we have employed in section 5.4. Then, we compare the intensity of the secondary flows between the cases of the outward and inward currents.

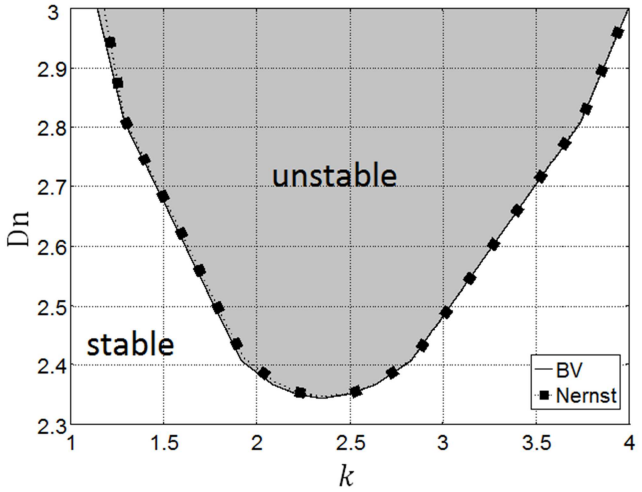

Figure 5.13 The critical Dean number at the onset of instability as a function of the wave number. Controlled potential case. The white and gray areas correspond, respectively, to stable ($\sigma < 0$) and unstable ($\sigma > 0$) states. The dotted line with solid squares corresponds to the solution of the linear stability problem with Nernst boundary conditions. The solid line corresponds to the Butler-Volmer boundary conditions with $j_e = 10^3$ and $\alpha = 0.5$. All the electrolyte properties are the same as used for Fig. 5.7.

5.5.1 The Range of Validity of the Small Gap Approximation

When the conduit curvature is small, often the quasi-two-dimensional model (the Dean's approximation) is employed (Dean 1928) as we have done in section 5.4. To

assess the validity of the Dean approximation in our case, we compare the predictions of the two-dimensional model with the predictions of the axisymmetric model. The corresponding axi-symmetric momentum and continuum equations are, respectively,

$$u\frac{\partial u}{\partial r}+w\frac{\partial u}{\partial z}=-\frac{\partial p}{\partial r}+\frac{\partial^2 u}{\partial r^2}+\frac{\partial^2 u}{\partial z^2}+\frac{v^2}{r}, \quad 5.57$$

$$u\frac{\partial v}{\partial r}+w\frac{\partial v}{\partial z}=\kappa j_r+\frac{\partial^2 v}{\partial r^2}+\frac{\partial^2 v}{\partial z^2}, \quad 5.58$$

$$u\frac{\partial w}{\partial r}+w\frac{\partial w}{\partial z}=-\frac{\partial p}{\partial z}+\frac{\partial^2 w}{\partial r^2}+\frac{\partial^2 w}{\partial z^2}, \quad 5.59$$

and

$$\frac{\partial u}{\partial r}+\frac{\partial w}{\partial z}=0. \quad 5.60$$

Additionally, one needs to solve the Nernst-Planck equations (5.14-5.15) for the concentration field.

We characterize the intensity of the secondary flow in the $r-z$ plane with its kinetic energy $\|\mathbf{u}_\perp\|^2=\oiint(u^2+w^2)dxdz$. **Fig. 5.14** depicts $\|\mathbf{u}_\perp\|^2$ as a function of the curvature r_1 when $l=2$. Non-slip boundary conditions are imposed at $z=0$ and $z=l$. The crosses and circles correspond to axi-symmetric and two-dimensional predictions. The inset depicts the relative difference (%) between the axi-symmetric and two-dimensional simulations as a function of r_1. When $r_1>40$ (curvature of 0.025), the difference between the two models predictions is smaller than 1%. The two-dimensional model overestimates the kinetic energy of the secondary flow. This is consistent with results previously obtained for pressure-driven Dean flow. Finlay & Nandakumar (1990) and Yanase et al. (1994) argued, respectively, that the Dean approximation is applicable when the curvature is smaller than 0.1 and 0.01.

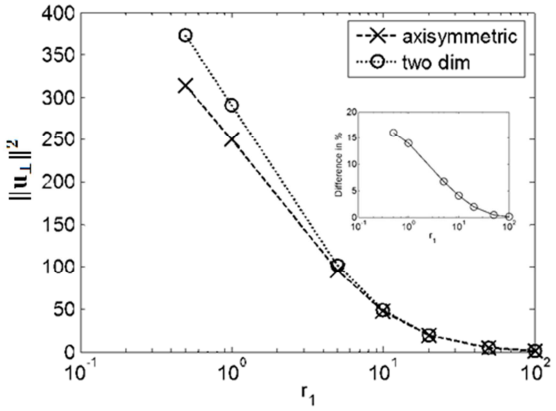

Figure 5.14 The kinetic energy of the secondary flow $\|\mathbf{u}_\perp\|^2$ as a function of r_1. $D_1 = D_2 = 1$. $j^* = 0.15$. $l = 2$. The dotted line with circles corresponds to results of the simplified, two-dimensional model. The dashed line with crosses shows results of the axisymmetric model. The inset depicts the relative difference between the approximate model and exact model predictions as a function of r_1.

5.5.2 The Effect of Current Direction on Secondary Convection

A somewhat unexpected result of our linear stability analysis of the flow in the azimuthal flow in the infinitely tall annulus is the strong dependence on the direction of the current flow. While in the infinitely long annulus secondary flows evolve only when the current is directed outwardly, the situation is quite different in the case of the finite-height annulus. As we have noted earlier, when the annulus is of finite height, secondary flows are always present regardless of the current's direction. These secondary flows are due to pressure gradients caused by the non-slip floor and ceiling.

Fig. 5.15 depicts the flow patterns and the concentration distributions (a and b) and the current fluxes intensity (c and d) when the current is directed outwardly (a and c) and when the current is directed inwardly (b and d). The annulus height $l =$

$2\pi/2.39$. No slip conditions are specified at $z = 0$ and $z = l$. All other conditions are the same as in Fig. 5.7. In both cases, the secondary flow is directed towards the outer cylinder at the mid-height plane, and returns towards the inner cylinder next to the top and bottom boundaries. When the current is directed outwardly, the ion concentrations are higher close to the inner cylinder's surface. These ions are advected outwardly forming a higher concentration/ higher electric conductivity "plume" at the annulus' midheight plane, which results in a higher current density, larger Lorentz force, and enhanced azimuthal velocity (Fig. 5.15a). In contrast, when the current is directed inwardly, the midheight plane contains fewer ions than in the absence of secondary flows (Fig. 5.15b) and the driving force is slightly reduced. As the result, the azimuthal velocity in the case of the outwardly-directed current (average azimuthal velocity 61.13) is larger than in the case of the inwardly directed current (average azimuthal velocity 61.12).

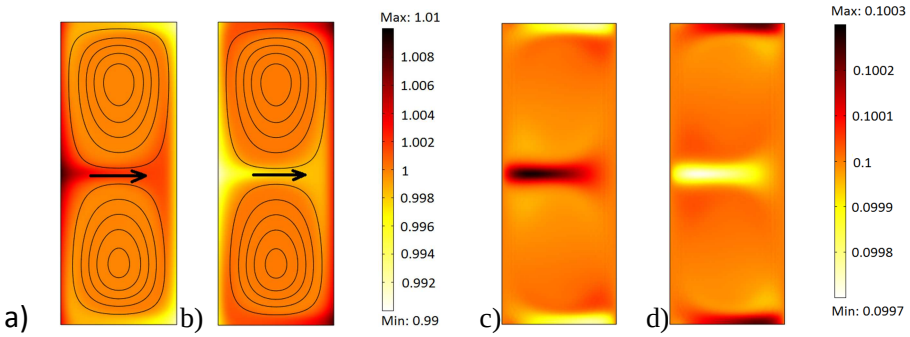

Figure 5.15 MHD flow in an annulus of height $l = 2\pi/2.39$. (a) Concentration distribution c_1 and the (u, w) streamlines when a) $j^* = 0.1$; (b) Concentration distribution c_1 and the (u, w) streamlines when $j^* = -0.1$. (c) Electric current distribution in case (a). (d) Electric current distribution in case (b). All the other

parameters are the same as used in Fig. 5.7.

To characterize the intensity of the secondary flow, we use the two-dimensional kinetic energy $\|\mathbf{u}_\perp\|^2$. **Fig. 5.16** depicts $\|\mathbf{u}_\perp\|^2$ as a function of the current flux j^*. The solid line with crosses and the dashed line with squares correspond, respectively, to an infinite height annulus with $k = 2.39$ and a finite annulus with $l = 2\pi/2.39 = 2.63$. The dashed lines with circles and triangles correspond, respectively, to finite annulus with height $l = 1.26$ and 0.63. When the annulus is infinite and the current is negative, $\|\mathbf{u}_\perp\|^2 = 0$ for all Dean numbers. When the annulus is infinite and $j^* > 0$ is smaller than its critical value, $\|\mathbf{u}_\perp\|^2 = 0$. Once j^* exceeds its critical value, secondary flows bifurcate supercritically and $\|\mathbf{u}_\perp\|^2$ increases as j^* increases.

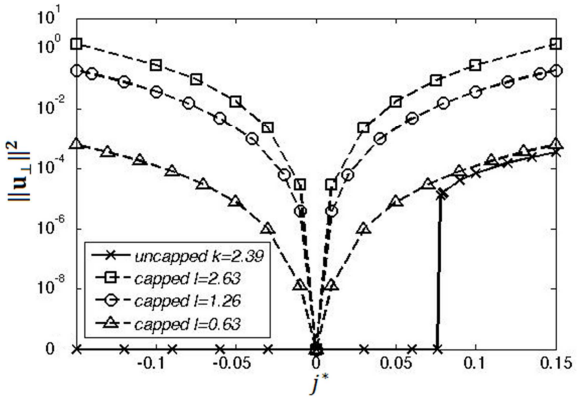

Figure 5.16 The intensity of the secondary flow $\|\mathbf{u}_\perp\|^2$ as a function of the current density j^*. The dashed line with squares, dashed line circles, and dashed line with triangles correspond, respectively, to capped conduits with height $l = 2\pi/2.39, 2\pi/5,$ and $2\pi/10$. The solid line with crosses correspond to an infinitely long annular conduit with periodic boundary conditions in the axial (z) direction and wave number $k = 2.39$. All the other parameters are the same as in Fig. 5.7.

When the annulus has finite height, secondary flows are always present. As the current density $|j^*|$ and the Dean number Dn increase so does $\|\mathbf{u}_\perp\|^2$. For similar Dn, $\|\mathbf{u}_\perp\|^2$ associated with the positive (outward) current is only slightly larger than $\|\mathbf{u}_\perp\|^2$ associated with the negative current. For example, when $l = 2\pi/2.39$, $j^* = 0.1$, $\mathrm{Dn} = 6.11$, $\|\mathbf{u}_\perp\|^2 = 0.2860$. The reverse current $j^* = -0.1$ leads to $\|\mathbf{u}_\perp\|^2 = 0.2856$. The equivalent, purely pressure-driven flow generates convection intensity $\|\mathbf{u}_\perp\|^2 = 0.2858$. In summary, $\|\mathbf{u}_\perp\|^2_{\text{Positive } j^*} > \|\mathbf{u}_\perp\|^2_{\text{Pressure Driven}} > \|\mathbf{u}_\perp\|^2_{\text{Negative } j^*}$ and $\|\mathbf{u}_\perp\|^2_{\text{Finite Annulus}} > \|\mathbf{u}_\perp\|^2_{\text{Infinite Annulus}}$. When the cross-sectional aspect ratio l decreases, the convection intensity decreases most likely due to the drag associated with the floor and ceiling. The figure suggests that when the annulus has a finite height, the floor and ceiling are the major causes for secondary flow and not the Dean instability.

Fig. 5.17a depicts the intensity of the secondary flow $\|\mathbf{u}_\perp\|^2$ as a function of the annulus aspect ratio l ($0.63 < l < 2.63$). The dashed line corresponds to positive current flux $j^* = 0.1$ and the circles correspond to negative current flux $j^* = -0.1$. The two curves are nearly overlapping. Consistent with Fig. 5.16, as *l* increases, the retarding effect of the floor and ceiling decreases, and $\|\mathbf{u}_\perp\|^2$ increases until it attains an asymptotic value independent of *l*. The flow field in the case of the finite length annulus is fundamentally different than in the case of the infinite height annulus no matter how large *l* is. Fig. 5.17b depicts the relative difference between $\|\mathbf{u}_\perp\|^2$ in the case of the outward current and the case of the inward current as a

function of l. The difference is most pronounced at small l values and it decreases to about 0.15% as l increases.

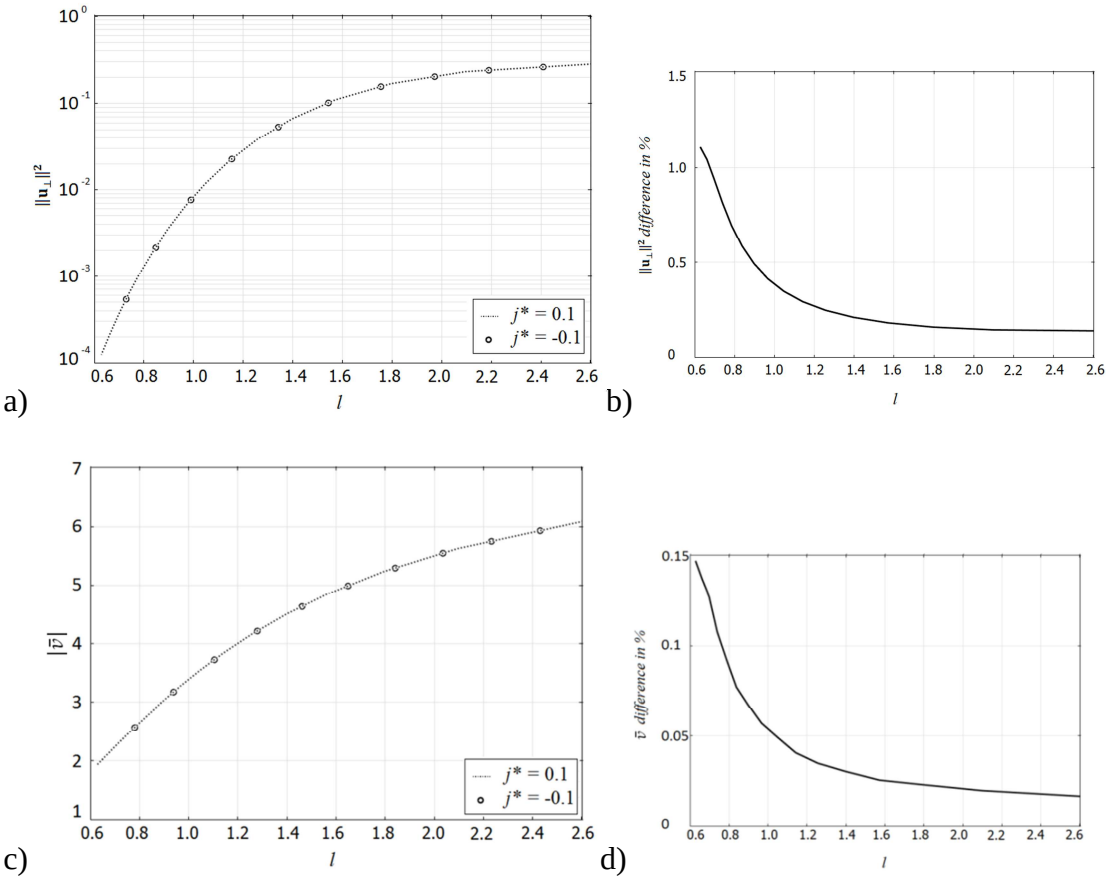

Figure 5.17 The intensity of the secondary flow $\|\mathbf{u}_\perp\|^2$ (a) and the average azimuthal velocity $|\bar{v}|$ are depicted as functions of the aspect ratio l when the current is controlled ($|j^*| = 0.1$). The dashed line and the hollow circles correspond, respectively, to positive and negative currents. The relative difference between the intensity of the secondary flow $\|\mathbf{u}_\perp\|^2$ **(**c) and the average azimuthal velocity (d) as functions of the aspect ratio l.

Similar behavior is observed when the electrodes' potential difference is controlled. **Fig. 5.18** depicts $\|\mathbf{u}_\perp\|^2$ as a function of the applied external potential

difference ΔV_{ext}. The solid line with crosses denote an infinite annulus with $k = 4$. The dashed lines with squares, circles, and triangles correspond to finite annuli with $l = \pi, \pi/2$ and $\pi/4$. For conditions similar to the ones specified in Fig. 5.11, $\Delta V_{ext} = 11.32$, and the resulting current flux $|j^*| \sim 0.1$. When the current is positive (negative), the intensity of the secondary flows $\|\mathbf{u}_\perp\|^2 = 0.2850$ (0.2832). The equivalent pressure-driven flow gives $\|\mathbf{u}_\perp\|^2 = 0.2843$. Here again, $\|\mathbf{u}_\perp\|^2_{\text{Positive } \Delta V_{ext}} > \|\mathbf{u}_\perp\|^2_{\text{Pressure Driven}} > \|\mathbf{u}_\perp\|^2_{\text{Negative } \Delta V_{ext}}$ and $\|\mathbf{u}_\perp\|^2_{\text{Finite Annulus}} > \|\mathbf{u}_\perp\|^2_{\text{Infinite Annulus}}$.

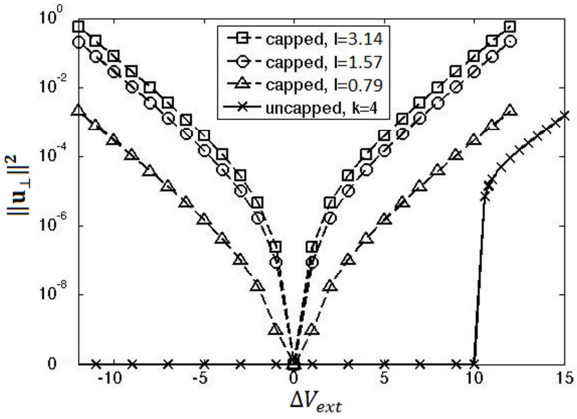

Figure 5.18 The intensity of the secondary flow $\|\mathbf{u}_\perp\|^2$ as a function of the potential difference between the electrodes (ΔV_{ext}). The dashed line with squares, dashed line circles, and dashed line with triangles correspond, respectively, to capped conduits with height $\pi, \pi/2$ and $\pi/4$. The solid line with crosses correspond to an infinitely long annular conduit with periodic boundary conditions in the axial (z) direction and wave number $k = 4$. All the other parameters are the same as in Fig. 5.11.

Fig. 5.19a, b, and c depict, respectively, the secondary flow's intensity $\|\mathbf{u}_\perp\|^2$,

the average azimuthal velocity $\bar{v}$, the average current density $\bar{j}$ as functions of the aspect ratio l ($0.63 < l < 3.14$). The dashed line and the hollow circles correspond, respectively to the case of $\Delta V_{ext} = 15$ and the case of $\Delta V_{ext} = -15$. Fig. 5.19d depicts the relative differences between the above quantities when the current is positive and when the current is negative as functions of the annulus aspect ratio l. When the electrodes' potential difference is controlled, the current flux distribution (which is responsible for the Lorentz body force) differs more greatly between the positive and negative potential cases than in the controlled current case. This leads to a greater difference in the controlled potential case between the intensities of the secondary flows when the current is positive and negative than in the controlled current case.

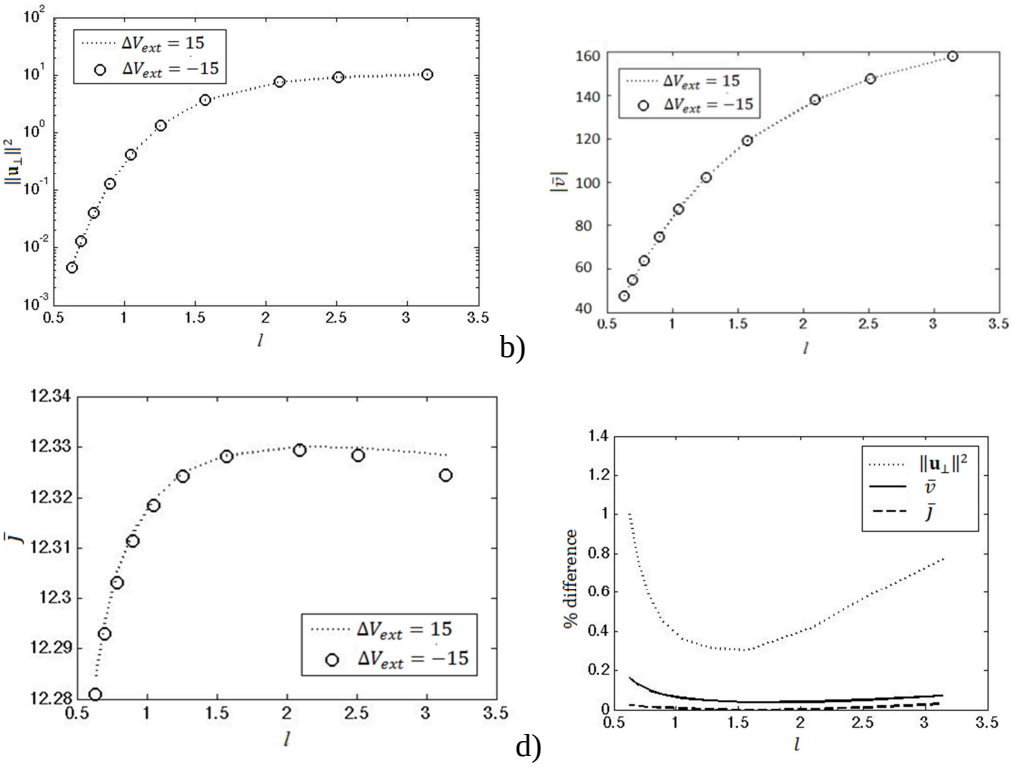

Figure 5.19 The intensity of the secondary flow $\|\mathbf{u}_\perp\|^2$ (a), the average azimuthal

velocity $|\bar{v}|$ (b), and the average current flux (c) as functions of the aspect ratio l when the potential is controlled ($|\Delta V_{ext}| = \pm 15$). The dashed line and the hollow circles correspond, respectively, to positive and negative currents. (d) The relative difference between the intensity of the secondary flow $\|\mathbf{u}_{\perp}\|^2$ (dashed line), average azimuthal velocity (solid line), and average current flux as functions of the aspect ratio l.

In contrast to the case of the infinitely tall annulus, in the case of the finite-height annulus the differences between the flow induced by the outwardly-directed current and the inwardly-directed current are not large. This is because the secondary flow is primarily driven by the pressure gradients induced by the floor and ceiling and only weakly modified by the Dean instability.

5.6 Conclusions

In this study, we provided base solutions of concentrations' distributions, velocity profile, and current flux field of MHD flow in an annular conduit when the cylinders are infinitely long. The azimuthal flow is similar to the celebrated Dean flow. In contrast to the Dean flow, the MHD flow described here can actually be attained in practice.

We examined, for the first time, the linear stability of the azimuthal flow in the infinitely long annulus. The computed disturbance growth rate at loss of stability was always real and the principle of exchange of stability holds. We delineated the effect

of electrochemistry on the Dean instability. We found that when the current flow is directed outwardly (positive), the MHD problem is significantly less stable than the Dean problem and secondary flows bifurcate from the base, azimuthal flow at a Dean number much smaller than in the pressure-driven case. In other words, in the case of outwardly-directed current, electrochemical effects have a destabilizing effect. When the current was directed inwardly (negative), the azimuthal flow was linearly stable for *all* Dean numbers. In other words, in the inward-directed case, electrochemical effects stabilize the flow.

The predictions of the linear stability analysis were compared and favorably agreed with finite element solutions of the nonlinear problem. Consistent with linear stability theory, the nonlinear simulations indicate that the disturbances grow/decay monotonically and that the bifurcation in the case of outwardly directed current is supercritical.

Finite element analysis was carried out to study the magnetohydrodyamic flow in the capped (finite length) annulus. When the annulus is of finite height, pure azimuthal flows are inadmissible and the flow is always three-dimensional, regardless of the direction of the current. The secondary flow is primarily caused by pressure gradients induced by the presence of the floor and ceiling (non-slip) and the Dean instability plays a relatively minor role in modifying the flow field. As a result, the differences in the intensity of the secondary convection between the outwardly -directed current and inwardly-directed current are relatively small, albeit the intensity of the secondary convection is always greater in the former case.

Chapter 6: Conclusions and Outlook

Microfluidics is an exciting, new area that is revolutionizing biotechnology in many different ways. Microfluidics allows researchers to manipulate macromolecules, transport biochemical species and particles, stir reagents, and carry out massive, parallel experiments in a very time-efficient and inexpensive way. Microfluidic devices are used in drug discovery and to facilitate medical diagnostics both in the lab and at the point of care.

This dissertation has focused on the pumping mechanisms of microfluidic devices. Pumps are essential components of many microfluidic devices as they are needed to induce and control fluid motion. In this thesis, I discussed two different pumping mechanisms. First, I induced fluid motion using surface tension imbalance. The variations in the surface tension forces were caused by the non-uniform geometry of the micro-conduit, which in turn, drives the fluid motion. Second, I studied magneto-hydrodynamic pumping, resulting from the interaction between externally applied electric and magnetic fields, or the Lorentz force. In the following content of this chapter, I summarize the main results of my accomplished work, and, when appropriate, provide suggestions for future work.

6.1 Phase Change Valves and Immiscible Displacement

In the first part of the thesis, I demonstrated the use of surface tension forces

to move slugs of liquid. When the ends of a slug of wetting liquid reside in segments of a conduit with different diameters, the slug will tend to move towards the cross-section with the smaller diameter. The slug motion can be used to either close or open valves. To prevent unwanted motion of the slug, the slug is normally kept frozen. When valve closing or opening is needed, the slug is heated and melted to achieve the desired actuation. A one dimensional dynamic model was constructed to describe the slug's dynamics. Experimental devices were constructed and tested and the theoretical predictions were compared and favorably agreed with experimental observations. We proposed an optimization scheme for the maximum flow rate based on the dynamic model and got good agreement between the optimization result and the brute force solutions of the dynamic model. The valving scheme operated successfully both when the slug displaced air and liquid. When attempting to use this scheme to pump a second liquid, we encountered interfacial instabilities at the interface between the more wetting fluid that migrates along the conduit's surface and the less wetting fluid that formed the core of the flow.

In most of my experiments, I used slugs made of paraffin and conduits with circular cross-sections. Many microfludic systems are, however, made with plastics and the conduits have a rectangular cross-section. When the molten paraffin slug displaces air or water in a rectangular conduit, as a result of surface tension forces, the paraffin will progress rapidly along the cross-section's corners. This process, over time would result in the disappearance of the piston-like form of the paraffin slug. One possible way to maintain the integrity of the piston is to embed magnetizable

particles in the paraffin. In the presence of an external magnetic field, the inter particle forces will maintain the paraffin together. A follow up work may analyze the behavior of a suspension of magnetic particles embedded in paraffin in the presence of an external magnetic field.

I also observed interfacial instabilities when molten paraffin (oil) was used to displace water in circular conduits. When the conduit was made of glass, a thin film of water was left along the surface of the tube when the water was displaced by the oil forming an annular shell around the oil. Eventually, the oil water interface lost stability and wave evolved along the interface. This phenomenon is undesirable in most cases. A possible remedy to suppress these types of instabilities may be through the use of magnetic particles and a magnetic field.

6.2 Electrochemical Cell Subjected to Time-Alternating Potential

Next, I explored the use of magnetohydrodynamics to pump liquids. The basic idea is to transmit current in an electrolyte solution in the presence of a magnetic field. The current interacts with the magnetic field to produce Lorentz body force, which in turns drives fluid motion. Since the fluid motion modifies the ions' concentrations in solution, the electric problem and the momentum equations are coupled. To better understand electric current transmission in electrolyte solutions, I investigated a one-dimensional electrolytic cell and examined the current-potential relationship under DC conditions. To this end, I solved the Nernst-Planck equations together with the electroneutrality condition. The current-voltage relations were obtained

analytically and compared to the numerical results. Then, I examined the AC response when the potential difference between the electrodes varies periodically in time. The theoretical study consisted of solving the full Poisson-Nernst-Planck equations. Since the solution of the full Poisson-Nernst-Planck equations is computationally intensive, approximate boundary conditions were derived so that one can solve time-periodic problems by solving the Nernst-Planck equations in the bulk (with electroneutrality condition) and without a need to resolve the electric double layer. The predictions of the approximate model were critically compared with the predictions of the full model. For the cases investigated, the difference between the exact and approximate model predictions was smaller than 6%. The use of the approximate model allows one to overcome the numerical difficulty associated with the two vastly different length scales: the macroscopic size of the electrolyte cell and the nanosclae thickness of the electric double layer associated with modeling electrochemical processes including problems associated with magnetohydrodynamic flow of electrolyte solutions.

6.3. MHD Flow and Equivalence with Pressure-Driven Flow

I constructed a mathematical model for MHD flows of electrolyte solutions in microfluidic systems. In general, the model requires the concurrent solution of the Nernst-Planck equations and the momentum equations. The flow field modifies the concentration field and the concentration field affects the electric current, which, in turn, affects the body force in the momentum equation. MHD has the advantage of providing a convenient means to pump and stir fluids and control fluid flow with

electrical signals and without a need for moving mechanical components. Flow can be directed along any desired path in a microfluidic network without a need for any valves and its direction can be reversed simply by reversing electrode polarity. The disadvantage of MHD is that it involves a volumetric force that does not scale favorably as the conduit size decreases. MHD pumps operating with electrolyte solutions also have very low conversion efficiency, as only a very small fraction of the electric power is converted into work. More serious shortcomings include the need to operate with electrolyte solutions that undergo reversible reactions to avoid bubble formation and undesirable electrochemical electrode reactions and the limitation on the maximum amount of current that can be transmitted in the solutions. It seems that MHD are most likely to benefit applications in which conduit sizes range from hundreds of micrometers to millimeters - a range of length scales in which the MHD drive provides significantly higher flow rates than electroosmosis.

I have shown that when the Reynolds number is low, the magnetic field is uniform, and the electric field is orthogonal to the magnetic field, the Lorentz body force is irrotational and one can define a “Lorentz” potential. In other words, the MHD flow is equivalent to pressure-driven flow, and one can use the large body of data available in the literature for pressure-driven flow to deduce the MHD flow patterns and drag coefficients. The above conditions often prevail in microfluidic systems. I utilized this equivalence in two examples. The first example consisted of a uniform conduit. Here, the equivalence between MHD flow and pressure-driven flow has been known for many years. The second example consisted of a conduit patterned

with pillars. This is a somewhat more general case as the electric flux is neither unidirectional nor uniform as in the first example. The equivalence between MHD flow and pressure-driven flow allows me to utilize drag coefficients available in the literature for pressure-driven flow to calculate the MHD flow patterns provided that the total electric current is controlled. The use of the MHD-pressure driven flow equivalence requires caution, however, since the emergence of secondary flows such as may evolve when the fluid goes around a bend (Yi and Bau 2003) or a curve will destroy the analogy between MHD and pressure-driven flows. Conduits patterned with pillars may be useful in application ranging from separation processes and catalytic reactors where large solid liquid interface is desired to heat exchangers, where the pillars act as fins.

I also computed the electric current, concentration, and flow field in a conduit and demonstrated that an optimal pillar diameter exists that maximizes the current flow. It is plausible that even higher current transmission can be obtained by optimizing the shape of the pillar. However, maximum flow rate still happens in the absence of pillars.

The conduits with pillar arrays can be used as columns for chromatographic separation with the pillars providing support for the stationary phase. In this case, it would be desirable to optimize the shape of the pillars, their pattern, and the flow field to minimize Taylor-Aris dispersion and to minimize the hydrodynamic drag.

6.4 MHD Flow in a Concentric Annulus

When secondary flows evolve such as when the fluid goes around a bend, the MHD-pressure driven flow equivalence no longer exists. It is of interest to determine the circumstances under which secondary MHD flows evolve. I considered MHD flow of a symmetric, binary electrolyte in a concentric annulus. In the case of infinitely long annulus, I obtained the velocity field, concentrations' distributions, and current flux field as functions of the potential difference between the cylindrical electrodes. The azimuthal flow is similar to the celebrated Dean flow. I then examined the linear stability of the azimuthal flow in the infinitely long annulus. The computed disturbance growth rate at loss of stability was always real and the principle of exchange of stability held. I found, for the first time, that electrochemical effects greatly modify the stability characteristics of the flow. When the electric current is directed outwardly (positive), the MHD Dean problem is significantly less stable than the pressure-driven, classical Dean problem and secondary flows bifurcate from the base, azimuthal flow at a Dean number much smaller than in the pressure-driven case. In other words, in the case of outwardly-directed current, electrochemical effects have a destabilizing effect. When the current was directed inwardly (negative), the azimuthal flow was linearly stable for *all* Dean numbers. In other words, when the electric current is directed inwardly (negative), electrochemical effects stabilize the flow. The predictions of the linear stability analysis were compared and favorably agreed with finite element solutions of the nonlinear problem. Consistent with linear stability theory, the nonlinear simulations indicate that the disturbances grow/decay monotonically and that the bifurcation in the case of outwardly directed current is

supercritical.

When the annulus has finite length, purely azimuthal flow is no longer possible. The non-slip floor and ceiling cause pressure gradients within the annular cross -section, which in turn induces secondary flow. Thus, when the annulus is of finite height, pure azimuthal flow is inadmissible and the flow is always three-dimensional regardless of the direction of the current. Finite element analysis was carried out to determine the flow field in the finite length annulus. I find that the secondary flow is primarily caused by pressure gradients induced by the presence of the floor and ceiling. When the length of the annulus is moderate, the Dean instability plays a relatively minor role in modifying the flow field. As a result, the differences in the intensity of the secondary convection between the outwardly-directed current and inwardly-directed current are relatively small, albeit the intensity of the secondary convection is always greater in the former case.

There are many possible extensions of this work. In my pioneering work, I focused on a binary, symmetric electrolyte. Similar analysis can be carried out for other solutions such as RedOx electrolytes that undergo reversible reactions at the electrode surfaces and in presence of excess supporting electrolyte. It is likely, that in the presence of abundant supporting electrolyte, the electric conductivity will be insensitive to the concentration distribution of the reacting species and the stability characteristics of the MHD flow will be more in line with that of the classical, pressure-driven Dean flow. And perhaps, most importantly, the predictions of my theory still require experimental verification.

BIBLIOGRAPHY

Aleksandrov R. S., Grigin A. P. and Davydov A. D., 2001, "Critical Time of the Convective Instability Emergence in Electrochemical Systems", *Russian Journal of Electrochemistry* **37**, 1237

Alemany A. and Chopart J. P., 2007, *An outline of magnetoelectrochemistry, Magnetohydrodynamics - Historical Evolution and Trends*, Springer, 391-407

Avramenko A. A., Kobzar S. G., Shevchuk I. V., Kuznetsov A. V. and B. I. Basok, 2003, "Laminar Forced Convection in Curved Channel with Vortex Structures", *Journal of Thermal Sciences* **13**, 143

Bara B., Nandakumar K., and Masliyah J. H., 1992, "An experimental and numerical study of the Dean problem: flow development towards two-dimensional multiple solutions", *Journal of Fluid Mechanics* **244**, 339

Bard A.J. and Faulkner L.R., 2001, *Electrochemical Methods, fundamentals and applications*, 2nd Edition, Wiley

Batchelor G. K., 1967, *An Introduction to Fluid Dynamics*, Cambridge University Press

Bau H. H., Zhong J. and Yi M., 2001, "A minute magneto hydro dynamic (MHD) mixer", *Sensors and Actuators B* **79**, 207-215

Bau H. H., Zhu J., Qian S. and Xiang Y., 2003, “Magnetohydrodynamically controlled fluidic network”, *Sensors and Actuators B* **88**, 205-216

Baylis J. A., 1964, “Detection of the Onset of Instability in a Cylindrical Magnetohydrodynamic Flow”, Nature **204**, 563

Baylis J. A., 1971, “Experiments on laminar flow in curved channels of square section” , *Journal of Fluid Mechanics* **48**, 417

Baylis J. A. and Hunt J. C. R., 1971, “MHD flow in an annular channel; theory and experiment”, *Journal of Fluid Mechanics* **48**, 423

Bayraktar T. and Pidugu S. B., 2006, “Characterization of liquid flows in microfluidic systems”, *International Journal of Heat and Mass Transfer* **49**, 815-824

Bazant M. Z., Chu K. T. and Bayly B. J., 2005, “Current-Voltage Relations for Electrochemical Thin Films”, *Siam journal on applied mathematics* **65:5**, 1463-1484

Bazant M. Z., Thornton K. and Ajdari A., 2004, “Diffuse-charge dynamics in electrochemical systems”, *Physical Review E* **70**, 021506

Ben Richou A., Ambari A. and Naciri J. K., 2004, “Drag force on a circular cylinder midway between two parallel plates at very low Reynolds numbers-Part 1: Poiseuille flow (numerical)”, *Chemical Engineering Science* **59**, 3215-3222

Berger S. A. and Talbot L., 1983, “Flow in Curved Pipes”, *Annual Review of Fluid Mechanics* **15**, 461

Bico J. and Quere D., “Self-propelling slugs”, 2002, *Journal of Fluid Mechanics* **467**, 101-112

Boden R., Lehto M., Simu U., Thornell G., Hjort K., Schweitz J. A., 2006, “A

polymeric paraffin actuated high-pressure micropump", *Sensors and Actuators A* **127**, 88-93

Bograchev D. A., Davydov A. D., Volgin V. M., 2008, "Linear stability of Rayleigh-Benard-Poiseuille convection for electrochemical system", *International Journal of Heat and Mass Transfer* **51**, 4886

Bonnefont A., Argoul F. and Bazant M. Z., 2001, "Analysis of diffuse –layer effects on time-dependent interfacial kinetics", *Journal of Electroanalytical Chemistry* **500**, 52-61

Bosanquet C. H., 1923, "On the flow of liquids into capillary tubes", *Philosophical Magazine* **45**, 525

Boum N. G. B. and Alemany A., 1999, "Numerical simulations of electrochemical mass transfer in electromagnetically forced channel flow", *Electrochemica Acta*, **44**, 1749-1760

Boutabaa M., Helin L., Mompean G. and Thais L., 2009, "Numerical study of Dean vortices in developing Newtonian and viscoelastic flows through a curved duct of square cross-section", *Comptes Rendus Mecanique* **337**, 40

Bovendeerd P. H. M., Van Steenhoven A. A., Van de Vosse F. N. and Vossers G., 1987, "Steady entry flow in a curved pipe", *Journal of Fluid Mechanics* **177**, 233

Brassard D., Malic L., Normandin F., Tabrizian M. and Veres T., 2008, "Water-oil core-shell droplets for electrowetting-based digital microfluidic devices", *Lab on a Chip* **8**, 1342-1349

Bretherton F. P., 1961, "The motion of long bubbles in tubes", *Journal of Fluid*

Mechanics **10**, 166-168

Burkhalter J. E. and Koschmieder E. L., 1973, “Steady supercritical Taylor vortex flow”, *Journal of Fluid Mechanics* **58**, 547

Carlen E. T., Mastrangelo C. H., 2002, “Electrothermally Activated Paraffin Microactuators”, *Journal of Microelectromechanical System* **11**, 275-282

Chandrasekhar S., 1961, *Hydrodynamic and Hydromagnetic Stability*, Oxford at the Clarendon Press

Chen Z., Wang J., Qian S. and Bau H. H., 2005, “Thermally-actuated, phase change flow control for microfluidic systems”, *Lab on a Chip* **5**, 1277-1285

Cheng K. C. and Akiyama M., 1970, “Laminar Forced Convection Heat Transfer in Curved Rectangular Channels”, *International Journal of Heat and Mass Transfer* **13**, 471

Cheng K. C., Lin R. C. and Ou J. W., 1976, “Fully Developed Laminar Flow in Curved Rectangular Channels”, *Journal of Fluid Engineering* **98**, 41

Chu K. T., Bazant M. Z., 2006, “Nonlinear electrochemical relaxation around conductors”, *Physical Review E* **74(1)**, 011501

Cole J. A., 1976, “Taylor- vortex instability and annulus- length effects”, *Journal of Fluid Mechanics* **75**, 5

Cuming H. G., 1955, “The Secondary Flow in Curved Pipes”, *Aeronautical Research Council Reports and Memoranda*, 2880

De Gennes P. G., 1998, “The dynamics of reactive wetting on solid surfaces”, *Physica A* **249**, 196-205

De Vriend H. J., 1931, “Velocity redistribution in curved rectangular channels”, *Journal of Fluid Mechanics* **107**, 423

Dean W. R., 1928, “Fluid Motion in a Curved Channel”, *Proceeding of the Royal Society of London A* **121**, 402

Deka R. K. and Takhar H. S., 2004, “Hydrodynamics stability of viscous flow between curved porous channel with radial flow”, *International Journal of Engineering and Science* **42**, 953

Digilov R. M., 2007, “Making a fluid rotate: Circular flow of a weakly conducting fluid induced by a Lorentz body force”, *American Journal of Physics* **75**, 361

Drazin P. G. and Reid W. H., 2010, *Hydrodynamic Stability*, Cambridge University Press, 2nd edition

Eijkel J. C. T., Dalton C., Hayden C. J., Burt J. P. H. and Manz A., 2003, “A circular ac magnetohydrodynamic micropump for chromatographic applications”, *Sensors and Actuator B* **92**, 215

Eijkel J. C. T., Van den Berg A. and Manz A., 2004, “Cyclic electrophoretic and chromatographic separation methods”, *Electrophoresis* **25**, 243 – 252

Eustice J., 1910, “Flow of water in curved pipes”, *Proceeding of Royal Society of London A* **84**, 107

Eustice J., 1911, “Experiments on stream-line motion in curved pipes”, *Proceeding of Royal Society of London A* **85**, 119 (1911)

Faxen H., 1946, “Forces exerted on a rigid cylinder in a viscous fluid between

two parallel fixed planes", *Proceeding of Royal Swedish Academy of Engineering and Sciences* **187**, 1

Finlay W. H. and Nandakumar K., 1990, "Onset of two-dimensional cellular flow in finite curved channels of large aspect ratio", *Physics of Fluids A* **2**, 1163

Frumkin A., 1955, "Adsorptionserscheinungen und elektrochemische Kinetic", *Z Electroche* **59**, 807

Goldstein S., 1938, *Modern Developments in Fluid Dynamics*, Clarendon Press, Oxford

Grigin A. P., 1993, "Theory of the direct-current flow in Redox systems with one-electron transfer reactions", *Russian Journal of Electrochemistry* **29(9)**, 1089-1094

Gyves T. W., Irvine T. F. Jr., Naraghi M. H. N., 1999, "Gravitational and centrifugal buoyancy effects in curved square channels with conjugated boundary conditions", *International Journal of Heat and Mass Transfer* **42**, 2015

Gyves T. W. and Irvine T. F. Jr., 2000, "Laminar conjugated forced convection heat transfer in curved rectangular channels", *International Journal of Heat and Mass Transfer* **43**, 3953

Harrison W. J., 1924, *Transactions of the Cambridge Philosophical Society* **23**: 71

Heiser W. H. and Shercliff J. A., 1965, "A simple demonstration of the Hartmann layer", *Journal of Fluid Mechanics* **22**, 701

Ho J. E., 2007, "Characteristic study of MHD pump with channel in rectangular

ducts", *Journal of Marine Science and Technology* **15(4)**, 315-321

Hobbs E. D. and Pisano A. P., 2003, "Micro Capillary-force driven fluidic accumulator/ Pressure Source", *12th International Conference on Solid State Sensors Actuators and Microsystems* **11**, 155-158

Hollerbach R. and Fournier A., 2004, "End-effects in rapidly rotating cylindrical Taylor-Couette flow in MHD Couette Flows: Experiments and Models", AIP Conference Proceeding **733**, 114

Hoffman R. L., 1975, "A study of the advancing interface I. Interface shape in liquid-gas systems", *Journal of Colloid and Interface Science* **50**, 228-241

Humphrey J. A. C., Taylor A. M. K. and Whitelaw J. H., 1977, "Laminar flow in a square duct of strong curvature", *Journal of Fluid Mechanics* **83**, 509

Hunt J. C. R. and Williams W. E. , 1968, "Some electrically driven flows in magneto -hydrodynamics, Part 1. Theory", *Journal of Fluid Mechanics* **31**, 705

Hunt J. C. R. and Malcolm D. G., 1968, "Some electrically driven flows in magnetohydrodynamics, Part 2. Theory and Experiment", *Journal of Fluid Mechanics* **33**, 775

Hunt J. C. R. and Stewartson K., 1969, "Some electrically driven flows in magneto -hydrodynamics, Part 3. The asymptotic theory for flow between circular electrodes", *Journal of Fluid Mechanics* **38**, 225

Ichimura K., Oh S. K. and Nakagawa M., 2000, "Light driven motion of liquids on a photosensitive surface", *Science* **288**, 1624-1626

Ito H., 1951, "Theory on laminar flow through curved pipes of elliptic and

rectangular cross-section", *Report of Institute of High Speed Mechanics Tohoku University* **1(1)**

Johnson M. and Kamm R. D., 1986, "Numerical studies of steady flow dispersion at low Dean number in a gently curving tube", *Journal of Fluid Mechanics* **172**, 329

Kabbani H., Wang A., Luo X. and Qian S., 2007, "Modeling RedOx-based magnetohydrodynamics in three-dimensional microfluidic channels", *Physics of Fluids* **19**, 083604

Kachoyan B. J., 1987, "Neutral curve behaviour in Taylor-Dean flow", *Zeitschrift Fur Angewandte Mathematik und Physic* **38**, 905

Khalzov I. V., 2008, "Equilibrium and stability of Magnetohydrodynamic flows in annular channels", Thesis

Kharkats Y. I., Sokirko A. V. and Bark F. H., 1995, "Properties of polarization curves for electrochemical cells described by Butler-Volmer kinetics and arbitrary values of the transfer coefficient", Electrochemica Acta **40**(2), 247-252

Khalzov I. V., IIgisonis V. I., Smolyakov A. I., Velikhov E. P., 2006, "Magnetorotational instability in electrically driven flow of liquid metal: Spectral analysis of global modes", *Physics of Fluids* **18**, 124107

Klintberg L., Karlsson M., Stenmark L., Thornell G., 2003, "A thermally activated paraffin-based actuator for gas-flow control in a satellite electrical propulsion system", *Sensors and Actuators A* **105**, 237-246

Klintberg L., Svedberg M., Nikolajeff F. and Thornell G., 2003, "Fabrication of a paraffin actuator using hot embossing of polycarbonate", *Sensors and Actuators A*

103, 307-316

Kobayashi R., 1977, “Stability of MHD Viscous Flow in a Curved Channel”, *Bulletin of the JSME* **20**, 983

Laser D. J. and Santiago J. G., “A review of micropumps”, 2004, *Journal of Micromechanics and Microengineering* **14**, R35-R64

Laughlin D. R., 2007, “Magnetohydrodynamic (MHD) actuator sensor”, US Patent 7171853

Lee J. S. and Lucyszyn S., 2005, “A Micromachined Refreshable Braille Cell”, *Journal of Microelectromechanical System* **14**, 673-682

Lioubashevski O., Katz E. and Willner I., 2004, “Magnetic force effects on electrochemical processes: A theoretical hydrodynamic model”, *Journal of Physical Chemistry B* **108**, 5778-5784

Liu R. H., Bonanno J., Yang J., Lenigk R., Grodzinski P., 2004, “Single-use, thermally actuated paraffin valves for microfluidic applications”, *Sensors and Actuators B* **98**, 328-336

A. J. P. Martin, 1958, *Gas Chromatography*, Academic Press, New York

Marshall G. and Mocskos P., 1997, “Growth model for ramified electrochemical deposition in the presence of diffusion, migration, and electroconvection”, *Physical Review E* **55**, 549-563

Martin J., Oshkai P. and Djilali N., 2005, “Flow Structures in a U-Shaped Fuel Cell Flow Channel: Quantitative Visualization Using Particle Image Velocimetry”, *Transaction of ASME* **2**, 70

Mazouchi A., Homsy G. M., 1999, “Thermocapillary migration of long bubbles in cylindrical capillary tubes”, *Physics of Fluids* **12**, 542-549

Mondal R. N., Uddin M. S. and A. Islam, 2008, “Non-isothermal Flow through a Curved Rectangular Duct for Large Grashof Number”, *Journal of Physical Science* **12**, 109

Moon P. and Spencer D. E., 1988, “§1 in Field Theory Handbook, Including Coordinate Systems, Differential Equations, and Their Solutions”, *Eleven Coordinate Systems*, 2nd ed. New York: Springer-Verlag, 1-48

Nakabayashi S., Inokuma K. and Karantonic A., 1999, “Magnetic effect for electrochemically driven cellular convection”, *Physical Review E* **59**, 6599

Newman J. and Thomas-Alyea K. E., 2004, *Electrochemical Systems*, 3rd edition, Wiley-Interscience

Oduoza C. F., 2004, “Electrochemical mass transfer at a heated electrode in a vertical annular flow cell”, *Chemical Engineering Processing* **43**, 921

Oh K. W. and Ahn C. H., 2006, “A review of microvalves”, *Journal of Micromechanics and Microengineering* **16**, R13-R39

Oh K. W., Namkoong K. and Park C., 2005, “A Phase Change Microvalve Using A Meltable Magnetic Material: Ferro-wax”, *Proceeding of microTAS*, 554-556

Park J. M., Cho Y. K., Lee B. S., Lee J. G. and Ko C., 2007, “Multifunctional microvalves control by optical illumination on nanoheaters and its application in centrifugal microfluidic devices”, *Lab on a Chip* **7**, 557-564

Probstein R. F., 1994, *Physicochemical Hydrodynamics: An Introduction*, John

Wiley & Sons Inc., New York

Qian S. and Bau H. H., 2005, “Magnetohydrodynamic flow of RedOx electrolyte”, *Physics of Fluids* **17**, 067105

Qian S., Chen Z., Wang J. and Bau H. H., 2006, “Electrochemical reaction with RedOx electrolyte in toroidal conduits in the presence of natural convection”, *International Journal of Heat and Mass Transfer* **49**, 21

Qian S., Bau H. H., 2009, “Magneto-hydrodynamics based microfluidics”, *Mechanics Research Communications* **36**, 10-21

Qin M. and Bau H. H., 2010, “When MHD-based microfluidics is equivalent to pressure-driven flow”, *Microfluidics and Nanofluidics*, DOI 10.1007/s10404-010 -0668-2

Ramos A., 2007, “Chapter 2: Electrohydrodynamic and Magnetohydrodynamic Micropumps”, *Microfluidic Technologies for Miniaturized Analysis Systems*, Springer

Ribando R. J. and Shadday M. A. Jr., 1984, “The Ekman Matching Condition in a Partially Filled, Rapidly Rotating Cylinder”, Journal of Computational Physics **53**, 266

Sangani A. S. and Acrivos A., 1982, “Slow flow past periodic arrays of cylinders with application to heat transfer”, *International Journal of Multiphase Flow* **8(1)**, 193-206

Selvaganapathy P., Carlen E. T., Mastrangelo C. H., 2003, “Electrothermally actuated inline microfluidic valve”, *Sensors and Actuators A* **104**, 275-282

Sharp K. V., Adrian R. J., Santiago J. G. and Molho J. I., 2005, “Chapter 6:

Liquid Flows in Microchannels", *The MEMS Handbook*, CRC Press LLC, 2nd edition

Silva R. J., Valle R. M. and Ziviani M., 1999, "Numerical hydrodynamic and thermal analysis of laminar flow in curved elliptic and rectangular ducts", *International Journal of Thermal Sciences* **38**, 585

Soh W. Y., 1988, "Developing fluid flow in a curved duct of square cross-section and its fully developed dual solutions", *Journal of Fluid Mechanics* **188**, 337

Song W. H., Kwan J., Kaigala G. V., Hoang V. N. and Backhouse C. J., 2008, "Readily integrated, electrically controlled microvalves", *Journal of Micromechanics and Microengineering* **18**, 045009

Sparrow E. M., Munro W. D. and Jonsson V. K., 1964, "Instability of the flow between rotating cylinders: the wide-gap problem", *Journal of Fluid Mechanics* **20**, 35

Staiger C. J., Baluska F., Volkmann D. and Barlow P., 2000, "Actin: A Dynamic Framework for Multiple Plant Cell", *Developments in Plant and Soil Sciences*, Springer

Sumino Y., Magome N., Hamada T. and Yoshikawa K., 2005, "Self-running Droplet: Emergence of Regular Motion from Nonequilibrium Noise", *Physical Review Letter* **94**, 068301

Szklarski J. and G. Rudiger, 2007, "Ekman-Hartmann layer in a magneto -hydrodynamic-Taylor-Couette flow", *Physical Review E* **76**, 066308

Targett M. J., Retallick W. B. and Churchill S. W., 1995, "Flow through Curved Rectangular Channels of Large Aspect Ratio", *AIChE Journal* **41**, 1061

Taylor G. I., 1923, "Stability of a viscous liquid contained between two rotating cylinders," *Philosophical Transaction of Royal Society of London A* **223**, 289

Velikhov E. P., 1959, “Stability of an ideally conducting liquid flowing between cylinders rotating in a magnetic field,” *Soviet Physics Journal of Experimental and Theoretical Physics* **36**, 995

Verkaik A. C., Beulen B. W. A. M. M., Bogaerds A. C. B., Rutten M. C. M. and van de Vosse F. N., 2009, “Estimation of volume flow in curved tubes based on analytical and computational analysis of axial velocity profiles”, *Physics of Fluids* **21**, 023602

Volgin V. M., Bograchev D. A. and Davydov A. D., 2007, “Onset of natural convection of electrolyte on horizontal electrode under non-steady-state-transfer conditions”, *International Journal of Heat and Mass Transfer* **50**, 2124

Walowit J., Tsao S. and Di Prima R. C., 1964, "Stability of flow between arbitrarily spaced concentric cylinder surfaces, including the effect of a radial temperature gradient," *Journal of Applied Mechanics* **31**, 585

Washburn E. W., “The dynamics of capillary flow”, 1921, *Physical Review* **XVII-3**, 273-283

Weislogel M. M., 1997, “Steady spontaneous capillary flow in partially coated tubes”, *AIChE Journal* **43**, 645-655

White F. M., 2006, *Viscous Fluid Flow*, 3rd ed. McGraw-Hill, New York

Winters K. H., 1987, “A bifurcation study of laminar flow in a curved tube of rectangular cross-section”, *Journal of Fluid Mechanics* **180**, 343

Woias P., “Micropumps-past, progress and future prospects”, 2005, *Sensors and Actuators B* **105**, 28-38

Wouahbi F., Allaf K. and Sobolik V., 2007, “Electrochemical analysis of Taylor vortices”, *Journal of Applied Electrochemistry* **37**, 57

Yamamoto K., Wu X., Hyakutake T. and Yanase S., 2004, “Taylor–Dean flow through a curved duct of square cross section”, *Fluid Dynamic Research* **35**, 69

Yamamoto K., Wu X., Nozaki K. and Hayamizu Y., 2006 “Visualization of Taylor-Dean flow in a curved duct of square cross-section”, *Fluid Dynamic Research* **38**, 1

Yan X., Wang Q. and Bau H. H., 2010, “Dispersion in retentive pillar array columns”, *Journal of Chromatography A* **1217(8)**, 1332-1342

Yanase S., Yamamoto K. and Yoshida T., 1994, “Effect of curvature on dual solutions of flow through a curved circular tube”, *Fluid Dynamic Research* **13**, 217

Yanase S., Kaga Y. and Daikai R., 2002, “Laminar flows through a curved rectangular duct over a wide range of the aspect ratio”, *Fluid Dynamics Research* **31**, 151

Yang B. and Lin Q., 2006, “Compliance-Based Latchable Microfluidic Actuators Using a Paraffin Wax”, *19th IEEE International Conference of MEMS*, 738-741

Yoo J. C., Choi Y. J., Kang C. J. and Kim Y. S., 2007, “A novel polydimethylsiloxane microfluidic system including thermopneumatic-actuated micropump and Paraffin-actuated microvalve”, *Sensors and Actuators A* **139**, 216-220

Yun K. S., Cho I. J., Bu J. U., Kim C. J. and Yoon E., 2002, “A Surface-Tension

Driven Micropump for Low-Voltage and Low-Power Operations", *Journal of Microelectromechanical System* **11**, 454-461

Zhang C., Xing D. and Li Y., 2007, "Micropumps, microvalves, and micromixers within PCR microfluidic chips: Advances and trends", *Biotechnology Advances* **25**, 483-514

Zhong, J., Yi, M., and Bau, H., H., 2002, "A Magneto-Hydrodynamics (MHD) Pump Fabricated with Ceramic Tapes", *Sensors and Actuators A Physical* **96**, 1, 59-66

Ziober B. L., Mauk M. G., Falls E. M., Chen Z., Ziober A. F. and Bau H. H., 2008, "Lab-on-a-chip for oral cancer screening and diagnosis", *Head and Neck* **30(1)**, 111 – 121